Quantitative single-molecule mapping of neuronal proteins at the nanoscale

Silvia Scalisi

XXXII ciclo
Scuola di Dottorato in Fisica
Università degli Studi di Genova

Tutor: *Prof. Alberto Diaspro*
Supervisor: *Dr. Francesca Cella Zanacchi*

“I learned then what science was about: it was patience.”

Richard Feynman, What is Science?

A Stefano, il mio compagno, e a Carmen, mia madre,
perché siete sempre con me, uno al mio fianco e l’altra nel mio cuore.

Table of Contents

Abstract **1**

Chapter 1 - An overview of super-resolution fluorescence microscopy **3**

1.1 Introduction to fluorescence optical microscopy 4

1.1.1 Fluorescence 4

1.1.2 Fluorescence optical microscopy 7

1.2 Optical microscope resolution and diffraction limit 10

1.3 Super-resolution microscopy 13

1.3.1 Breaking the diffraction barrier 14

1.3.2 Targeted read-out methods 14

1.3.3 Stochastic switching of fluorophores 16

1.3.4 Other super-resolution techniques 17

1.4 Stochastic optical reconstruction microscopy (STORM) 17

1.4.1 Features of STORM probes 19

1.4.2 Spatial resolution of STORM 22

1.4.3 STORM modalities 25

1.4.4 Experimental requirements for STORM imaging 29

1.5 Quantitative methods in SMLMs 32

1.5.1 Cluster analysis of localization data sets 33

1.5.2 Calibration tools for quantifying protein copy number 34

Chapter 2 - Discovering neurons with single-molecule localization microscopy **37**

2.1 Fundamentals of neuroscience 38

2.1.1 Synapses 39

2.1.2 Synaptic proteins 40

2.1.3 Excitatory and inhibitory synapses 41

2.1.4 Synaptic plasticity 42

2.2 Single-molecule localization microscopy as a quantitative imaging tool for studying neurons 43

2.2.1 Structural investigation of neurons and synapses 43

2.2.2 Quantitative imaging of synaptic proteins 44

Chapter 3 - Quantitative investigation of GABA$_A$ receptor organization at the inhibitory synapse 47

3.1 The inhibitory neurotransmission 48

3.1.1 The GABAergic synapse 48

3.1.2 Synaptic plasticity and long-term potentiation of inhibition............................... 49

3.1.3 Gephyrin stabilizes GABA$_A$Rs at the postsynapse 50

3.2 Unveiling the nanoscale architecture of the inhibitory potsynaptic density 51

3.2.1 The role of gephyrin subsynaptic domains in the inhibitory plasticity............... 51

3.2.2 Nanoscale rearrangement of GABA$_A$Rs in GABAergic plasticity 53

3.3 Materials and methods 54

3.3.1 Primary neuronal cultures 54

3.3.2 iLTP induction and drug treatments.. 54

3.3.3 Immunostaining protocol 54

3.3.4 Activator-reporter dye pairs preparation protocol.. 55

3.3.5 STORM imaging and data reconstruction 56

3.3.6 Cluster analysis 57

3.3.7 Statistical analysis 58

3.4 Results... 58

3.4.1 Quantitative super-resolution imaging of GABA$_A$Rs 58

3.4.2 Enhancement of synaptic GABA$_A$Rs under plasticity conditions 61

3.4.3 Rearrangement of GABA$_A$Rs in a larger number of SSDs during iLTP 62

3.4.4 Nanoscale organization of GABA$_A$Rs inside SSDs... 63

3.4.5 SSD characteristics as a function of the number of SSDs per synapse............... 66

3.5 Discussion.. 68

Chapter 4 - Adhesion and migration of neurons on single-layer graphene 73

4.1 Nanomaterials and biological samples interaction 74

4.1.1 Graphene: the “wonder material”.. 74

4.1.2 Adhesion and proliferation of neurons on graphene 76

4.2 Quantification of adhesion proteins in epithelial cells and neurons on SLG............ 77

4.3 Materials and methods 78

4.3.1 Single-layer graphene/glass substrate fabrication 78
4.3.2 Cell cultures 78
4.3.3 Immunostaining protocol 78
4.3.4 Activator-reporter dye pair preparation protocol 79
4.3.5 STORM imaging and data reconstruction 79
4.3.6 Cluster analysis 79
4.3.7 Statistical analysis 79
4.4 Results 80
4.4.1 Quantification of vinculin in CHO cells 80
4.4.2 Quantification of vinculin in neurons 82
4.5 Discussion 83

Chapter 5 - Conclusions and future perspectives 85

List of references 87

List of publications 97

Acknowledgments 99

Ringraziamenti 101

Abstract

The advent of super-resolution microscopy, also called nanoscopy, allowed a substantial improvement of spatial resolution, opening the door for the observation of biological structures beyond the diffraction limit impossible with conventional light microscopy. Among the super-resolution techniques, single-molecule localization microscopies have proven to be a powerful tool to address many biological issues, since they provide an imaging resolution of the order of tens of nanometers and the possibility to perform quantitative measurements.

Neuroscience has been one of the fields in biology to benefit most from super-resolution microscopy. During the last years, single-molecule localization microscopies have been widely exploited to study diffraction-limited subcellular structures in neurons, allowing a deeper understanding of molecular mechanisms underlying neural network functioning and its impairments in pathologies.

In this thesis, we developed a tool to investigate the distribution, spatial organization, clustering, and density of neural proteins at the nanoscale. In particular, we focused on the quantitative study of synaptic neurotransmitter receptors and focal adhesions.

The knowledge of the distribution and stoichiometry of synaptic proteins is fundamental to understand the regulation of the synaptic transmission in neurons. However, a detailed characterization of the protein architecture within synapses can be achieved only by visualizing them at a nanometric level. Here we propose a quantitative approach based on stochastic optical reconstruction microscopy combined with cluster analysis to investigate the molecular rearrangement of $GABA_A$ receptors into subsynaptic domains during synaptic plasticity of the inhibitory neurotransmission.

This approach was also applied to the study of the adhesion machinery of mammalian cells and neurons at the interface with single-layer graphene to investigate the interaction between cells and nanostructured materials. Due to their excellent properties and biocompatibility, graphene and its derivatives are the ideal candidates for many biomedical applications, such as neural tissue engineering. However, the adhesion processes at the graphene/neuron interface are still not clear nowadays. Our method offers an easy way to study how graphene substrates can affect adhesion and migration of different types of cells.

Chapter 1

An overview of super-resolution fluorescence microscopy

> *“Scientific inquiry starts with observation.*
> *The more one can see the more one can investigate.”*
>
> Martin Lee Chalfie
> (Nobel Prize for Chemistry in 2008)

During the last decades, fluorescence microscopy has become one of the most widespread, powerful, and versatile techniques to study biological samples. Despite the limits to the resolving power, due to the wave nature of light, the employment of fluorescent labels allowed the investigation of many structures and related processes inside cells and tissues with high molecular specificity and multicolor imaging ability. The recent development of super-resolution microscopy, also called nanoscopy, provided a new prospect into cell imaging, enabling optical microscopes to circumvent the resolution limit and to observe biological processes at the subcellular level.

Before the invention of the optical microscope, around 1600, the direct observation of most of the cells was not feasible. A cell is the smallest unit of life and the functional and morphological unit of all the living organisms. Being cells invisible to the naked eye, only the appearance of the first optical microscopes made it possible to observe and investigate their structure and functions.

The basic optical microscope uses visible light and a single lens, as in the earliest microscopes, or a system of lenses, as in the compound microscope, to magnify images of objects.

1.1 Introduction to fluorescence optical microscopy

Since the 17th century, plenty of improvements have been made on optical microscopy to get better imaging capabilities. The most crucial breakthroughs in light microscopy was the introduction of fluorescence microscopy.

1.1.1 Fluorescence

Fluorescence is a type of *luminescence*, which consists in the emission of light by a molecule when it relaxes from an electronically excited state. There are different kinds of luminescence, classified according to the modality of excitation. When a molecule is excited by absorption of light, fluorescence or phosphorescence can occur depending on the nature of the excited state.

The *Jablonski diagram* (Jablonski, 1933) (**figure 1.1**) describes the electronic state of a molecule and shows the possible transitions that can arise when the molecule absorbs a photon. An electron moves from the singlet ground state (S_0) to an excited singlet state (S_1), where its spin remains paired to the spin of the other electron in the ground state. Paired spins imply that the relaxing transition from S_1 to S_0 is spin allowed and occurs rapidly, in the order of 10^{-8} s. This relaxation pathway is called *fluorescence*, and emission of light accompanies it. Moreover, the excitation process also sets in motion molecular vibrations. Therefore, non-radiative transitions may take place within the same electronic state, like vibrational relaxations. *Internal conversion*, instead, involves vibrionic relaxation and brings the electron to the first excited singlet state, before the molecule fluoresces.

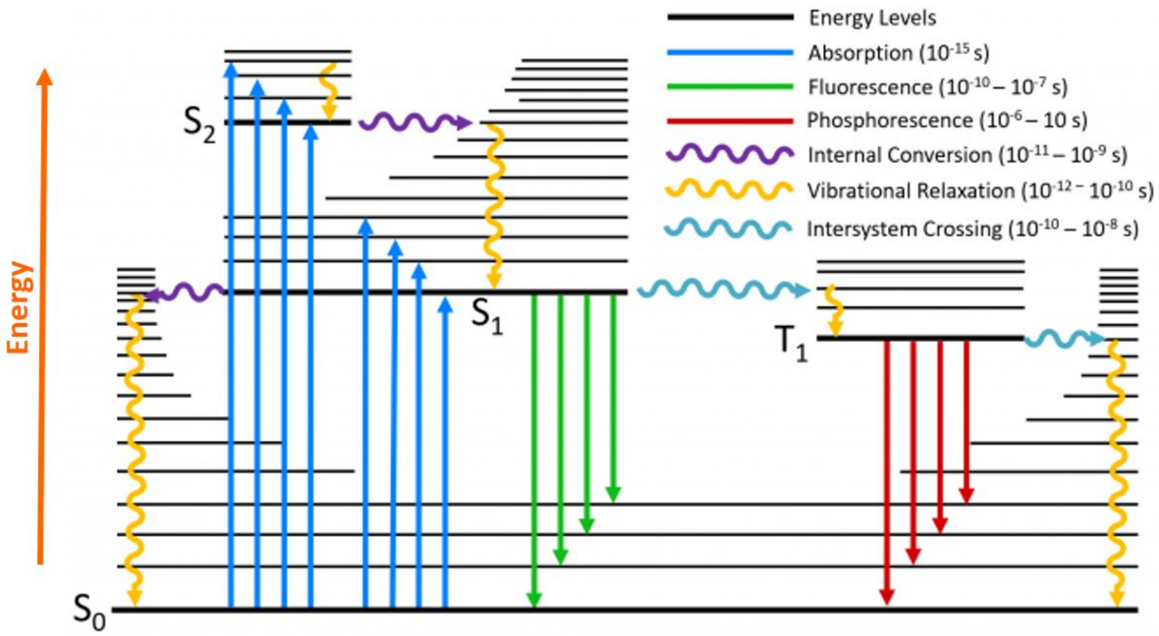
Energy Levels
Absorption (10^{-15} s)
Fluorescence ($10^{-10} – 10^{-7}$ s)
Phosphorescence ($10^{-6} – 10$ s)
Internal Conversion ($10^{-11} – 10^{-9}$ s)
Vibrational Relaxation ($10^{-12} - 10^{-10}$ s)
Intersystem Crossing ($10^{-10} – 10^{-8}$ s)
Energy
S_2
S_1
T_1
S_0

Figure 1.1 Jablonski diagram.

The Jablonski diagram illustrates the electronic states of a molecule and the possible transitions that can occur between them. In a typical Jablonski diagram, the *singlet ground state* is named S_0, the *singlet excited states* are indicated as S_1 andS_2 and the *triplet excited state* with T_1. All these electronic states are arranged vertically by energy and horizontally by spin multiplicity. Each electronic state has the lowest energy vibrational level represented with a thick line and the higher energy vibrational states represented with thinner lines. *Radiative transitions* consist in the absorption or emission of a photon (fluorescence and phosphorescence), depending on the direction in which the transition takes place, and they are drawn with straight arrows. *Non-radiative transitions*, which are depicted with wavy arrows, are of different types. *Vibrational relaxation* is the relaxation of the excited state to its lowest vibrational level. *Internal conversion* occurs when a vibrational state of an electronically excited state can couple to a vibrational state of a lower electronic state. *Intersystem crossing* is the transition to a state with a different spin multiplicity, which can bring to phosphorescence.

Following a photon absorption, many other pathways can compete with fluorescence. For example, there is a low probability that the electron undergoes an *intersystem crossing*. This transition implies a change in the spin multiplicity because the electron moves from an excited singlet state to a triplet state. From this, the electron decays with a forbidden-transition, emitting a photon of *phosphorescence* in a slower way than fluorescence.

Generally, a *fluorophore* is a molecule, which exhibits fluorescence upon light excitation. There are different types of fluorophores, each characterized by a *maximum absorption/excitation wavelength* and a *maximum emission wavelength*. These maxima correspond to the peak in the excitation spectrum and the peak in the emission spectrum, respectively. **Figure 1.2** shows the spectrum of fluorescein as an example. The reason for these two different peaks is that the molecule absorbs photons of a specific wavelength, and emits light always at a longer wavelength. Therefore, the emitted photon has lower energy than the absorbed one. This property of fluorescence is named the *Stokes shift*. The energy loss between excitation and emission finds its cause in the rapid decay of the excited electron to the lowest vibrational level of S_1 or in the fact that fluorophores often decay to higher vibrational level of S_0.

Furthermore, the emission spectrum is often specular to the absorption band, as the *mirror rule* states.

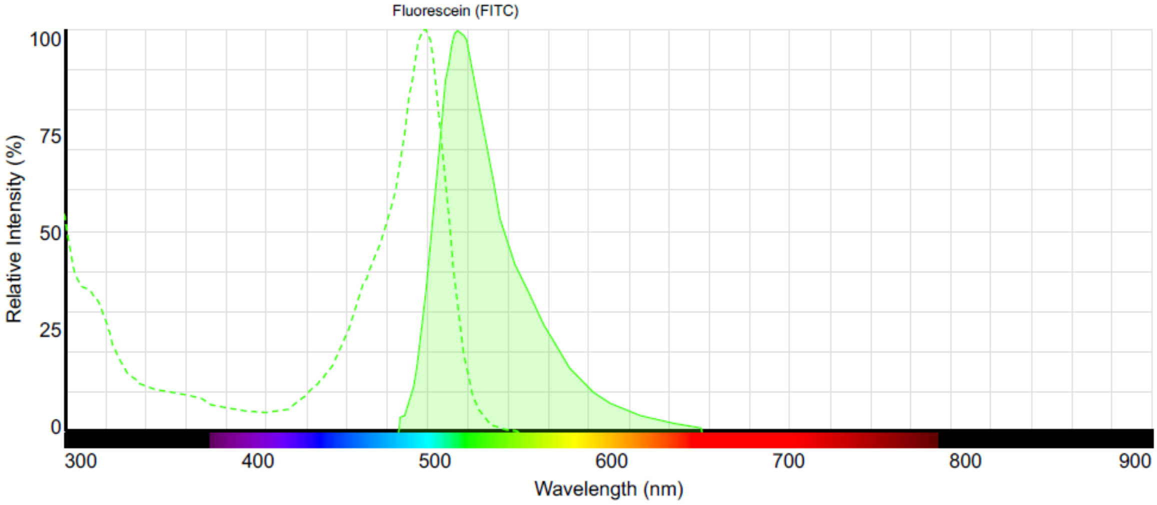

Figure 1.2 Absorption and emission spectra of fluorescein.

The fluorescence spectrum of fluorescein (FITC) shows the absorption peak at about 495 nm and the emission peak at about 518 nm. The spectrum was generated using ThermoFisher Scientific online tool "Spectra Viewer".

A main characteristic of fluorophores is the *molar extinction coefficient* (ε) expressing how strongly a species absorbs light at a given wavelength. It also links the absorbed light at that wavelength to the concentration of the fluorophore in solution.

Another property of fluorophores is the *quantum yield* (Φ) that gives a measure of the fluorescent process efficiency. The quantum yield can be defined as the fraction of excited molecules that return to the ground state emitting fluorescence or as the ratio of the number of photons emitted to the number of photons absorbed:

$$\Phi = \frac{number\ of\ photons\ emitted}{number\ of\ photons\ absorbed}$$

The brightness of a fluorophore is the number of photons emitted by the molecule, and it is proportional to the product of the extinction coefficient and the quantum yield.

One more fluorescence feature is the *fluorescent lifetime* that is the average time a fluorophore spends in the excited state before returning to the ground state. The fluorescent intensity of a population of molecules decreases exponentially with a distinctive time, which reflects the average lifetime of fluorophores in the excited state. Along with the quantum yield, the fluorescent lifetime of a fluorophore is drastically affected by the surrounding environment (Lakowicz, 2006).

1.1.2 Fluorescence optical microscopy

The fluorescent phenomenon has been exploited to increase the contrast between the signal and the background in optical microscopy.

Classical optical microscopes use transmitted white light and optical components, like lenses and mirrors, to illuminate and magnify the object. The contrast between different structures in the specimen is due to the dissimilarities in light absorbance. Unfortunately, biological samples show low contrast so that the resulting image will exhibit a low signal-to-noise ratio. Moreover, transmitted-light based microscopes do not allow to distinguish different structures or organelles characterized by similar light absorbance values, except through the shape or optical density (Born and Wolf, 2013). Consequently, the purpose of technical improvements in microscopes over the years aimed to reveal only objects of interest in biological samples, enhancing contrast and specificity.

It was not until the beginning of the 20th century that histologists, like Camillo Golgi and Santiago Ramón y Cajal, started to stain specimens with substances able to recognize precise biological structures and absorb light at a specific wavelength to improve contrast, thus propelling the development of fluorescence microscopy.

The characteristic that makes fluorescence so sturdy is the Stokes shift. In fact, because of the difference in wavelength between absorption and emission, it is possible to filter out the excitation light and detect only light coming from fluorescing molecules. In this way, even a single fluorescent molecule is visible if the background does not manifest autofluorescence (Lichtman and Conchello, 2005).

Fluorophores

Over the years, a vast spectral array of fluorophores has been developed, exploiting natural or synthetized molecules that have some degree of conjugated double bonds or, even better, aromatic rings. These kinds of molecules are ideally suited for fluorescence microscopy because the energy differences between the ground state and the excited state orbitals are slight, and electrons can be excited by relatively low-energy photons in the visible spectrum. The availability of fluorescent labels with a significant quantum yield and different excitation and emission wavelengths along the entire visible spectrum allows simultaneous imaging of different cellular or subcellular structures, even molecules. In addition, most of the fluorophores permit to label specifically a variety of cell components. For example, the *DNA-binding dyes* intercalate between DNA bases or *membrane-binding dyes* bound lipids in cell membranes. Otherwise, *immunofluorescence staining* is a good alternative. This technique exploits the highly specific binding of a labeled antibody to its antigen to attach a fluorophore to the protein of interest. In addition, several *fluorescent proteins* may be genetically fused to a protein of interest, thus allowing the direct visualization of a target molecule inside living cells (Chalfie et al., 1994).

The fluorescence microscope

As mentioned before, a fluorescence microscope takes advantage of the Stokes shift principle to collect only the fluorescent signal originating from the specimen. The basic idea is to illuminate the sample with a given excitation wavelength and filter the emission light, which is at a longer wavelength.

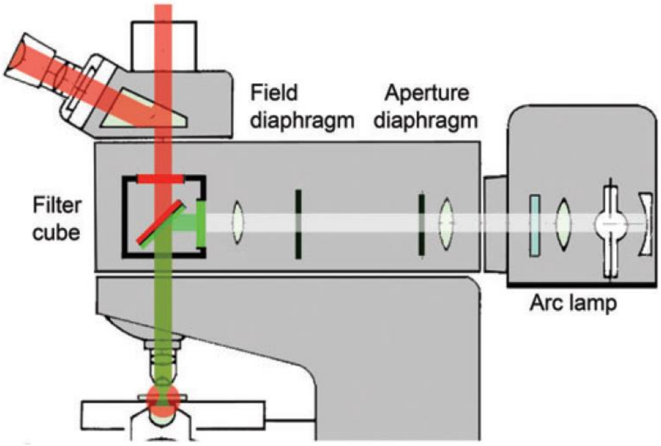

Figure 1.3 The epifluorescence microscope.

The epi-illumination fluorescence microscope is equipped with a multispectral light source (in this example an arc lamp). In order to select the required excitation wavelength, the light pass through an excitation filter, which is part of a cube-shaped filter. The excitation light is therefore reflected by the dichroic mirror and then it pass through the microscope objective, which acts as a condenser of the excitation light, reaching the specimen eventually. The resulting fluorescent light sends photons in all directions and a fraction of them is gathered by the objective and convey through a barrier filter in the cube to the detector. This last filter prevents the exciting wavelengths from reaching the camera (Lichtman & Conchello, 2005).

Modern fluorescence microscopes exploit the approach called *epifluorescence illumination*. The epifluorescence illumination configuration (**figure 1.3**) consists in lightening the sample with a defined wavelength produced by filtering the full-spectrum light from a light source, for example, an arc lamp. The light, coming from the lamp, reaches a *cube-shaped filter*, which selects the excitation wavelength. This cube has three components with specific spectral features: a filter that selects the excitation light, a dichromatic mirror, also called dichroic or beam splitter, and a barrier filter. The filter cube is fundamental since in epifluorescence microscopes, the exciting light and the emitted fluorescence overlap in the light path. The surface of a dichroic mirror reflects the selected wavelength, illuminating the specimen through the microscope objective that acts as a condenser in order to concentrate light onto the specimen. At this point, the fluorescence emitted by the sample and gathered by the objective returns through the objective to the dichroic where it passes through the emission filter, which rejects the excitation light.

The application of lasers as excitation light sources for fluorescence microscopy provided narrow-size sources with low divergence and monochromaticity. In addition, lasers have become indispensable in scanning confocal microscopy, a technique developed in the 50s (Minsky and Minsky, 1961). Confocal microscopy has introduced several advantages over conventional microscopy, overcoming some of the limits of traditional fluorescence microscopes named *wide-field microscopes*. In a wide-field microscope, the whole sample is evenly illuminated by the light source, such that every fluorescent molecule may fluoresce from each part of the specimen. The *laser scanning confocal microscope* (LSCM) uses a pinhole positioned in an optical conjugated plane in front of the detector, in order to reject out-of-focus fluorescent signal. In this way, the detector will receive only photons emitted by the fluorophores in the focus plane. Since one point at a time is illuminated, the laser beam is required to scan the sample.

Drawbacks of fluorescence microscopy

If, on one hand, the employment of fluorophores improves specificity, contrast, and selectivity of light microscopy with respect to other optical techniques, on the other hand, it also presents some drawbacks like fluorescence *fading* and *phototoxicity.*

Fading is mostly due to two phenomena: quenching and photobleaching. *Quenching* is one of the possible non-radiative pathways by which the energy of the excited state can be dissipated. It competes with the emission of photons and thus results in fluorescence intensity loss. Quenching can occur by different mechanisms, such as collisions, excited state reactions, or energy transfer. A variety chemicals can act as fluorescence quenchers, including iodide ion, oxygen, and acrylamide (Lakowicz, 2006).

Photobleaching consists in the permanent alteration of photochemical properties of a fluorophore that ceases to fluoresce. While quenching is a reversible loss of fluorescence owing to non-covalent interactions between the fluorophore and surrounding molecules, the term photobleaching indicates a process that causes the fluorescence emission to fade irreversibly, owing to covalent modifications of the fluorophore. Usually, it occurs because of the transition from the excited singlet state to the triplet state of the fluorophore, followed by the reaction of the triplet state with molecular oxygen. Molecular oxygen itself is a triplet in the ground state; therefore, a transfer of energy can occur between the two species. This energy brings the oxygen in the excited singlet state, a strong reactive molecule, which can cause various chemical reactions, altering the fluorophore covalently. Moreover, the singlet oxygen may also react with other organic molecules resulting in *phototoxicity* for cells (Lichtman and Conchello, 2005).

Although microscopists usually attempt to minimize damages deriving from it, sometimes photobleaching turns out to be useful, for example, to quench autofluorescence before staining the specimen. In addition, it has been exploited in techniques like FRAP (*fluorescent recovery after photobleaching*) or FLIP (*fluorescence loss in photobleaching*) where bleaching plays an indispensable role in studying motion and diffusion of macromolecules or cellular components inside the cell.

1.2 Optical microscope resolution and diffraction limit

The resolving power is the most crucial characteristic of an optical system since it determines the capability to distinguish fine details in a specimen. By definition, the *resolution* is the smallest distance at which two points on the imaged object can be still distinguished by the detection device (observer eye or microscope camera). The resolution can be affected by many factors as aberrations, incorrect alignment of the microscope components, the numerical aperture of the objective and the condenser, and the light wavelength.

Despite all the technological advancements and manufacturing breakthroughs developed over the years that have led to significantly improved optical microscopes, their resolution is limited owing to the diffraction of visible light wavefronts as they pass through a circular aperture. As a result of the wave properties of light, the image of a point source formed by a perfect objective lens is always a diffraction pattern composed by a bright central discoid region, commonly called Airy disk, with an alternating series of bright and dark diffraction rings whose intensity decreases (Airy, 1835). The result is an image of the point source that is larger than the actual size of the object. Hence, the resolution of a light microscope refers to its power to distinguished two close-range Airy disks in the diffraction pattern.

The finite dimension of the central spot of the diffraction pattern is intrinsically dependent on the numerical aperture (*NA*) of the objective, that is equal to the refractive index of the immersion medium (n) multiplied by the sine of the aperture angle (θ), and the excitation wavelength (λ):

$$d_{xy} = \frac{\lambda}{2\,NA} = \frac{\lambda}{2\,n\,sin\theta}$$

This expression corresponds to the *Abbe's limit of diffraction*. Ernst Karl Abbe was a German physicist who published his theory in 1873, which explained the resolution limits of a microscope. As images consist of an ensemble of diffraction-limited spots overlapping each other, the only way to optimize the resolution is to increase the numerical aperture or the medium refractive index and to decrease the illumination wavelength in order to minimize the size of the diffracted spots (Abbe, 1873). Nevertheless, even if a microscope is provided with the best quality optical components, the resolution is still limited to about half the wavelength of visible light, 200-250 nanometers, in the focal plane (xy). This is the current lateral resolution achievable with a wide-field microscope, while the axial resolution (z axis) is even worse, ranging on the order of 500 nanometers, according to the Abbe's equation:

$$d_z = \frac{2\,\lambda}{NA^2}$$

It is common to refer to the conventional optical limitations of fluorescence microscopy with the term "*diffraction barrier*".

The degree of blurring of a point light source is a measure of the quality of an optical microscope, and it is usually denoted with the *Point Spread Function* (*PSF*), a characteristic of each microscope. The PSF describes the response of the microscope to a point light source, and it is the three-dimensional diffraction pattern of the light emitted by the source, with x-y full width at half maximum (FWHM) corresponding to the Abbe's limit (**figure 1.4**).

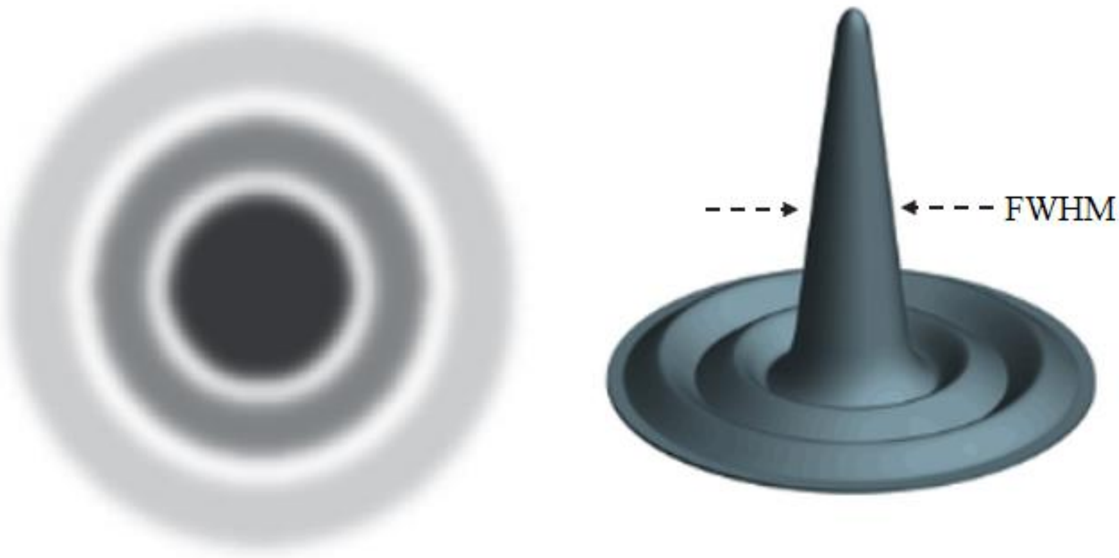

Figure 1.4 Diffraction pattern and Point Spread Function.

Consequently, when imaged with a microscope, a point object will appear as the convolution of the point object real spatial distribution with the PSF (**figure 1.5**).

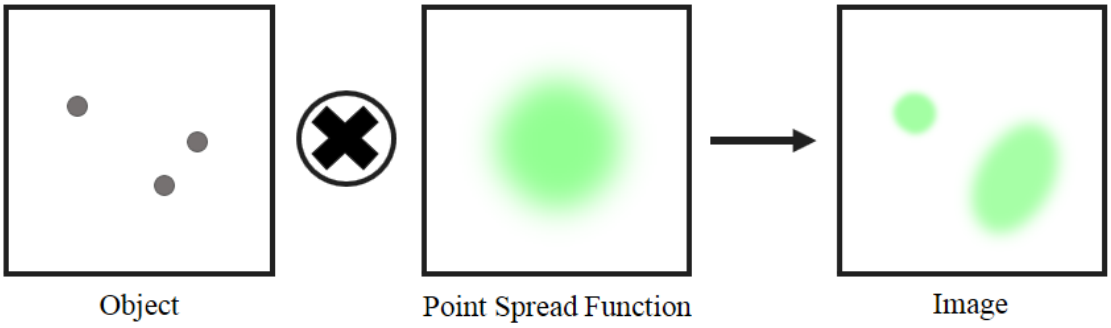

Figure 1.5 Convolution of the real spatial distribution of the imaged object with the PSF.

1.3 Super-resolution microscopy

Optical microscopes are intrinsically limited in spatial resolution to roughly half the wavelength of visible light, because of diffraction. All the fluorophores, closer to each other than the diffraction limit, are indistinguishable.

For a long time, this resolution limit seemed impossible to overcome. Despite the several technological improvements achieved over the years in the field of fluorescent microscopy, such as *total internal reflection* (TIRF) (Axelrod, 1981) or *two-photon excitation microscopy* (2PEF) (Denk et al., 1990) that surpassed the imaging limitations of thick samples, the only way to gain high spatial resolution remained *electron microscopy* (EM) for decades. Notwithstanding, EM presents many practical issues that restrict its applicability in the biological field. Although EM can achieve atomic resolution, it requires specimens to be in vacuum and difficult sample preparation (fixation, dehydration, and sectioning) that do not allow live-cell imaging. Moreover, images obtained with EM may often result in artifacts (Leung and Chou, 2011). Instead, fluorescent optical microscopy is a powerful tool in life science, thanks to the almost negligible effect of visible light on living samples, high molecular specificity through targeted labeling, and multi-labeling ability that permits to get multi-color imaging.

During the last years, many efforts have been made to overcome the resolution limit imposed by physical laws, trying to bypass the “diffraction barrier” of far-field optical microscopes. These efforts led to the development of better-resolved, but still diffraction-limited, imaging techniques such as the already mentioned confocal scanning microscopy (page 9) or the *structured illumination microscopy* (SIM) (Gustafsson, 2000). The latter is based on wide-field microscopy and improves lateral resolution by up to a factor 2 in respect to the epifluorescence microscope, without the need to limit imaging speed by scanning the sample as in confocal microscopy. In SIM, the sample is illuminated using a known structured pattern of light, typically sinusoidal stripes produced by the interference of two beams split by a grating. When the fluorescent sample is illuminated with such a fine structure, it will produce Moiré fringes that are recorded by the microscope. Since the periodicity of a Moiré pattern is lower than the array of illumination lines, by acquiring a series of images for different phases and orientations of the illumination pattern, it is possible to reconstruct the image with an enhanced lateral resolution.

1.3.1 Breaking the diffraction barrier

The diffraction barrier was shattered with the advent of *super-resolved fluorescent microscopies* developed separately by Stefan W. Hell, Eric Betzig, and William E. Moerner, who received the Nobel Prize in Chemistry in 2014. The achievement of super-resolution microscopy, also called *nanoscopy*, allowed the optical microscope to peer into the nanometric universe. The trick to deceive the diffraction limit relies on the ability to discern fluorescent molecules residing within the same sub-diffraction region, preventing them from being detected together. Super-resolution techniques accomplish this goal by two main families of approaches exploiting different concepts: the targeted read-out approach based on patterned illumination to engineer the PSF, and the approach based on stochastic switching of fluorophores and single-molecule detection.

1.3.2 Targeted read-out methods

The first strategy to achieve super-resolution relies on *spatially targeted methods* that consist in using patterned illumination to narrow the size of the fluorescent spot, the PSF, by modulating the fluorescence emission of most of the fluorophores within a diffraction volume, in order to achieve separate detection of molecules.

These techniques include *stimulated emission depletion* (STED) (Hell and Wichmann, 1994; Klar and Hell, 1999), *ground-state depletion* (GSD) (Hell and Kroug, 1995), and *saturated structured illumination microscopy* (SSIM) (Gustafsson, 2005).

STED microscopy was the pioneering method in this subgroup of super-resolution techniques. This approach exploits the concept of stimulated emission to deplete the fluorescence emission of fluorophores in the peripheral part of the illumination spot to reduce the broadness of the fluorescent spot. In detail, the sample is scanned with two laser beams: an excitation laser diffraction-limited and a red-shifted depletion laser shaped like a donut, thanks to a vortex phase plate. Both beams are diffraction-limited, but fluorescence emission of molecules located within the area of the STED beam is suppressed, since these fluorophores are transferred back to their ground state by stimulated emission, and only fluorophores at the center of the donut are able to emit fluorescent light. In this way, the size of the final fluorescent spot is sharpened, and a later resolution measured in tens of nanometers can be achieved (**figure 1.6**).

Microscopies exploiting excitation patterns are generalized to *reversible saturable optically linear fluorescence transitions* (RESOLFT) (Hofmann et al., 2005), including any stimulated transition between to molecular states in addition to stimulated emission.

Non-linear SIM or *saturated SIM* (SSIM) also achieves a higher resolution than that obtained by linear SIM, by following the concept of RESOLFT microscopy. This technique combines SIM with strong illumination intensities (Gustafsson, 2005) or photoswitchable fluorophores (Rego et al., 2012).

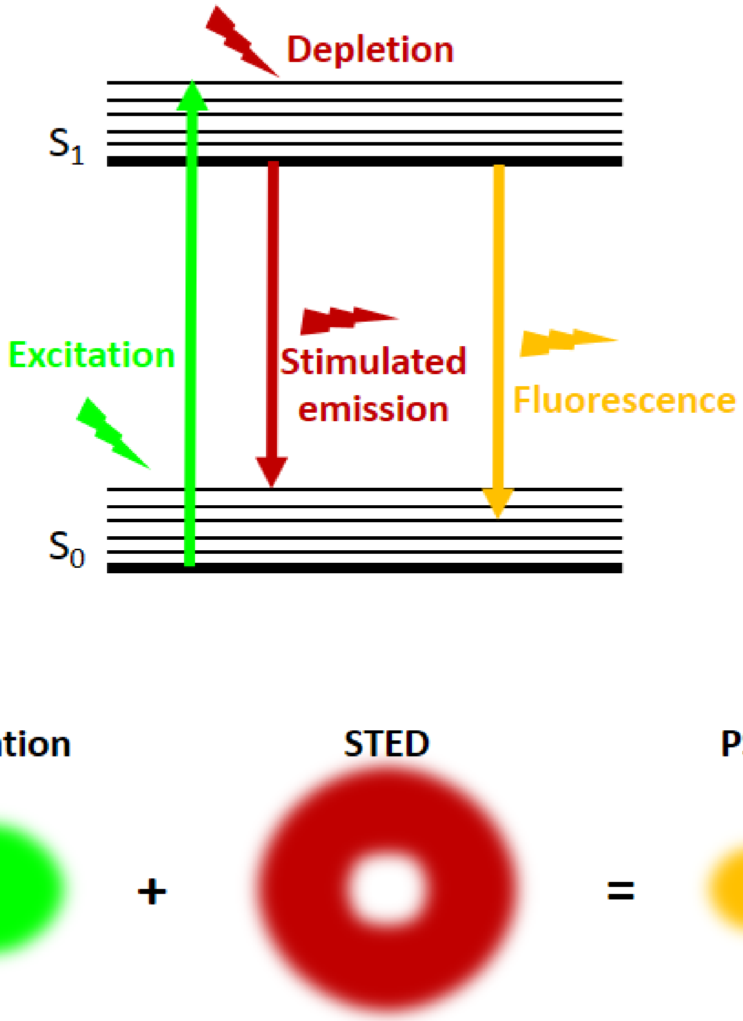

Figure 1.6 Schematic representation of STED principle.

The schematic shows the Jablonski diagram of fluorescence emission and stimulated emission and the superimposition of the donut-shaped STED beam to the excitation spot. In the peripheral region of the fluorescent spot, where the STED beam has its maximum intensity, the phenomenon of stimulated emission occurs. The redshift of the stimulated photon allows to ignore its wavelength when fluorescence is collected, leading to a reduction of the PSF.

1.3.3 Stochastic switching of fluorophores

The second approach to circumvent the diffraction limit is based on *stochastic switching of molecules* between two fluorescent states, usually a fluorescence emitting “on” state and a non-fluorescent “off” state, and localization of the fluorophore positions.

The underlying principle is that although PSF of a single emitter is always much larger than its actual size, the location of the fluorophore can be determined to nanometer precision if a sufficient number of photons are collected, and there are not any other molecules emitting at the same wavelength within ~ 200 nm.

Since in all these methods the molecule positions are inferred from photons emitted by single molecules, they are named *single-molecule localization microscopies* (SMLMs) (Betzig, 1995; Moerner and Kador, 1989). They include *stochastic optical reconstruction microscopy* (STORM) (Rust et al., 2006), *photoactivated localization microscopy* (PALM) (Betzig et al., 2006), fluorescence *photoactivated localization microscopy* (FPALM) (Hess et al., 2006), *points accumulation for imaging in nanoscale topography* (PAINT) (Sharonov and Hochstrasser, 2006).

However, the ability to localize accurately single molecules does not automatically translate in super-resolved imaging of samples labeled with fluorescent probes. Especially in the case of densely labeled samples, the diffraction-limited images of fluorophores will overlap, preventing their localization. SMLM overcome this issue by exploiting the photochemical properties of *photoswitchable probes* that can stochastically switch between an emitting state and a dark state (Bates et al., 2005; Patterson and Lippincott-Schwartz, 2002). By sequentially switching on and off these photoswitchable probes in a stochastic manner, it is possible to detect ideally small and spatially sparse subsets of fluorophores on the imaged sample. This is the fundamental principle underlying techniques such as PALM and STORM. They differ from each other in the employed fluorescent probes: PALM uses photoactivatable fluorescent protein expressed in the form of genetic fusion constructs to the protein of interest. In STORM, instead, is performed the immunolabeling of endogenous proteins with antibodies covalently bound with organic fluorophores.

A different version of stochastic state switching of fluorescent probes is PAINT that relies on transient binding of fluorophores that are turned “on” when reversibly attach to the targets in the sample, while the other moving unbound fluorophores stay in an “off” state.

1.3.4 Other super-resolution techniques

Recently a new technique that combines strength form both approaches has been developed. This method, named *nanoscopy with minimal photon fluxes* (MINFLUX) (Balzarotti et al., 2017), exploits stochastic switching of fluorophores to enable detection of adjacent molecules combined with patterned illumination to achieve 1 nm localization precision of molecules by detecting local minima of fluorescent emission.

Another super-resolution technique called *expansion microscopy* (ExM) (Chen et al., 2015; Chozinski et al., 2016) that improves resolution by mechanically expanding the specimen to allow features closer than the diffraction limit of light to become resolvable. The method entails the staining of a specimen with polymer-linkable probes, growth of a swellable polymer within the specimen that links to the probes, protease digestion of the specimen, and eventually the expansion, resulting in physical magnification.

A detailed explanation of every super-resolution microscopy is beyond this thesis. In the next paragraphs, we will focus on the description of the operating principles, instrumentations, and capabilities of the STORM technique used in our work to address biological issues at a quantitative nanoscale level.

1.4 Stochastic optical reconstruction microscopy (STORM)

As mentioned before, all the SMLMs are based on the same concept: the reversible transition between bright and dark states of photoswitchable or photoactivable fluorescent probes. SMLMs take advantage of this switching behavior of special organic dyes, fluorescent proteins, or quantum dots, to resolve molecules separated by less than half the wavelength of excitation light, allowing users to acquire nanoscale information. The basic idea is that, instead of trying to distinguish spatially close fluorescent molecules, they can be switched “on” at different times.

Among the SMLMs, *stochastic optical reconstruction microscopy* (STORM) (Heilemann et al., 2008; Rust et al., 2006) exhibits several advantages, relying on the use of standard organic fluorophores, of a rather simple instrumentation and allowing to achieve a resolution of the order of tens of nanometers (**figure 1.7**).

In substance, STORM lays on the sequential and stochastic read-out and localization of multiple single molecules from specimens that were labeled with photoswitchable dyes.

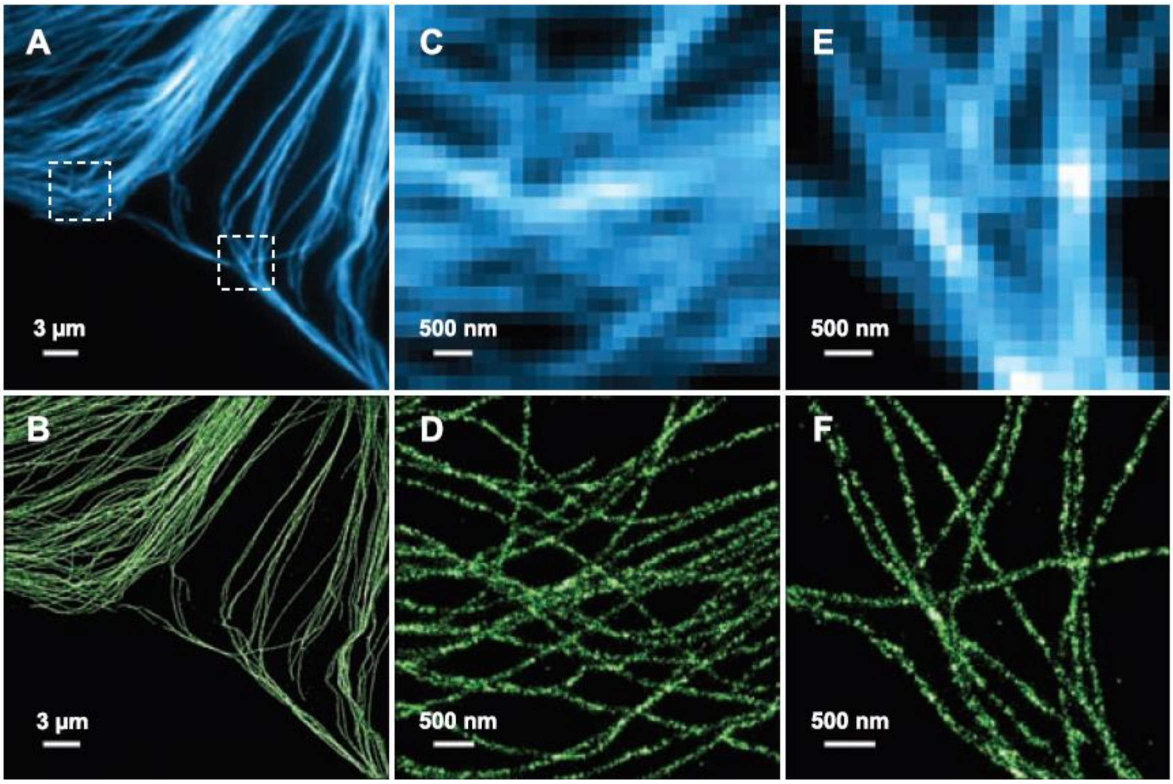

Figure 1.7 Wide-field vs STORM imaging of microtubules in mammalian cells.
(Bates et al., 2007)

In a typical STORM imaging routine, a weakly emissive or non-emissive state of fluorophores attached to the structure of interest is induced. From this “dark state”, an ideally very small and sparse subset of fluorophores is sequentially brought back to the fluorescence emitting state and detected. The centroid position of each imaged molecule is statistically fitted, usually with a Gaussian distribution, by localization algorithms, and with a localization precision that scales with the number of detected photons. By collecting localization data for thousands of frames of sparse single molecules populations, it is eventually possible to reconstruct the super-resolution image (**figure 1.8**).

However, an excellent performance of STORM imaging is achievable not without unavoidable critical steps, in order to satisfy three crucial requirements: (i) the stochastic photoblinking of fluorescent probes to obtain sparsely distributed emitting molecules in the field of view, (ii) an accurate localization of single fluorescent molecules, and (iii) an appropriate labeling of structures of interest. As a consequence, the STORM user is bound to follow strict sample preparation protocols and to select the more adequate fluorescent probes. If any of these requirements are not fulfilled, a deterioration in resolution or image artifacts may occur.

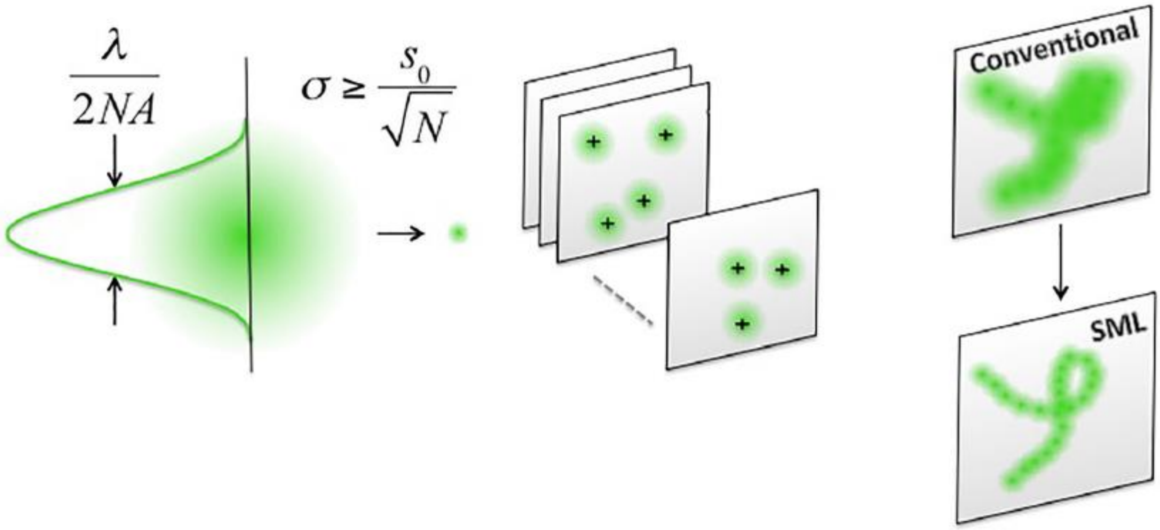

Figure 1.8 Schematic representation of the SML concept.

The position of a single emitter, isolated by means of stochastic photoswitching of fluorescent probes, is determined by fitting the photon distribution with a Gaussian approximation of the PSF, with a localization precision improving with a higher number of detected photons. The iteration of this process for thousands of subsets of sparse molecules allows collecting enough localization data to reconstruct an image with a resolution 10-fold better with respect to wide-field fluorescence microscopy (Magrassi et al., 2019).

1.4.1 Features of STORM probes

The choice of the proper fluorophore for STORM imaging is a determinant of the performance of super-resolution imaging. To date, a large palette of fluorescent probes has been developed to be employed in super-resolution microscopy, but only a small group of them can successfully meet the requirements for SMLMs (Dempsey et al., 2011).

The selection of a probe for STORM measurements requires several considerations to be taken into account, beyond the standard ones for a good fluorophore, such as photostability.

Photochemistry and photophysics

The German physicist Werner Heisenberg was the first to introduce the concept of single-molecule localization in the 1930s (Heisenberg, 1930), and in the 1980s, this principle was experimentally demonstrated (Gelles et al., 1988). STORM imaging exploits the concept of single-molecule detection to overcome the diffraction limit and reconstruct images of biological samples at the nanoscale. To achieve this, STORM fluorescent probes are induced to cycle randomly between “on” and “off” states during image acquisition. These switching cycles allow avoiding simultaneous emission of spatially close fluorophores and the consequent overlapping of fluorescence emission profiles.

Synthetic dyes suitable for STORM imaging belong to different structural families. Usually, red-shifted dyes perform better. Most of them are cyanine and rhodamine derivatives (**figure 1.9**), but there are also xanthene and oxazine derivatives. All these molecules are characterized by a conjugated π-electron system that provides the molecule with its light absorption properties. The unique spectral properties of each dye are determined by the length of the π-conjugated system, the number of electrons, and different functional groups, including the ability to switch reversibly between a dark and a bright state (Klessinger, 1978).

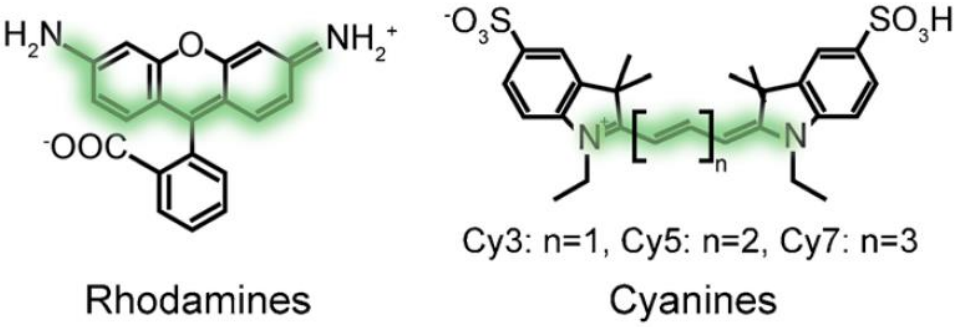

Figure 1.9 Principal STORM synthetic dyes structures.
(Turkowyd et al., 2016)

The particular behavior of these photoswitchable probes is commonly named *photoblinking*. The photophysical mechanism underlying the fluorescence blinking is the transition of the excited molecule from the excited singlet state (S_1) to the triplet state (T_1), which has a lifetime longer than S_1. The triplet state is a metastable and weakly fluorescent state because the molecule does not emit fluorescence and cannot be excited during the time residing in it (**figure 1.10**). From the triplet state, many fluorophores can be reduced to a dark and stable radical state (R*). In order to push most of the fluorophores in the dark state, it is used a strong excitation laser power (~ 200 mW) and a proper reducing agent. From the triplet state, molecules go back to the ground state, and this process can be tune upon irradiation with UV light at 405 nm.

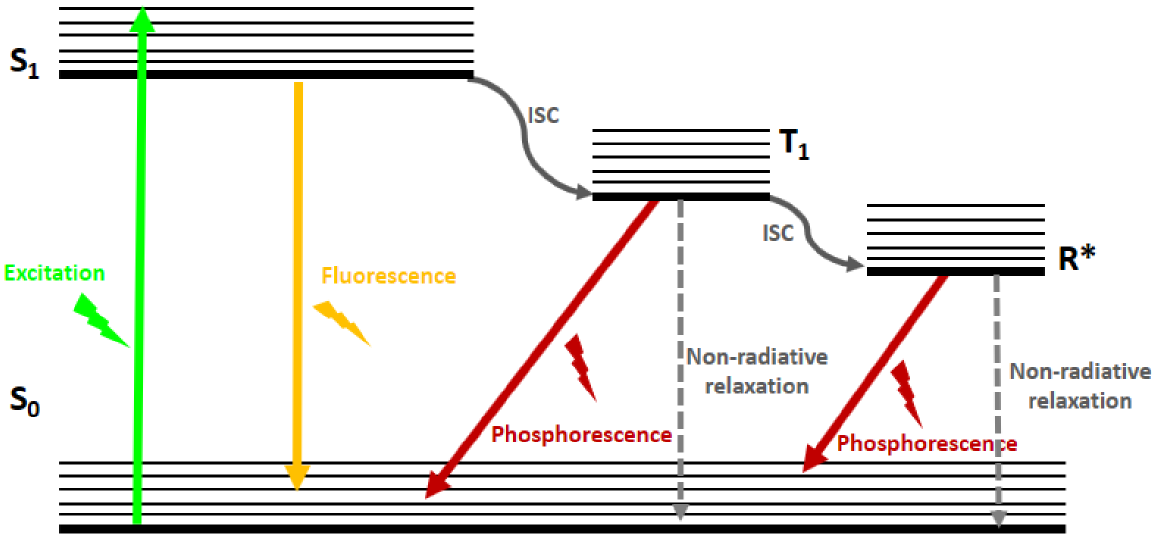

Figure 1.10 Simplified Jablonski diagram showing the mechanism of blinking of STORM dyes.

By absorption of a photon, an electron from the ground state (S_0) can be excited to the excited state (S_1), preserving the spin pairing with the ground state partner. The excited electron can relax by fluorescence emission or can undergo an intersystem crossing transition to the weakly fluorescent triplet state (T_1), inverting its spin. For this reason, the intersystem crossing is a forbidden transition. From the T_1, the molecule relaxes in a longer lifetime than fluorescence lifetime, and return available to be excited, by phosphorescence emission or non-radiative relaxation. In the presence of an appropriate buffer solution, it can also undergo intersystem crossing into a stable, dark, and long-lasting radical state (R*) by chemical reduction of the fluorophore.

Duty cycle

In order to obtain spatial and temporal separation of the fluorophores, it is necessary to use probes characterized by a low duty cycle. The *duty cycle* is the ratio of time a fluorophore spends in the bright state compared to the time it spends in the dark state. A probe with a high duty cycle spends much time in the fluorescent state, so it is more difficult to localize the fluorophores because they stay in the “on” state for too long, and several molecules can be fluorescent at the same time. Instead, a probe with a low duty cycle spends more time in the non-emissive state and minimize false multiple-fluorophore localizations (Dempsey et al., 2011).

Switching cycle

The need to use high laser powers to force fluorophores to the triplet state implies the risk of permanent photobleaching of the molecules. Therefore, it is of enormous importance to select fluorescent probes that can undergo a large number of switching cycles before photobleaching. The average number of switching cycles a probe can experience depends mostly on the molecule chemistry; for example, the synthetic dyes commonly used for STORM are able to undergo more cycles than the fluorescent proteins used for other SMLMs. Still, it can be controlled by experimental conditions, such as the employment of the right imaging buffer.

Switching kinetics

Along with the average number of switching cycles, another crucial feature of a probe for STORM imaging is the switching kinetics that is the time the fluorophore takes to move to the triplet state after excitation. The camera rate needs to be tuned up to the switching rate of the probe to ensure that molecules stay in the bright state for no longer than one frame of read-out. So, the switching kinetics determines the acquisition time, since probes with faster kinetics lead to a faster collection of localization data (Dempsey et al., 2011).

For most STORM probes, the switching kinetics is directly proportional to the excitation laser power.

Brightness

As already mentioned, and as it is explored in the next paragraph, the number of photons emitted is a key feature of a fluorescent probe for STORM imaging, since probes with high photon output provide better localization precision (Thompson et al., 2002).

Moreover, higher brightness ensures a better signal to noise ratio, since the detected fluorescent signal is greater than the fluorescent background, leading to a better outcome of imaging.

1.4.2 Spatial resolution of STORM

The resolving ability of the STORM technique is strictly dependent on the precision with which fluorescent molecules are localized. However, the spatial resolution is affected by several other factors, such as the labeling density, the probe size, and the sample drift.

Localization precision

Although the photons emitted by the probes are distributed in finite-size spots when captured on the microscope camera, they can be localized with high precision, provided enough photons are detected. In fact, each captured photon provides an independent measurement of the fluorophore position. Image-processing methods for determining molecular localization coordinates generally rely on statistical fitting algorithms. Gaussian function is typically used to approximate the photon distribution, to determine its mean value, that corresponds to the localization coordinates of the fluorophore, and the standard error in the fitted position (σ), that corresponds to the *localization precision* and is expressed by the following equation (Thompson et al., 2002):

$$\sigma = \sqrt{\frac{s^2}{N} + \frac{a^2/12}{N} + \frac{4\sqrt{\pi}s^3b^2}{aN^2}}$$

where *s* is the width of the Gaussian function approximating the PSF of the probe, *N* is the number of collected photons, *a* is the pixel size, and *b* is the background noise. Therefore, the localization accuracy does not depend only on the number of photons, but the effect of a finite pixel size must also be taken into account, as well as the fluorescence background and the detector noise.

In the case of negligible background noise compared to the fluorescent signal, assuming a pixel size of ~ 100 nm and a photon output of ~ 1000, it is possible to achieve a localization precision of approximately 10 nm.

Labeling density

The other parameter that limits the resolution in localization microscopy is the labeling density. Localizing fluorophores with high localization precision is not sufficient to reach optimal resolution if the labeling fails to tag each molecule of interest, leading to a loss of details (**figure 1.11**).

The *Nyquist criterion* provides a guideline to define a reliable labeling density of a structure. This criterion states that the distance between two neighboring emitters must be smaller than half of the smallest sample feature that can be resolved (Shroff et al., 2008). However, in the case of a sample with sparse molecules of interest, this criterion cannot be applied, and the criterion leads to an overestimation of the improvement of resolution with the label density (Fitzgerald et al., 2012).

Optimizing the labeling density by following strict sample preparation protocols and choosing the right labeling and high-quality antibodies ensure a better imaging performance and better spatial resolution.

Probe size and labeling strategies

The size of the probe is another crucial point that can alter the resolution of the STORM image (**figure 1.10**). Although the synthetic dyes usually employed in STORM microscopy have a size around 1 nm, they are generally attached to the protein of interest by *indirect immunolabeling*. This means that they are bound to a secondary antibody, which in turn binds a primary antibody on the target protein. Immunoglobulin G (IgG) antibodies (Weber et al., 1978) are typically around 10-15 nm big. Therefore they are of the same size order of the localization precision. Unavoidably, IgG size has an impact on the spatial resolution, preventing the user from realizing the full resolution potential of STORM. An alternative option is to label the target protein by *direct immunolabeling*, where the fluorescent probe is attached directly to the primary antibody. However, this approach necessitates that the user conjugates the primary antibody with the chosen dye since primary antibodies are commercially available as non-labeled IgG. Moreover, the indirect approach has the advantage to allow using different secondary antibodies to target any primary, produced in a compatible host animal.

Another valid alternative can be the employment of *F(ab) fragments* that are generated from IgG antibodies by enzymatic digestion and are smaller than the entire antibodies (~ 5-6 nm). Further alternatives are *nanobodies* or single-domain antibodies, with a size of ~ 4 nm (Ries et al., 2012). The small size of nanobodies leads to a decreased steric hindrance so that protein epitopes ordinarily inaccessible to larger antibodies can be reached more easily.

Another strategy is the expression of GFP- or RFP-fusion proteins and their labeling with anti-GFP or anti-RFP secondary antibodies conjugated to a photoswitchable probe. However, this approach implies transfecting cells that could be challenging, and not labeling of native proteins.

Eventually, the targeting of organic dyes using *SNAP*, *CLIP*, or *HALO-tags* (~ 3-4 nm) (Gautier et al., 2008) or direct labeling of specific markers that bind to membranes or organelles, DNA, or the use of *click-chemistry* (Laughlin et al., 2008) may reduce the probe size.

In our experiments, we have preferred to use indirect immunolabeling because of the need to tag multiple targets at the same time in primary cells like neurons makes this method the most suitable.

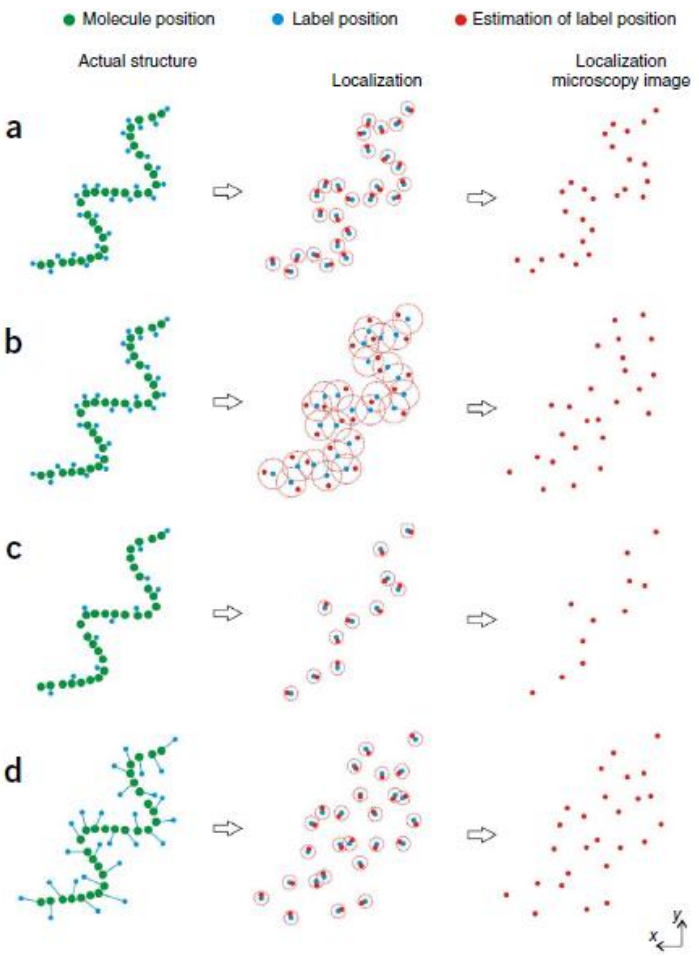

Figure 1.11 Influence of localization precision, labeling density and probe size on STORM resolution. Green dots symbolize molecules in the actual structure, and the labels are indicated as blue dots. The red circles and the red dots represent the localization precision and the estimation of the label position, respectively. **(a)** When the localization precision and the labeling density are sufficiently high, and the label displacement is small, SMLMs reliably represent the actual structure. The accuracy in SML imaging decreases drastically in the case of lower localization precision **(b),** lower label density **(c)**, or higher label displacement **(d)** (Deschout et al., 2014).

1.4.3 STORM modalities

Multicolor imaging

One of the most significant advantages of fluorescence microscopy is the ability to label different molecules inside the cell to study their relative organization and the possible interactions and co-localization between them. Multicolor stochastic optical reconstruction microscopy is still a challenging task. Relying on the photoswitching behavior of organic dyes, multicolor STORM requires employing two or more chromatically distinguishable probes. Moreover, they have to be able to switch appropriately between dark and bright states in the same imaging environment (i.e., imaging buffer, activation laser power, camera exposure time, etc.). Although several photoswitchable dyes spanning on an extensive spectral range have been developed and are readily available commercially, they generally have different buffer requirements. Moreover, chromatic aberrations cause different wavelength fluorescent signals to be focused at different points. Therefore, performing multicolor STORM using spectrally distinct dyes, the so-called *direct STORM* (dSTORM), is extremely difficult.

Multicolor STORM can be performed utilizing *activator-reporter pairs*, consisting of an activator dye and a reporter dye covalent bound to a secondary antibody. At first, three pairs have been constructed with Cy3 acting as the activator, and three different carbocyanine dyes with distinct emission spectra acting as the reporters (Bates et al., 2007). The reporters can be reversibly switched “on” and “off”, with the assistance of the activator, when it is excited at its maximum of absorption. The underlying mechanism is not clear, but it results in a non-radiative transfer of energy from the activator to the reporter, facilitating the recovery of the reporter from the dark state to the fluorescent state. The excellent switching properties of the activator-reported pair Cy3-Cy5 was previously reported in a paper by Bates et al., stating that the reporter can be switched for hundreds of cycles before permanently photobleaching (Bates et al., 2005). The same activator dye can activate the three reporters, and their distinct emission spectra allow them to be distinguished by the detector (**figure 1.12**, left side). However, this approach for multicolor imaging still suffers from chromatic aberrations.

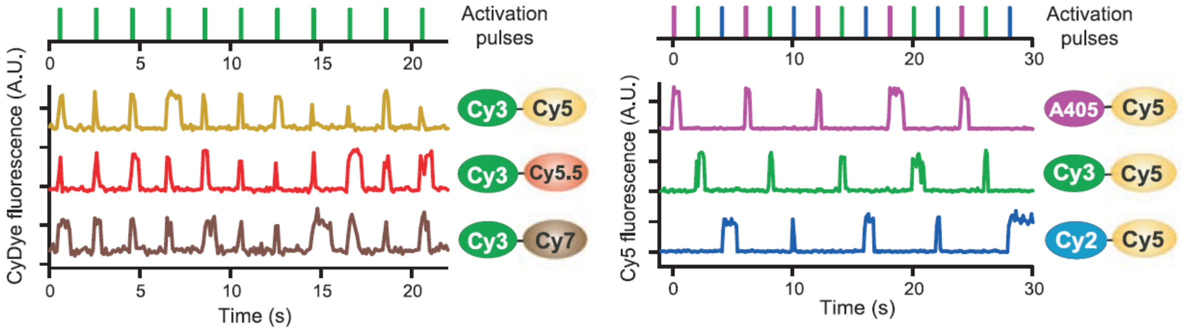

Figure 1.12 Three-color STORM imaging with activator-reporter dye pairs.

A possible approach to achieve multicolor imaging consists in the employment of dye pairs with different reporters and same activator (left side). A more valid alternative is offered by dye pairs with the same reporter and three different activators: by exciting the reporter continuously and the activators sequentially with the corresponding laser light, it is possible to collect all the three channels separately (Bates et al., 2007).

Another proposed option is to use dye pairs built with the same reporter dye, but different activator fluorophores (Bates et al., 2007). The activation of the reporter requires different-colored lasers corresponding to the absorption wavelengths of the activators. Hence, this approach allows separating channels by means of the distinct activation lights. While the excitation laser for the reporter is continuously on, one of the activators is excited with the proper laser, and only the paired reporter is imaged; then, another activator is excited, and its reporter is imaged, and so on (**figure 1.12**, right side). The result is that there are no chromatic aberrations because the fluorescence signals in the different channels are read-out at the same wavelength.

Nevertheless, this multicolor modality is exposed to inter-channel crosstalk, since the reporter dyes might blink independently of the activation lasers and be assigned to the wrong channel (Bates et al., 2012). Fortunately, post-processing methods based on statistical modeling have been developed to remove crosstalk (Bates et al., 2007; Dani et al., 2010). Moreover, dye-pair labeled antibodies are not commercially available and must be custom made.

3D STORM

Performing 3D STORM imaging implies to be able to determine the axial position of molecules in the sample. However, the fast switching kinetics of fluorophores precludes the acquisition of z stack, as usually performed in 3D microscopies.

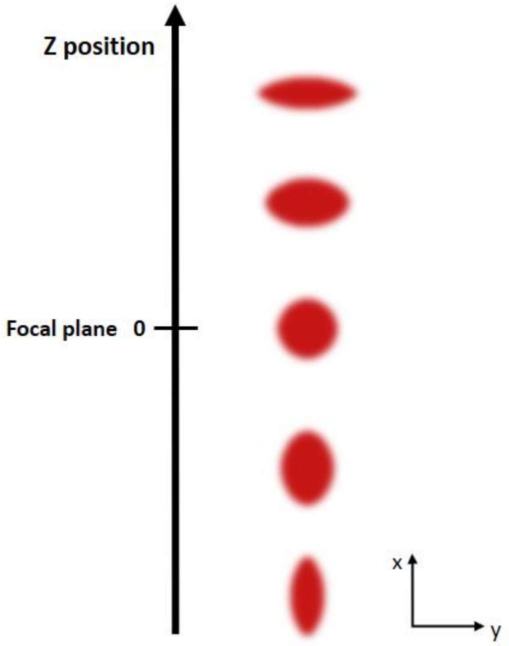

Figure 1.13 PSF astigmatism as a function of the z position of a single fluorescent molecule.

The positioning of a cylindrical lens in the optical pathway introduces astigmatism, inducing an elliptical deformation of the image of a single emitter as a function of its z position.

There are several different approaches to achieve 3D images with the STORM technique. The most straightforward and commonly used approach consists in introducing a cylindrical lens in the emission path to introduce astigmatism in the image of single emitters as a function of their z position. The PSFs of emitters positioned on the focal plane appear like a circular spot, whereas the PSFs of molecules above or below the focal plane are vertically and horizontally elongated, respectively (**figure 1.13**). By performing a calibration, the ellipticity (i.e., the width in x e in y) of the elongated PSF of each fluorophore provides a measure of its distance from the focal plane. The calibration curve can be obtained by using a piezoelectric stage and a sample of fluorescent beads and acquiring a stack of images at fixed z positions. With the astigmatic approach, it is possible to achieve an axial resolution of 50-60 nm over a range of ~ 1 µm (Huang et al., 2008).

Alternative approaches, achieving better axial resolution, include PSF engineering such as the method exploiting a spatial light modulator to generate a double-helix PSF containing two lobes whose angular orientation correlates with the axial position of the fluorophore (Pavani et al., 2009), or interferometric patterning like in iPALM (Shtengel et al., 2009). Still, the imaging depth is limited in this latter method. Recently, an approach based on Airy beams has been developed. This method employs a self-bending PSF, obtaining an isotropic three-dimensional localization precision of 10–15 nm over a 3 µm imaging depth (Jia et al., 2014).

In 3D images, the number of localizations acquired is lower with respect to 2D images. Then, it might not be the best choice in the case of low signal samples.

Live-cell imaging

Live-cell STORM imaging is complicated to achieve because of the imaging timescale. Only the imaging of slowly changing structures can be performed, as STORM requires the acquisition of thousands of frames to reconstruct the final image. Moreover, the addition of potentially toxic imaging buffers, which are commonly used to induce photoblinking, and the phototoxic effects stemming from the application of high power laser illumination, make using the STORM for live imaging even more complicated. Another critical aspect is the time response of the acquisition camera. The introduction of *scientific complementary metal-oxide-semiconductor* (sCMOS) detectors has enabled the acquisition of STORM data at higher rates than previously possible using slower read-out *electron multiplying charge-*

coupled devices (EMCCD). Finding a compromise between these aspects may lead to optimal super-resolved live-cell images (Lakadamyali, 2014).

Some recent works have demonstrated successful live-cell STORM imaging of different targets (Benke and Manley, 2012; Heilemann et al., 2009; Huang et al., 2013; Jones et al., 2011; Shim et al., 2012; Wombacher et al., 2010).

1.4.4 Experimental requirements for STORM imaging

The microscope

In terms of instrumentation, localization microscopy is relatively simple to realize, as it requires a good quality wide-field microscope with the addition of some necessary equipment:

i. Inverted microscope with *total internal reflection fluorescence* (TIRF) configuration. As seen before, SMLMs are sensitive to background signals since localization precision is strictly dependent on probes photon output. Consequently, it is highly desirable to achieve the best possible signal to noise ratio. This goal can be accomplished using TIRF illumination, where the incident light is internally reflected at the glass-water edge between the coverslip and the sample (Axelrod, 2003). In this way, only the molecules in a very thin layer within the exponentially decaying evanescent field above the coverslip can fluoresce, and most of the background signal is suppressed. Another approach is to use *inclined illumination*. In this modality, the excitation light gets out from the objective at a narrow angle, which results in an inclined beam passing through the sample.

ii. High-quality objectives with high magnification and high numerical aperture.

iii. Automatic focusing system to prevent the sample from going out of focus because of sample drift. Sample drift on the nanometer scale can be caused by a variety of causes, such as vibrations or changes in temperature.

iv. Continuous-wave excitation laser with high power to induce the correct blinking behavior of fluorophores. Typical laser intensities in STORM experiments are around 0.5-5 kW/cm^2.

v. Charge-coupled device (CCD) camera for sensitive detection of fluorescence.

Sample preparation

Choosing a strategy to label the molecule of interest is a crucial issue in STORM imaging that requires following stringent protocols for sample preparation. In order to preserve the structure of interest while keeping the epitopes available for antibody binding, it is recommended to fix the sample. In the case of immunolabeling, the antibodies concentrations must be tested before performing the central experiment to optimize the labeling density and minimize the fluorescent background coming from nonspecific labeling.

Imaging buffers

A rigid control of photoswitching is fundamental. As explained previously, the blinking performance of STORM probes is induced by the forbidden transition of the fluorophore to the triplet state promoted by high excitation laser intensities. From the triplet state, the molecule can be reduced to a dark and stable radical state. Proper photoswitching is closely tied to a delicate balance between the lifetime duration of the “on” state and the “dark” state of the fluorophore. To meet all these requirements, organic dyes need special imaging buffers, containing two principal components: a reducing agent and an oxygen scavenging system.

The *reducing agent* is usually a primary thiol, most commonly β-mercaptoethanol (BME) or mercaptoethylamine (MEA). The blinking mechanism of cyanine derivatives, such as the fluorophore of choice in STORM (Alexa Fluor 647), is at least partially due to the photo-induced formation of a non-fluorescent adduct between the primary thiol and the dye. This adduct can be subsequently broken with UV-violet illumination that breaks the bond (Dempsey et al., 2010).

Since the ground state of molecular oxygen is a triplet, it easily reacts with the fluorophore triplet state, acting as a triplet and radical state quencher. The consequences are a shorter lifetime of the dark state and the production of reactive oxidizing species (ROS) that can cause irreversible photobleaching. Long-lasting triplet and radical state lifetimes are crucial for STORM imaging and the effect of molecular oxygen results in a higher duty cycle. To reduce photobleaching and to lower the duty cycle, an enzymatic *oxygen scavenging system* is included as a fundamental component in imaging buffers. The most common employed scavenging enzyme for STORM buffers is the *glucose oxidase* that performs its function in combination with the enzyme-substrate, glucose, and catalase. The latter removes the hydrogen peroxide produced by the reaction of glucose oxidase. This scavenging system is commonly called *GLOX* (Swoboda et al., 2012).

Furthermore, the GLOX reaction lowers the pH of the imaging solution during the acquisition, so it is essential to buffer the solution to maintain pH stability. Tris buffer ($pK_a \sim 8.0$) is usually utilized.

The buffer described above performs well with cyanine dyes, but when rhodamine derivatives are employed, GLOX is no longer the best choice. In fact, rhodamines blink better in the presence of higher oxygen concentration. Recently, another imaging buffer, named *OxEA*, was introduced (Nahidiazar et al., 2016). The OxEA buffer utilizes OxyFluor^{TM}, an oxygen scavenging system whose substrate is DL-lactate. It has been demonstrated that with this buffer, rhodamine dyes blink better than in GLOX-based imaging buffers, but cyanines still perform better with GLOX.

Analysis Software

After data acquisition, the super-resolution image has to be reconstructed from the stack of collected frames. In each frame, a subset of fluorescent molecules is detected. The software for analysis identifies single-molecules by applying an intensity threshold to find the pixels with higher intensity than the background, and a width threshold to avoid considering nearby fluorophores emitting simultaneously or molecules out of focus as single-molecules.

Determining the precise localization of the identified molecules is the next step. Most of the available software approximates the PSF to a 2D Gaussian model, assuming the fluorophore is an isotropic and point light source. Many localization algorithms have been developed. The choice of algorithm depends on the imaging system, how the user controls fluorophore activation, and many other factors (Small and Stahlheber, 2014).

The most common methods (Abraham et al., 2009) are based on nonlinear least squares algorithms such as Levenberg-Marquardt method (Rust et al., 2006) and maximum likelihood estimation (MLE) (Brede and Lakadamyali, 2012), where a Gaussian PSF and a Poisson noise approximation are used.

Finally, additional data processing methods are applied to improve the image quality. One of the most counterproductive issue is the sample drift during data acquisition. The drift can be corrected by tracking the position of fiduciary fluorescent markers (Betzig et al., 2006) or by splitting the data into subsets of frames and correlating images from each subset (Bates et al., 2007).

1.5 Quantitative methods in SMLMs

In the last years, single-molecule localization microscopies have become a powerful tool to investigate biological structures, such as proteins and their functions inside the cell, not only because of the unprecedented spatial resolution offered by these techniques, but also because they allow counting the imaged molecules of interest.

The biological functions are often strictly dependent on the amount of a specific protein specie inside the cell, and on its heterogeneity in spatial organization. Being able to yield quantitative information about distribution, arrangement and number of proteins, is strongly helpful in the understanding of the etiology of any pathologies or the functioning of any cellular processes inside our organism.

In conventional fluorescence microscopy, the most obvious approach to address quantitative issues is to compare the fluorescence intensity of a protein of interest with a known protein amount labeled with the same fluorescent probe. This method is not reliable because of fluorescence quenching effects (Coffman and Wu, 2012). Another fluorescence-based method to count proteins is *stepwise photobleaching* that relies on the stochastic and irreversible bleaching of fluorescent proteins (FPs), due to long-lasting exposure of the sample to low intensities of excitation light. Fluorescent proteins can be genetically expressed as a construct with the protein of interest, ensuring a 1:1 stoichiometry of labeling. However, since in this approach the likelihood of missed bleaching events increases exponentially with the number of proteins, it is valid only for a low number of molecules (Ulbrich and Isacoff, 2007).

SMLMs reconstruct images from single-molecule localization events of photoswitchable fluorophores (whether they are fluorescent proteins or organic dyes). Consequently, super-resolution localization images already contain information about the number of molecules themselves.

In recent years, several approaches have been developed to extract quantitative information from SMLMs data sets. These quantitative analysis tools strive to obtain not only the number, but also the patterning, the spatial distribution and organization of the molecules of interest at a nanoscale level. By treating localization data as an array of points, it is possible to apply *cluster analysis* or *clustering algorithms* to SMLM outputs (Nicovich et al., 2017). A brief overview of different clustering algorithms and their functioning is provided in the following subparagraph.

Because of the high labeling specificity offered by fluorescent proteins and the relatively low probability (but still a probability!) of overcounting due to the repeated imaging of the same probe, PALM might seem the best choice for quantitative super-resolution imaging and stoichiometry estimation (Durisic et al., 2014) in respect to STORM and the organic dye-labeled antibodies. Nevertheless, FPs' photon output is lower than the photon output of STORM probe, thus affecting the spatial resolution. Finally, the employment of fusion proteins leads to count only the expressed proteins and not the endogenous ones.

For all these reasons, in our work we performed STORM imaging combined to cluster analysis to quantify membrane proteins in neural cells to address two biological current issues.

A different quantitative method is the *quantitative point accumulation in nanoscale topography*, qPAINT (Jungmann et al., 2016), where individual dye-labeled DNA strands transiently bind to target proteins labeled with complementary strands. The dye emits a short fluorescent signal only when both strands are bound, so that it is possible to extrapolate the number of proteins from the apparent blinking of dyes, by controlling the density of implemented dyes.

1.5.1 Cluster analysis of localization data sets

Cluster analysis consists of grouping objects such that objects in the same group, called a *cluster*, are more similar or homogeneous to each other than to those in different clusters. Cluster algorithms had been initially developed in the field of statistical geography. Lately, with the advent of SMLMs, they have been employed to extract topography and quantitative information of sub-diffraction structures from single-molecule localization events. This kind of information can be particularly relevant in biology. For example, in the study of membrane proteins. In fact, a question that often arises when studying membrane proteins is whether they are dispersed, clustered together, or distributed randomly. Clustering (i.e., grouping) of membrane proteins, in fact, might be the consequence of the formation of some underlying membrane structure, or it can be a prerequisite for triggering some functional effect.

In general, spatial clustering methods provide a powerful tool to address the segmentation of dense localization data and “to reveal order within the sea of points” obtained from SMLMs imaging (Nicovich et al., 2017).

Many different clustering algorithms have been adapted or developed for analyzing localization data sets. They differ from each other for the modus operandi.

Briefly, algorithms based on *nearest-neighbor index*, *Ripley's function*, and *pair-correlation function*, are derived from spatial statistics analysis tools (Clark and Evans, 1954; Ripley, 1977; Sengupta et al., 2011). These algorithms are defined only for stationary and spatially homogeneous point processes, where the average density within the point pattern is assumed to be independent of the spatial position. Therefore, they provide only an overall measure of clustering within a region of interest and average cluster size.

Instead, if per-cluster metrics are needed, such as the number, shape, or size of individual clusters, other approaches must be taken into account.

The *density-based analysis* algorithms process localization data by exploiting the difference in density between the clusters and the background, typical of SMLMs images. Generally, in this type of clustering algorithm, the point density surrounding a certain localization event must exceed a certain threshold for that event to be considered as part of a cluster. One of the most popular density-based algorithm is the density-based spatial clustering of applications with noise, DBSCAN (Ester et al., 1996). However, it fails the task when clusters vary largely by density.

The last option is to generate a *mesh representation*, usually a Voronoi diagram or a Delaunay triangulation, based on the spatial distribution of points within a data set (Andronov et al., 2016; Levet et al., 2015). Mesh representations are at the center of the modern computer graphics, so implementations to analyze them are readily available, even if the application of these approaches to SMLMs data sets is relatively recent and unexplored.

1.5.2 Calibration tools for quantifying protein copy number

From what has been said so far, it might be thought that it is possible to determine the exact number of proteins directly by counting the number of localizations detected, and dividing the total number of localizations by the number of localizations measured for an individual fluorophore under similar experimental conditions. Conversely, the quantification of proteins from SML data sets is impaired by the randomness of labeling and the intricate photophysics of the photoswitchable fluorescent probes. In fact, both the antibody labeling efficiency and the number of fluorophores conjugated to the antibodies are highly stochastic.

Also, fluorophores undergo repeated reactivation events leading to the risk of overcounting (Sauer, 2013).

To overcome all these hurdles and quantify the real protein copy number, a number of calibration methods have arisen by different research groups. Some of these methods exploit natural biological calibration samples as a reference standard for counting molecules, such as the *nuclear pore complex* (NPC) that consists of a defined number of proteins (Thevathasan et al., 2019), or *pre- and post-synaptic proteins* (Dani et al., 2010). Another option is offered by artificial calibration samples, including *DNA origami* (Böger et al., 2019; Steinhauer et al., 2009; Zanacchi et al., 2017), *single-molecule assembled patterns generated by cut-and-paste technology* (SMCP) (Cordes et al., 2009; Kufer et al., 2008) and *DNA bricks* (Ke et al., 2012).

Chapter 2

Discovering neurons with single-molecule localization microscopy

“A typical neuron makes about ten thousand connections to neighboring neurons. Given the billions of neurons, this means there are as many connections in a single cubic centimeter of brain tissue as there are stars in the Milky Way galaxy.”

David Eagleman
(Professor at Stanford University, neuroscientist and science communicator)

Understanding the functioning of the brain has always been a major goal of biological and medical sciences. Since the advent of the first optical microscopes, neuroscience has benefited from the progress made in the field of microscopy. Fluorescence microscopy before, and super-resolution fluorescence microscopy then, made neuroscience experiencing a revolution. Nowadays, single-molecule localization microscopies are routinely employed in the study of many biological issues, opening the door for the study of cell sub-structures at the nanometer-scale. The recent literature manifests how the use of SMLMs in the investigation of neuronal cells and synaptic proteins has offered a deeper comprehension of the molecular mechanisms underlying neural networks functioning or neurological disorders. In particular, the knowledge of the spatial distribution and stoichiometry of synaptic proteins is fundamental to reach a complete understanding of the machinery that regulates synaptic transmission. However, a meticulous characterization of the synapses architecture can be achieved only by visualizing them with a quantitative and super-resolved imaging tool, such as single-molecule localization microscopy.

Before the advent of fluorescence nanoscopy that combines minimally invasive imaging with high molecular specificity and a spatial resolution beyond the diffraction barrier imposed by physical laws, the study of intracellular structures and key molecular processes involved in cell life was constrained by the limited resolving power offered by conventional optical microscopes.

Many papers and reviews published in recent years testify the several progress in learning novel information about the structure, organization, stoichiometry, distribution, and dynamics of macromolecules, protein assemblies, and organelles, such as the cytoskeleton, nuclear pore complex, chromatin, synaptic vesicles, focal adhesions, mitochondrial substructures, etc., achieved by employing super-resolution fluorescence microscopy (Magrassi et al., 2019; Sahl et al., 2017; Sigal et al., 2018).

In particular, single-molecule localization microscopies (SMLMs) provided both a substantial improvement of the spatial resolution and the possibility to perform quantitative measurements at a nanometric level, allowing biophysicists to address biological questions that require the observation of sub-diffraction sized cell structures.

Among the different areas of biology, which adopted SMLMs as a tool to answer challenging questions, neuroscience had experienced an undeniable revolution.

2.1 Fundamentals of neuroscience

Neuroscience is the multidisciplinary science that investigates the nervous system to understand the biological basis of its functioning and impairments. Nowadays, neuroscience expands on a wide range of research efforts, from the biological basis of normal and disordered behavior to the molecular biology of nerve cells (Squire et al., 2012).

In all animals, the nervous tissue is the part of the organism responsible for the transmission, elaboration, and reception of internal and external stimuli, signals, and information. Its operation relies on specialized nerve cells called *neurons*. The essential role of neurons is to transfer information encoded in electrical signals to other neurons. These signals between neurons occur by specialized connections called *synapses*, where the information is transmitted by means of an electrical wave of membrane depolarization, called the *action potential* (Alberts et al., 2008).

The neuron is the essential cellular element of the nervous tissue and consists of three main parts (**figure 2.1**). The *soma* (or cell body), which contains the nucleus and the major cytoplasmic organelles, is where the main inner cell functions take place. The *dendrites* are short ramifications that extend from the soma to receive synaptic contacts from other neurons; dendrites become thinner with each branching and may possess multiple short protrusions called *dendritic spines*. The *axon* is a slender projection of the neuron that can extend up to one meter to transmit action potential to target neurons through synapses. It is often branched, but usually maintaining the same diameter.

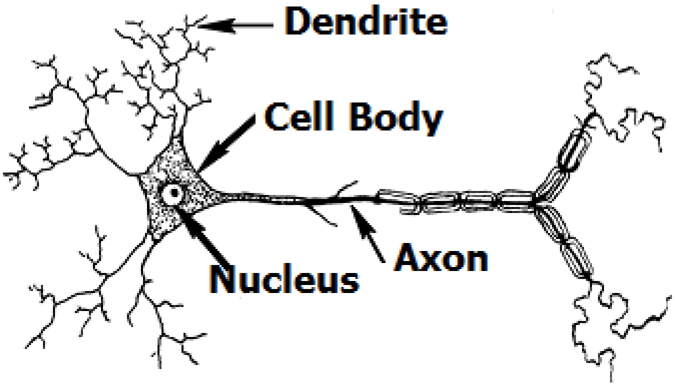
Dendrite
Cell Body
Nucleus
Axon

Figure 2.1 Scheme of a neuron.

A neuron can be morphologically divided into three parts: the dendrites, where the neuron receives the information, the soma, where the nucleus and other organelles are located, and the axon, where the signal is transmitted through synapses

2.1.1 Synapses

The synapse is composed of three components (**figure2.2**). The *presynaptic element* is a specialized part of the axon, the *postsynaptic element* may be a portion of a dendrite or the

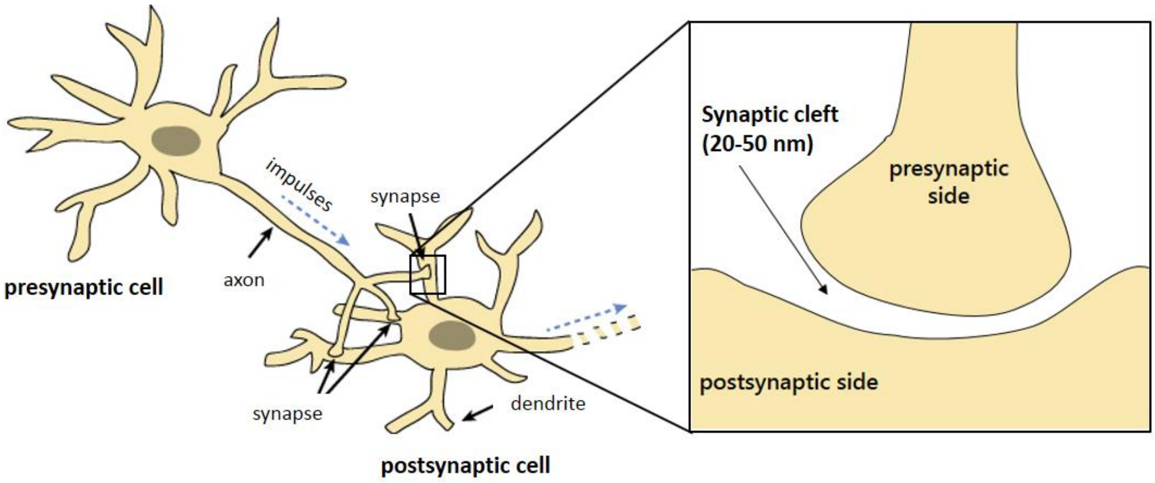
impulses
synapse
presynaptic cell
axon
synapse
dendrite
postsynaptic cell
Synaptic cleft
(20-50 nm)
presynaptic
side
postsynaptic side

Figure 2.2 Neurotransmission and synapses.

A presynaptic neuron transmits a nervous impulse to a postsynaptic neuron through specialized connections called synapses. In the inset, a scheme of a synapse. The presynaptic side on the axon of the presynaptic cell is separated from the postsynaptic terminal on a dendrite of the receiving neuron by a space called synaptic cleft,.

soma, and the nanometric gap between these two elements is named *synaptic cleft*, whose size is typically between 20-40 nm (Zuber et al., 2005).

The presynaptic terminal is rich in *synaptic vesicles*, filled with *neurotransmitters* molecules. Chemically-mediated transmission is the major mode of neuronal communication. When an action potential is conducted through the axon and reaches the presynaptic terminal, depolarization of the membrane occurs. This leads to the fusion of synaptic vesicles with the membrane, and the neurotransmitter can be released into the synaptic cleft (Jin and Garner, 2008). The site of neurotransmitters release is termed *presynaptic active zone* (PAZ). The neurotransmitter molecules bind receptors on the postsynaptic terminal, triggering a conformational change. In the case of *ionotropic receptors*, the neurotransmitter opens or closes the ion channel, creating a postsynaptic current. In the case of *metabotropic receptors*, the neurotransmitter may initiate a secondary messenger pathway.

2.1.2 Synaptic proteins

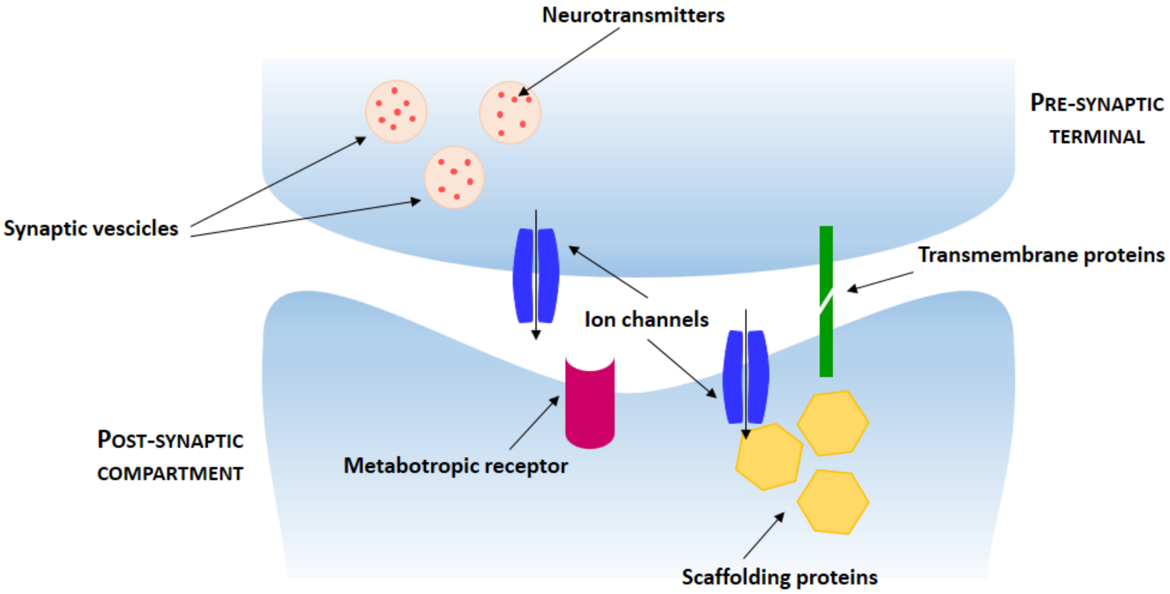
Neurotransmitters
PRE-SYNAPTIC TERMINAL
Synaptic vescicles
Transmembrane proteins
Ion channels
POST-SYNAPTIC COMPARTMENT
Metabotropic receptor
Scaffolding proteins

Figure 2.3 Synaptic proteins.

The synapse is a dense structure of proteins that play a concerted role in the transmission of the nervous signal.

The chemical synapse is a highly dense structure, where the leading players are the membrane-spanning *receptors*, which are located on the postsynaptic terminal. Receptors can be metabotropic or ionotropic, as already mentioned in the previous paragraph.

The ionotropic receptors are *ligand-gated ion channels*, which contain selective binding sites for neurotransmitters. They can undergo fast diffusion from the extra-synaptic regions to the synapse, but they are relatively immobile when bound to *scaffolding proteins*. The latter ones create a platform below the membrane to stabilize the ion channels during synaptic transmission. Synaptic clustering and lateral surface mobility of receptors are primarily modulated by the interaction between receptors and intracellular scaffold proteins (Choquet and Triller, 2013). Therefore, scaffolding proteins are responsible for synaptic transmission, signal transduction, and processing, and they provide a substrate for synaptic plasticity (Alberts et al., 2008).

There are also *voltage-gated ion channels* whose opening/closing is regulated by changes in the membrane voltage. They allow the transport of charges inside and outside the cell membrane. When an incoming action potential arrives at the presynaptic membrane of a chemical synapse, ion channels open, allowing calcium ions to come into the cell and trigger the neurotransmitter release (Kandel et al., 2000).

Finally, the *transmembrane proteins* are present on both synaptic sides and stabilize the synaptic cleft by connecting from one side to the other.

All these proteins are called *synaptic proteins*. The knowledge of their organization and their stoichiometry at a nanoscale level is fundamental to understand the processes that regulate synaptic transmission, and may help to understand the mechanisms that cause neurological disorders. Neuronal transmission is, in fact, a result of a very accurate organization of synaptic proteins.

2.1.3 Excitatory and inhibitory synapses

Depending on the nature of the signal, chemical synapses can be classified into excitatory and inhibitory. If the synaptic potential has an excitatory or inhibitory effect, it depends on the type of receptors present at the postsynaptic cell. When the release of neurotransmitters causes a depolarization of the postsynaptic membrane, the synapse is called *excitatory*. If instead a hyperpolarization occurs, the synapse is considered as *inhibitory* (Kandel et al., 2000).

In the excitatory synapse, when the electrical signal reaches the presynaptic terminal on the axon, excitatory neurotransmitters such as *acetylcholine*, *glutamate*, or *serotonin* are released by the fusion of vesicles containing them with the membrane. The neurotransmitter molecules diffuse in the synaptic cleft and reach the ionotropic receptors on the postsynaptic membrane. The opening of ion channels induces the influx of Na^+ or Ca^{2+} inside the postsynaptic cell, resulting in membrane depolarization that enhances the neuron's ability to generate an action potential in turn. The most common receptors in excitatory synapses are the *N-methyl-D-aspartate receptor* (NMDAR) and *α-amino-3-hydroxy-5-methyl-4-isoxazolepropionic acid receptor* (AMPAR). NMDARs and AMPARs belong to the group of glutamate receptors with crucial roles in memory, learning, and synaptic plasticity (Kandel et al., 2000). The protein *PSD-95* constitutes the core of the scaffold at the postsynaptic density (PSD) of excitatory synapses, and it is fundamental for glutamate receptor stabilization (Renner et al., 2008).

At inhibitory synapses, incoming action potentials produce hyperpolarization of the postsynaptic membrane. Inhibitory neurotransmitters, such as *γ-aminobutyric acid* (GABA) or *glycine*, are released, opening Cl^- or K^+ channels in the postsynaptic side. The opening of K^+ channels makes it harder to drive the cell away from the resting state. Instead, the influx of $Cl^−$ produces an increase of the negative charges in the membrane, which in turn makes it more difficult for the cell to be depolarized and excited (Alberts et al., 2008; Kandel et al., 2000). The most common receptors in inhibitory synapses are *GABA* and *glycine receptors*. Although postsynaptic scaffold proteins, such as *gephyrin*, are present at the inhibitory synapses, the postsynaptic side does not contain a large macromolecular machine of the PSD.

2.1.4 Synaptic plasticity

Neurons are terminally differentiated cells, so they cannot undergo proliferative response to stimuli or damages, as other cells in the animal body. As a result, neurons have evolved other adaptive mechanisms for the maintenance of stable functions. These adaptive mechanisms range from the constant adjustment of gene expression to the modification of the synaptic structure and the strength of synaptic transmission (Squire et al., 2012). In particular, the modulation of synaptic activity is known as *synaptic plasticity*. The molecular mechanisms involved in memory and learning rely upon very similar processes as those involved in morphological and functional plasticity. Plastic changes often result from the alteration of the number of neurotransmitter receptors located on a synapse (Choquet and Triller, 2013).

Long-term potentiation (LTP) is a persistent strengthening of synapses that produce a long-lasting increase in signal transmission between two neurons. It is one of several phenomena underlying synaptic plasticity and it is considered one of the major cellular mechanisms that underlies learning and memory (Kandel et al., 2000).

2.2 Single-molecule localization microscopy as a quantitative imaging tool to study neurons

The synapse is a structure whose visualization is diffraction-limited because of the very narrow cleft dividing the presynaptic and the postsynaptic terminals. Even more, synaptic proteins that regulate the neurotransmission, and whose plasticity is the basis of many regulating processes, are molecules that are impossible to be seen with conventional optical microscopes. Moreover, traditional imaging techniques cannot provide information about protein distribution, density, or assembling. This kind of information are indispensable to a complete understanding of neuronal functions and impairments.

Although electron microscopy was pioneering in synapses imaging (De Robertis and Bennett, 1955; Palay and Palade, 1955), the aforementioned drawbacks of this technique combined with the low contrast at the molecular level make the imaging of synaptic proteins and their complexes highly challenging.

Super-resolution microscopies have provided new insights into the study of nerve cells. Among them, SMLMs have proven to be the most suitable imaging techniques in the investigation of synaptic proteins, allowing researchers to achieve a quantitative characterization of their organization at the nanoscale.

Here we summarize the most relevant findings obtained in the field of neuroscience by the employment of SMLM in recent years.

2.2.1 Structural investigation of neurons and synapses

Since the cytoskeleton is a well-characterized structure having dimensions similar to the imaging resolution achievable with SMLMs, it was widely used as a convenient cellular structure to test the resolving power of single-molecule-based and the localization precision. However, SML imaging leads to a surprising discovery concerning the cytoskeleton of neurons. By means of 3D-STORM, it was determined a *membrane-associated periodic skeleton* (MPS) in axons (Xu et al., 2013). MPS consists of short actin filaments capped by adducin ring-like structures that wrap around the axon circumference. These rings are connected through spectrin tetramers along the major axis. This periodic lattice has eluded visualization by electron microscopy.

STORM imaging has revealed the protein mapping of pre- and postsynaptic terminals, providing a clearer picture of the spatial organization of molecular scaffolds and machinery (Dani et al., 2010).

Moreover, PALM and PAINT in live neurons allowed to identify an activity-dependent clustered organization of postsynaptic receptors and scaffolding proteins in *subsynaptic domains* (SSDs) (MacGillavry et al., 2013; Nair et al., 2013; Pennacchietti et al., 2017). In addition, localization microscopy has contributed to the detection of a clustered organization also across the synaptic cleft, where presynaptic vesicles fusion sites and postsynaptic receptors are spatially aligned, forming the so-called *nanocolumns* (Tang et al., 2016). This molecular organization may facilitate synapses formation and communication by providing a mechanism for the coordination of synaptic vesicles release and receptors response.

2.2.2 Quantitative imaging of synaptic proteins

Along with structural studies of neural cells and synaptic protein assemblies, a remarkable number of quantitative investigations were performed with SML techniques.

In the already mentioned work from Zhuang’s group, they did not only reveal synaptic molecular organization but also quantified two proteins, GluR1, from AMPARs, and GluN2B, from NMDA receptors, in correlation to the quantification of Homer, a very well-defined postsynaptic protein (Dani et al., 2010).

Other labs focused on the quantification of the protein stoichiometry. Regarding the postsynaptic site, it was shown that the AMPARs are organized in nanodomains of around 70 nm in the synapse (Nair et al., 2013). They also showed that these AMPARs are stabilized in these nanodomains and they diffuse in stochastic dynamics among them. Finally, they reported an estimation of the number of receptors in each nanodomain using the dSTORM images. By considering the distribution and median of the fluorescence intensity emitted by an isolated single AMPAR, they made a calibration of fluorescence to extrapolate an estimation of the number of molecules from the intensity distribution of the nanodomains.

Although it is not yet well-characterized as the excitatory synapse, also the inhibitory synapse has been the subject of quantitative studies. A close correspondence between the spatial organization of gephyrin scaffolds and glycine receptors (GlyRs) at spinal cord synapses has been found (Specht et al., 2013). Moreover, several recent studies have assessed the dynamic changes of receptor clustering as a result of the stimulation of the synaptic plasticity. It was reported that during long-term potentiation of inhibitory neurotransmission (iLTP), gephyrin is gathered at the postsynaptic terminal, thus driving an increase in the number of synaptic $GABA_A$ receptors. Therefore, the nanoscale organization of inhibitory synaptic proteins is a crucial determinant for inhibitory synaptic plasticity (Pennacchietti et al., 2017).

Chapter 3

Quantitative investigation of $GABA_A$ receptor organization at the inhibitory synapse

"I always think that inhibition is a sculpturing process. The inhibition, as it were,
chisels away at the ... mass of excitatory action and gives a more specific form
to the neuronal performance at every stage of synaptic relay."

Sir John Carew Eccles
(Nobel Prize for Medicine in 1963)

Inhibitory transmission is fundamental in tuning neuronal excitability and network functions, and it also regulates higher cognitive functions in the brain and underlies some neurological disorders when impaired. Inhibition can undergo strength alterations due to synaptic plasticity, related to a modification in the number of inhibitory ionotropic receptors clustered at the synapse.

Until the advent of super-resolution microscopy, molecular mechanisms underlying plasticity of inhibition remained unclear, since the synapse size is below the diffraction limit. Recent studies employing super-resolution microscopy techniques have shown that receptors and scaffold proteins at the inhibitory synapses are organized into subsynaptic domains (SSDs), suggesting a fundamental role of proteins assembling in neuronal transmission.

In this chapter, we show how the employment of single-molecule localization imaging to study the inhibitory synapse architecture, allows to obtain quantitative and structural information about $GABA_A$ *receptors rearrangement under plasticity at a nanoscale level.*

3.1 The inhibitory neurotransmission

A synapse is classified as inhibitory when an action potential in the presynaptic neuron decreases the probability of an action potential occurring to the postsynaptic neuron, since the incoming action potential produces a hyperpolarization of the postsynaptic membrane. The *inhibitory postsynaptic potential* (IPSP) takes place when an inhibitory neurotransmitter, such as *γ-aminobutyric acid* (GABA) or *glycine*, is released in the synaptic cleft determining the opening of Cl^- channels on the postsynaptic membrane. The entry of negative charges in the membrane makes it harder for the neuron to be depolarized and excited (Alberts et al., 2008; Kandel et al., 2000).

Since inhibitory neurotransmission plays a central role in the brain being involved in many pathways, inhibitory synaptic strength oscillations are a crucial mechanism in the regulation of network activity. Inhibitory plasticity is expressed both at the presynaptic level and the postsynaptic level, but while there has been noteworthy progress in the characterization of the presynaptic mechanisms of inhibitory long-term plasticity, the postynaptically-expressed plasticity of inhibition only start to be explored (Petrini and Barberis, 2014).

3.1.1 The GABAergic synapse

Inhibition in the central nervous system is primarily mediated by γ-aminobutyric acid (GABA) acting through GABA$_A$ receptors (GABA$_A$Rs). GABA$_A$Rs are composed of five subunits.

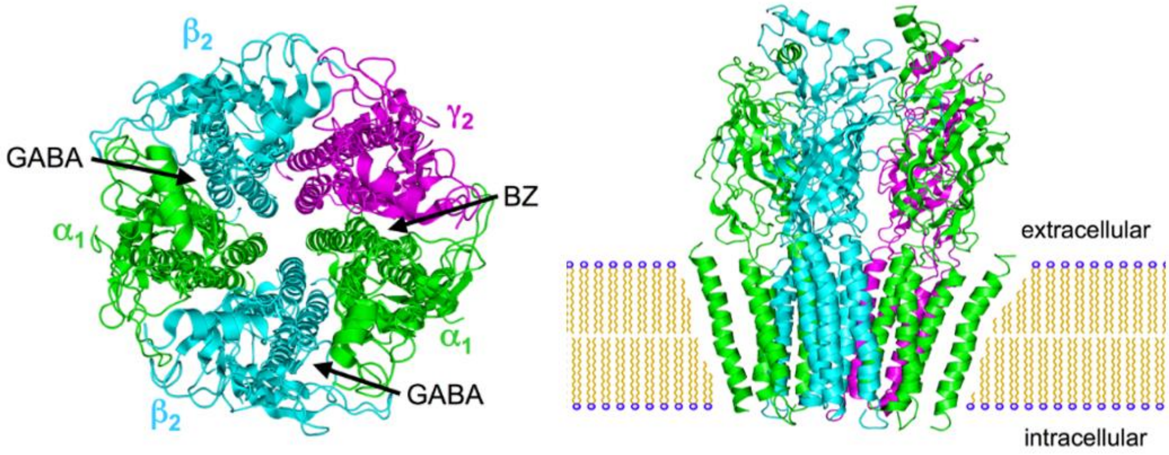

Figure 3.1 GABA$_A$ receptor.

Structural cartoons representation of GABA$_A$ receptor (PDB: D6W0). On the left the top view, and on the right the side view. There are two binding sites for GABA at the interfaces between the α and β subunits. Instead, benzodiazepines (BZ) bind the channel at the interface between the α and γ subunits, enhancing the influx of chloride ions.

These subunits can be encoded by 19 different genes, which have been grouped into eight subclasses based on sequence homology: α_{1-6}, β_{1-3}, γ_{1-3}, δ, ε, θ, π, and ρ_{1-3}. Thus, $GABA_A$ receptor consists of a heteropentameric GABA-gated chloride channel, usually formed by two α subunits, two β subunits, and one γ subunit, that can be replaced by δ, ε, θ, π or ρ subunits (Barnard et al., 1998; Luscher et al., 2011). Two molecules of γ-aminobutyric acid bind the channel at the interface between α and β subunits and trigger the opening of the channel, allowing the passage of chloride ions into the cell (**figure 3.1**).

$GABA_AR$ subunits composition determines different subtypes of the receptor, which show different pharmacological and physiological properties, diverse expression levels during brain development and in the adult brain, and different locations along the neuron membrane. Receptors with α_{1-3}, β, and γ subunits are more concentrated at synapses than in the extrasynaptic compartments (Kasugai et al., 2010).

$GABA_ARs$ are expressed ubiquitously in neurons, but it is the number of receptors at the postsynaptic membrane that directly affects the strength of GABAergic synaptic transmission. Thus, modifications in the receptor expression and trafficking are both essential mechanisms for the modulation of many aspects of brain function or prevention of different pathologies (Luscher et al., 2011).

3.1.2 Synaptic plasticity and long-term potentiation of inhibition

Under basal conditions, neurotransmitter receptors intracellular trafficking and lateral mobility guarantee receptor renewal, but it also underlies many forms of synaptic plasticity by regulating surface receptors disposability at the postsynaptic density (PSD) (Choquet and Triller, 2013).

In particular, the postsynaptic expression of inhibition relies on the active reorganization of molecular components of the GABAergic synapse, including $GABA_A$ receptors, scaffold proteins, and structural molecules (Petrini and Barberis, 2014).

The influence of receptors lateral diffusion on synaptic plasticity has been widely investigated at the excitatory synapses, where long-term potentiation (LTP) induction lead to the immobilization of synaptic α-amino-3-hydroxy-5-methyl-4-isoxazoleproprionic acid receptors (AMPARs) (Heine et al., 2008; Petrini et al., 2009). Instead, despite the evidence of enhanced $GABA_ARs$ lateral diffusion involvement in inhibitory long-term potentiation (iLTP) expression, the mechanism regulating receptors accumulation and stabilization at the synapse during potentiation of inhibition remains unclear.

It has been reported that in hippocampal cultured neurons, moderate activation of N-methyl-D-aspartate receptor (NMDAR) triggers the translocation of activated Ca^{2+}/calmodulin-dependent kinase II (CaMKII) to inhibitory synapses and CaMKII-dependent exocytosis of GABA$_A$Rs, (Marsden et al., 2007). NMDAR activation can be used to chemically induce iLTP. During chemical induced iLTP the surface mobility of GABA$_A$Rs is reduced, potentiating GABAergic synaptic currents. In fact, the NMDARs activation enhances β$_3$-subunit phosphorylation at serine 383 by Ca^{2+}/calmodulin-dependent kinase, immobilizing and confining the receptors at the inhibitory synapse (Petrini et al., 2014).

3.1.3 Gephyrin stabilizes GABA$_A$Rs at the postsynapse

Scaffold proteins are critical determinants of the internal architecture of synapses, as they provide binding sites for the anchorage of neurotransmitter receptors at the postsynaptic membrane.

The PSD of GABAergic synapses is characterized by high-density assemblies of *gephyrin* that is the principal scaffold protein at the inhibitory synapse. It forms an intracellular structure below the postsynaptic membrane. The interaction between gephyrin and α$_{1-3}$ and β$_{2-3}$ subunits of GABA$_A$R has been demonstrated, as well as its involvement in the synaptic accumulation of GABA$_A$Rs (Kneussel et al., 1999). Indeed, gephyrin plays a specific role in reducing lateral diffusion of GABA$_A$Rs promoting their clustering at the synapse (Jacob et al., 2005).

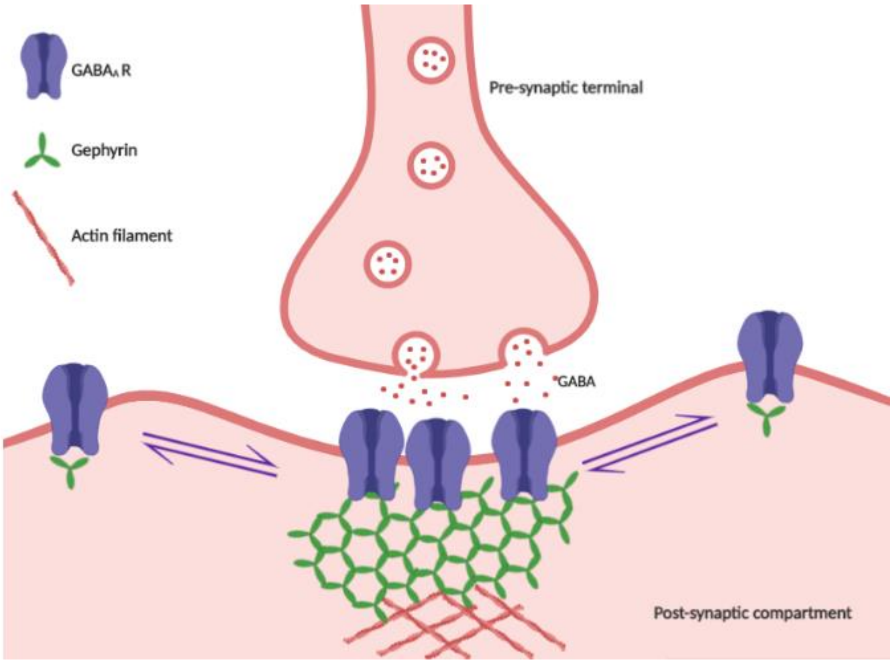

Figure 3.2 Mechanism of recruitment of extra-synaptic gephyrin to synaptic compartments.

Single-particle tracking of individual $GABA_ARs$ labelled with Quantum Dots (QDs) demonstrated that chemically induced long-term potentiation promotes gephyrin recruitment at the synapse from extrasynaptic compartments with the consequent clustering and immobilization of receptors (**figure 3.2**), thus potentiating GABAergic synaptic currents (Petrini et al., 2014).

3.2 Unveiling the nanoscale architecture of the inhibitory postsynaptic density

The impairment of inhibition functioning can alter the excitatory/inhibitory balance of the neural network, concurring to several neurological disorders (Yizhar et al., 2011). Therefore, it is crucial to define the mechanisms by which $GABA_ARs$ are stabilized at synaptic sites, and how their clustering is modulated under plasticity condition, in order to understand neuronal inhibition and its disruption in pathologies (Luscher et al., 2011).

Super-resolution optical microscopy circumvented the diffraction limit of conventional optical microscopes, offering to the neuroscientists a powerful tool to reveal the subsynaptic organization of proteins with unprecedented resolution. It has been proved that scaffold proteins and neurotransmitters receptors organize themselves in dense assemblies called *subsynaptic domains* (SSDs) of variable morphology, whose formation appears to be related to the reshaping of synapses during plasticity (MacGillavry et al., 2013; Nair et al., 2013; Specht et al., 2013).

3.2.1 The role of gephyrin subsynaptic domains in the inhibitory plasticity

The application of super-resolution optical techniques to the investigation of SSDs architecture has led to significant findings regarding the role played by the scaffold protein gephyrin in the expression of inhibitory plasticity. Recently, the employment of photo-activated localization microscopy (PALM) combined with cluster analysis has enlightened the relation between gephyrin clustering into nanoscale subsynaptic domains at the postsynaptic site and the modulation of inhibitory neurotransmission. In detail, it has been reported that under plasticity condition chemically induced by long-term potentiation, gephyrin is recruited at the synapse from the extrasynaptic areas, increasing number of molecules per cluster, cluster area, and density of gephyrin copies and stabilizing $GABA_ARs$

in the postsynaptic membrane. Moreover, synaptic gephyrin potentiation is accompanied by its fragmentation in multi-spot high-density nanodomains, while under basal condition gephyrin is organized in single-spots (**figure 3.3**). This nanoscale reorganization of gephyrin is a determinant of the inhibitory synaptic plasticity (Pennacchietti et al., 2017).

In another recent study (Crosby et al., 2019), three-dimensional structured-illumination microscopy (SIM) and stimulated emission depletion microscopy (STED) have been exploited to get information about the architectural interdependence between $GABA_AR$ and gephyrin. Super-resolution imaging confirmed that inhibitory pre- and postsynaptic sites are composed of nanoscale $GABA_AR$ and gephyrin SSDs and provided information about the size of compartments (i.e., the regions of synapse occupied by receptors or gephyrin SSDs), SSD number, SSD area, and SSD diameter. What resulted is a significant similarity between gephyrin and $GABA_AR$ compartments volumes, suggesting that gephyrin and $GABA_AR$ SSDs closely associate and are dependent on each other.

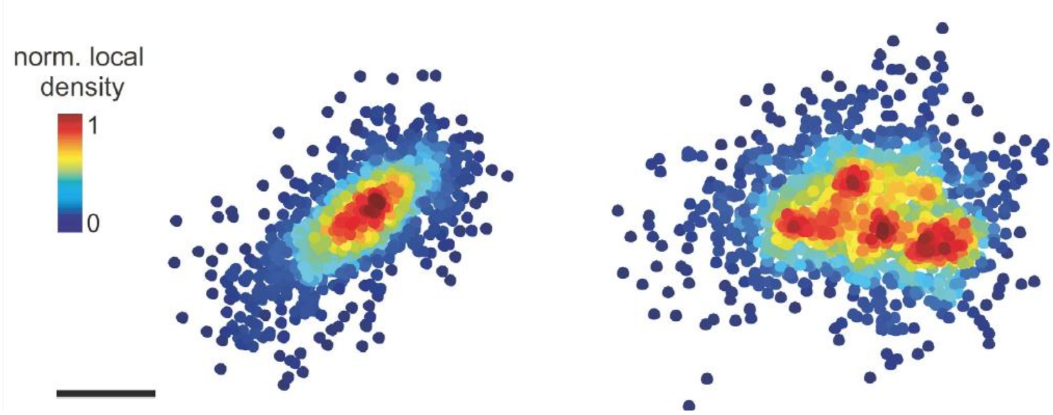

Figure 3.3 PALM images of postsynaptic gephyrin topography.

Single-molecule localization images (PALM) experiments to study the synaptic distribution of gephyrin in culture hippocampal neurons. Points represent detections of single fluorophores, showing synaptic gephyrin clusters. Left panel: density map of a gephyrin subsynaptic domain (SSD) exhibiting a Gaussian distribution (mono-spot). Right panel: gephyrin reorganization during synaptic plasticity revealing a non-uniform local density map, suggesting a fragmentation of gephyrin in multiple nanodomains at the synapse (multi-spot) (Pennacchietti et al., 2017)

Furthermore, gephyrin compartments with larger numbers of SSDs are more likely to be associated with larger numbers of $GABA_AR$ SSDs, confirming that gephyrin recruitment affects $GABA_ARs$ clustering at the synapse. They also performed a long-term homeostatic scaling treatment to induce a kind of synaptic plasticity, revealing that inhibitory synapses recruit additional SSDs during their activity-dependent growth. Still, SSDs do not increase their volumes, indicating that new SSDs form at the synapse as it increases in size, rather than expand already existing SSDs.

3.2.2 Nanoscale rearrangement of $GABA_A$Rs in GABAergic plasticity

Previous paragraphs have stressed the importance of deepening the spatial organization of synaptic proteins at the nanoscale to understand the molecular mechanisms underlying the inhibitory neurotransmission. As just mentioned, there are precedent works investigating the distribution of inhibitory synaptic proteins with super-resolution, with special attention for the reshaping of gephyrin SSDs during inhibitory synaptic plasticity (Crosby et al., 2019; Pennacchietti et al., 2017). However, to date, there are no works in literature focused on the study of the $GABA_A$ receptors reorganization under plasticity conditions at a molecular level.

In this thesis, we aimed to report structural and quantitative differences in spatial distribution between $GABA_A$Rs at the inhibitory synapse in basal conditions and $GABA_A$Rs at the inhibitory synapse during synaptic plasticity that alters the strength and efficacy of synaptic inhibition.

In order to accomplish our goal we exploited stochastic optical reconstruction microscopy (STORM) combined with distance-based cluster analysis. STORM provides imaging capability with spatial resolution of the order of 10 nm (Rust et al., 2006) but above all, allows extracting quantitative information from localization data sets in term of number of SSDs and number of localization per SSD (Nicovich et al., 2017), permitting a comparison between the two different conditions.

We studied two subtypes of $GABA_A$Rs in cultured mouse hippocampal neurons, α_1-$GABA_A$R and α_2-$GABA_A$R, labeling the α_1 subunit in the first case and the α_2 subunit in the latter case, using an activator-reporter pair custom-made. Then, we imaged surface $GABA_A$Rs on dendrites along with a presynaptic marker, the *vesicular GABA transporter* (vGAT) to label inhibitory axon terminals and verify the functionality of synapses. STORM imaging was performed in control samples and in samples stimulated by chemically induced long-term potentiation (iLTP), following the protocol described previously (Petrini et al., 2014). The images were then analyzed with a previously developed cluster analysis method (Ricci et al., 2015).

3.3 Materials and methods

All animal procedures were conducted in accordance with the guidelines established by the European Communities Council (Directive 2010/63/EU of 22 September 2010), by the Italian Ministry of Health's directives (D.lgs 26/2014), and by the Istituto Italiano di Tecnologia.

3.3.1 Primary neuronal cultures

Cultures of hippocampal neurons were prepared from P1-P3 C57BL/6J mice of either sex using a previously published protocol (de Luca et al., 2017). Neurons were plated at a density of 70 × 10^3 cells per ml on polylisine pre-coated coverslips and kept in serum-free Neurobasal-A medium (Invitrogen, Italy) supplemented with Glutamax (Invitrogen, Italy) 1%, B-27 (Invitrogen, Italy) 2%, at 37°C in 5% CO_2 for 14 DIV. During this period, half of the medium was exchanged weekly.

3.3.2 iLTP induction and drug treatments

iLTP was chemically induced by NMDA receptor (NMDAR) activation, as previously described (Marsden et al., 2007; Pennacchietti et al., 2017; Petrini et al., 2014). Briefly, neurons were incubated in a recording solution containing NaCl 145mM, KCl 2mM, $CaCl_2$ 2mM, $MgCl_2$ 2mM, glucose 10mM, and HEPES 10mM, pH 7.4, supplemented with NMDA 20μM (Sigma-Aldrich) and CNQX 10μM (Tocris Bioscience) for 2 min and then allowed 18 min recovery in the recording solution. In control samples, NMDA and CNQX were omitted.

3.3.3 Immunostaining protocol

As previously mentioned, two different subunits of GABA$_A$R were labeled and imaged, both under basal conditions and during iLTP. The immunostaining protocol was the same for the two subunits, except for the primary antibodies directed against the subunit α_1 and the subunit α_2: the rabbit anti-GABA$_A$ receptor α_1 subunit (#AGA-001, Alomone), directed against an extracellular epitope, was used at 1:100 diluition; the rabbit anti-GABA$_A$ receptor α_2 subunit (#224103, Synaptic System) directed against an extracellular epitope, was used at 1:500 diluition. After incubation with the recording solution (supplemented with NMDA and CNQX for stimulated samples and without for controls), neurons were fixed with 4%

paraformaldehyde (PFA) in phosphate-buffered saline (PBS) for 10 min at room temperature (RT). After that, neurons were incubated with a blocking buffer solution containing 1% (w/v) bovine serum albumin (BSA) (Sigma-Aldrich) in PBS, for 30 min at RT to prevent non-specific binding. Immunolabeling of α_1-GABA$_A$R or α_2-GABA$_A$R was performed in non-permeabilized neurons incubated with the aforementioned primary antibodies at RT for 1h, followed by 45 min incubation with a custom built anti-rabbit secondary antibody conjugated with the dye pair Alexa Fluor 405/Alexa Fluor 647 (conjugation protocol in the following paragraph) at RT.

Subsequently, neurons were permeabilized with 0.2% Triton X-100 (Sigma-Aldrich) for 10 min and incubated with the mouse anti-vGAT primary antibody (1:400) directed against the luminal domain of vGAT (#131011, Synaptic Systems) for 1h. Then, samples were incubated with 1:500 solution of anti-mouse secondary antibody conjugated with Alexa Fluor 488 (ThermoFisher Scientific).

At the end of the immunostaining, samples were fixed again in PFA 2% for 5 min and stored in PBS at 4°C.

3.3.4 Activator-reporter dye pairs preparation protocol

For STORM imaging, the photo-switchable secondary antibody consisting of a dye activator/reporter was custom prepared following the STORM-protocol sample preparation (Nikon) (Bates et al., 2007).

Briefly, secondary antibody used was a donkey anti-rabbit from Jackson ImmunoResearch Europe. The dyes were purchased as NHS ester derivatives: Alexa Fluor 405 carboxylic acid succinimidyl ester (Invitrogen), and Alexa Fluor 647 carboxylic acid succinimidyl ester (Invitrogen). Antibody labeling reaction was performed by incubating for 40 min at RT a mixture containing the secondary antibody, NaHCO3, and the appropriate pair of activator/reporter dyes diluted in dimethyl sulfoxide, anhydrous (DMSO) (Sigma-Aldrich).

Purification of labeled antibody was performed using NAP5 Columns (GE HealthCare). The dye to antibody ratio was quantified using NanoDrop™ in order to have a labeling ratio within the range:

Activator Dye : Antibody : Reporter Dye = 2.0 – 3.0 : 1 . 0.6 – 1

3.3.5 STORM imaging and data reconstruction

STORM microscope

A commercial N-STORM TIRF microscope (Nikon Instruments), equipped with an oil immersion objective (CFI Apo TIRF 100x, NA 1.49), was used to acquire 20,000 frames at a 33 Hz frame rate using highly inclined illumination. The duration of the acquisition was the same in all experiments.

An excitation intensity of ~ 1.0 kW/cm^2 for the 647 nm read-out (300 mW laser; MPB Communications) and an activation intensity of ~ 30 W/cm^2 (100 mW laser; Coherent CUBE) were used.

A repeating cycle of 1 activation frame followed by 3 read-out frames was used, and imaging was performed with an EMCCD camera (Andor iXon DU-897, Andor Technologies). The Nikon Perfect Focus System was applied during the entire recording process. Fluorescence-emitted signal was spectrally selected by the four colors dichroic mirrors (ZET405/488/561/647; Chroma) and filtered by a multiband pass filter (ZT405/488/561/647; Chroma).

Imaging buffer

All samples were imaged in the previously described GLOX imaging buffer (pages 30, 31), containing a glucose oxidase solution as oxygen scavenging system (40 mg/mL^{-1} catalase (Sigma-Aldrich), 0.5 mg/mL^{-1} glucose oxidase, 10% glucose in PBS) and MEA 10 mM (cysteamine MEA (#30070-50G; Sigma-Aldrich) in 360 mM Tris-HCl) (Bates et al., 2007).

Imaging protocol

Imaging was performed in two steps for each image:

- *First step*: acquisition of 500 frames of 488 channel with exposure time of 70 ms only to localize the centroid positions of presynaptic vGAT diffracted spots. Alexa Fluor 488 does not blink with the glox buffer. The aim of this step is to label the presynaptic site of active synapses as a landmark.
- *Second step*: acquisition of 20,000 frames of 647 channel with an exposure time of 30 ms. 647 nm laser was used for exciting the reporter dye (Alexa 647) and switching it to the dark state. 405 nm laser light was used for reactivating the Alexa Fluor 647 into a fluorescent state via the activator dye (Alexa Fluor 405).

An imaging cycle was used in which one frame belonging to the activating light pulse (405 nm) was alternated with three frames belonging to the imaging light pulse (647 nm).

Analysis of raw STORM data

The images reconstruction was performed using a custom software (Insight3, kindly provided by Dr. Bo Huang of University of California) by Gaussian fitting of the single-molecule images in each frame to determine the x-y coordinates. The molecules were identified by setting always the same threshold of counts/pixel (800 for α_1 experiments and 1200 for α_2 experiments). The final images were obtained by plotting each identified molecule as a Gaussian spot and corrected for drift by cross correlating images obtained from subsets of frames as described in literature (Huang et al., 2008).

3.3.6 Cluster analysis

Cluster analysis of localized STORM data was performed with a MATLAB (The MathWorks, Natick, MA) custom-written code implementing a distance-based clustering algorithm (Ricci et al., 2015). This code is used to identify spatial clusters of localizations and is part of the density-based clustering algorithms family. It is suitable to analyze optimally both high-density and low-density protein distributions because it allows acting on a scale factor that determines the segmentation degree of examined clusters without affecting the clustering ability of the algorithm.

The localization lists were first binned to construct discrete localization images with a pixel size of 20 nm. These were filtered with a square kernel (5×5 pixel) to obtain a density map and transformed into binary images by applying a constant threshold, such that pixels have a value of 1 where the density is larger than the threshold value and a value of 0 elsewhere. These binary images were used only to locate regions of the sample containing localizations. Further analysis were performed on raw localization data. From the binary images, only localizations lying on adjacent (six-connected neighbors) nonzero pixels of the binary image were considered. Localization coordinates within each connected component were grouped employing the distance-based clustering algorithm. Initialization values for the number of clusters and the relative centroid coordinates were obtained from local maxima of the density map within the connected region, and localizations were associated with clusters based on their proximity to cluster centroids. New cluster centroid coordinates were iteratively calculated as the average of localization coordinates belonging to the same cluster. The procedure was iterated until convergence of the sum of the squared distances between localizations and the associated cluster (Ricci et al., 2015).

The algorithm relies on a limited number of parameters and allows setting a factor, whose value determines the degree of segmentation of clusters, and a threshold of minimum number of molecules, in order to avoid noise. Before analyzing localization data from SML images, we optimized clustering factors and parameters to obtain the best performance of clustering on our synaptic protein distributions. Analysis of each image were performed with the same selected parameters.

The algorithm provided cluster centroid positions and the number of localizations per cluster.

3.3.7 Statistical analysis

All statistical tests were performed in OriginPro2016. Data were tested with unpaired two-tailed Student's *t* test. P-values were considered significant if < 0.05. Bar graphs are displayed as mean ± standard error of mean (SEM), unless otherwise noted.

3.4 Results

3.4.1 Quantitative super-resolution imaging of GABA$_A$Rs

To determine the organization of GABA$_A$Rs with nanometric accuracy we used 2D STORM to image surface GABA$_A$Rs on hippocampal neuronal dendrites, along with a presynaptic marker, the vesicular GABA transporter (vGAT), to mark inhibitory axon terminals.

In order to do this, before acquiring single-molecule localizations of the receptors labeled with the photoswitchable dye pair, we collected just few frames (~ 500) of fluorescence emission of vGAT labeled with Alexa Fluor 488, to localize the centroid position of the pre-synapse as an indicator of its position (**figure 3.4**).

To get a statistically valid population of synapses to be investigated quantitatively, we collected tens of images of several samples of cultured hippocampal neurons at DIV14, prepared in different days. We acquired both stimulated samples (i.e., iLTP induced neurons) and control samples (i.e., neurons prepared with the same protocol but in basal conditions) (**figure 3.5**).

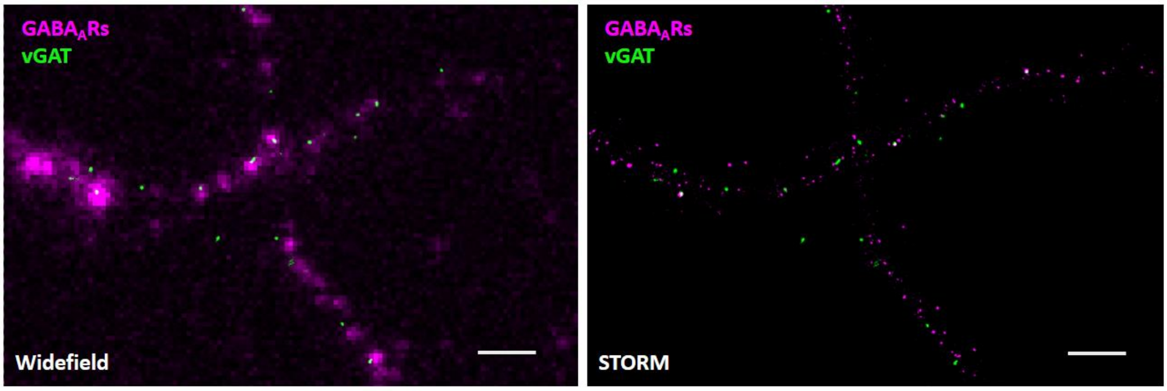
GABA$_A$Rs
vGAT
Widefield
GABA$_A$Rs
vGAT
STORM

Figure 3.4 STORM imaging of GABA$_A$Rs, and localization of the centroid positions of presynaptic vGAT.

Left, first step of imaging protocol; the centroid positions of vGAT (green), acquired with few frames of Alexa Fluor 488 emission and fitted with the STORM image reconstruction software (Gaussian fit); GABA$_A$R is displayed as a wide-field image (magenta). On the right, STORM imaging of GABA$_A$Rs (magenta). Scale bars, 2μm.

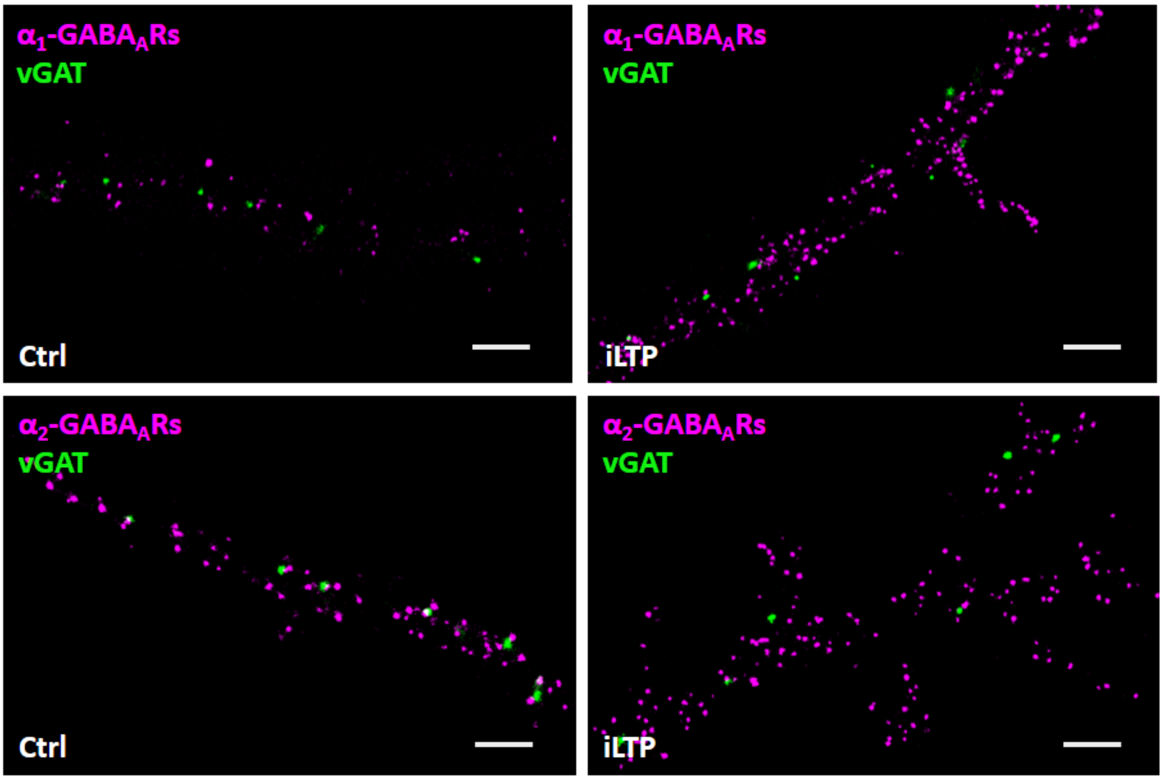
α$_1$-GABA$_A$Rs
vGAT
Ctrl
α$_1$-GABA$_A$Rs
vGAT
iLTP
α$_2$-GABA$_A$Rs
vGAT
Ctrl
α$_2$-GABA$_A$Rs
vGAT
iLTP

Figure 3.5 Examples of single-molecule localization images of the acquired samples.

Top, Left, STORM image of α1-GABA$_A$Rs in control samples; Right, STORM image of α1-GABA$_A$Rs in iLTP samples. Bottom, Left, STORM image of α$_2$-GABA$_A$Rs in control samples; Right, STORM image of α$_2$-GABA$_A$Rs in iLTP samples. Scale bars, 1μm.

In order to quantify molecular density, SSDs number and size of α_1-GABA$_A$ and α_2-GABA$_A$, we processed single-molecule localization images with the MATLAB code implementing a distance-based clustering algorithm (Ricci et al., 2015), previously optimized to study synaptic protein distributions. In a first step, only receptor localizations located at a distance no longer than 500 nm from the presynaptic vGAT are selected. This range of distance from the presynaptic site mimics the generic size of a synapse. Afterwards, the algorithm clusters GABA$_A$Rs localization based on their distance from the centroids of each local maxima of receptor density. The final output of clustering consists in a color-code map, where each color represents a SSD of GABA$_A$R belonging to a synapse (**figure 3.6**).

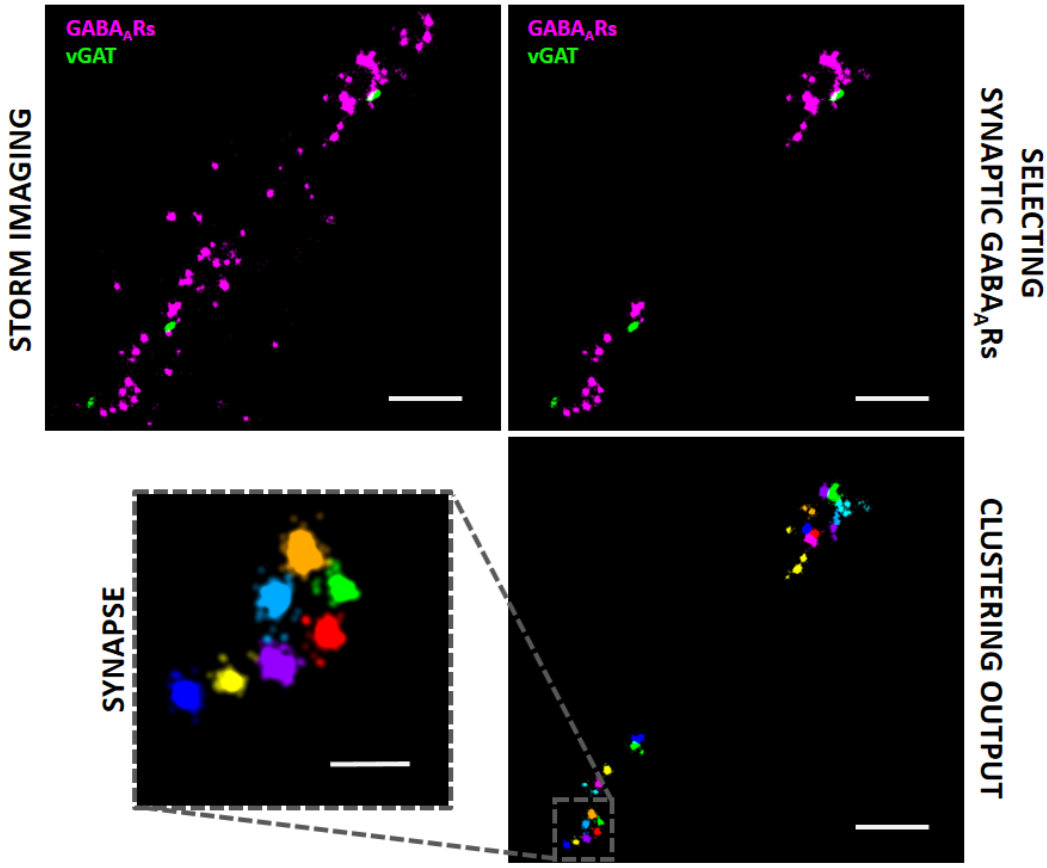

Figure 3.6 Single-molecule imaging and cluster analysis of GABA$_A$ receptor at the inhibitory synapse.

Top, Left, Representative input of the cluster analysis; Right, selection of GABA$_A$R localizations in a 500 nm distance range around the vGAT centroids. Bottom, Right, Representative output of the clustering algorithm, that is a color-code map of GABA$_A$R SSDs. Scale bars, 1μm.

Bottom, Left, Magnification of the inset in the right picture that shows receptor SSDs at the synapse. Scale bar, 250 nm.

3.4.2 Enhancement of synaptic GABA$_A$Rs under plasticity conditions

By processing STORM images with the distance-based clustering algorithm, we quantified GABA$_A$Rs at the inhibitory synapse in control neurons, under basal conditions, and in stimulated neurons, during chemically induced long-term potentiation of inhibition. This form of inhibitory synaptic plasticity has been reported to enhance GABAergic synaptic currents by promoting the accumulation of GABA$_A$Rs at the postsynaptic site (Petrini and Barberis, 2014).

Therefore, we aimed to compare the number of GABA$_A$R localizations in these two different conditions. The number of localizations is proportional to the number of receptors per synapse.

GABA$_A$R SSDs in close proximity to vGAT puncta were considered as synaptic. Since we knew the number of localization of receptor per SSD from cluster analysis, we calculated the number of localizations per synapse.

We found that under plasticity conditions the number of localizations of GABA$_A$ receptor per synapse increased significantly, for both α_1-GABA$_A$R (from 270.3 ±16.1 in the basal condition to 343.7 ± 20.6 during iLTP, n = 336 and 365, respectively, $p < 0.01$, Student's *t* test) and α_2-GABA$_A$R (from 294.1 ±11.4 in the basal condition to 368.0 ± 16.4 during iLTP, n = 585 and 465, respectively, $p < 0.01$, Student's *t* test). Respectively, we observe a 27% increase of α_1-GABA$_A$R localizations and a 25% increase of α_2-GABA$_A$R localizations

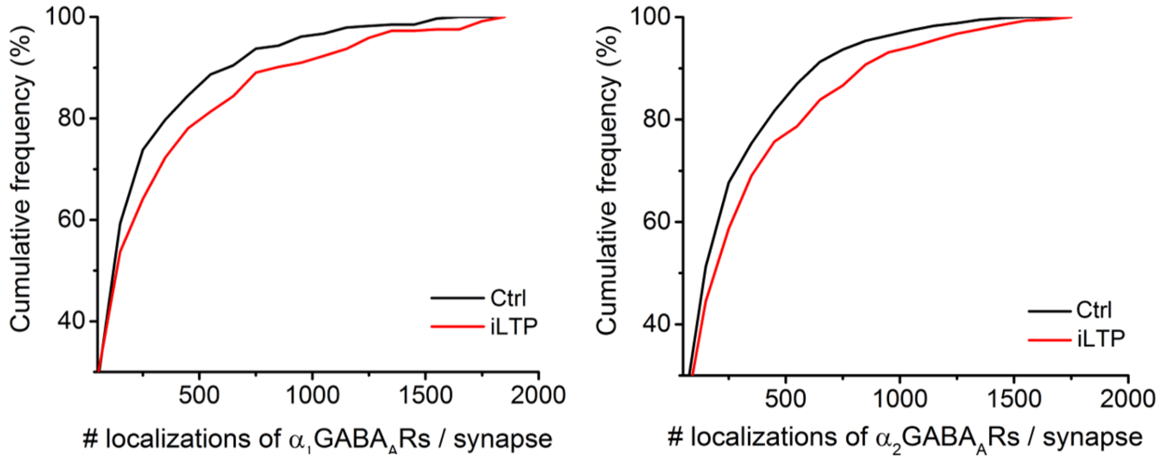

Figure 3.7 Cumulative distributions of the number of localizations of GABA$_A$Rs per synapse.

The cumulative distribution on the left shows the increase of GABA$_A$Rs localizations in iLTP samples where we labeled α_1 subunit of receptor in respect to control samples. The cumulative distribution on the right shows the increase of GABA$_A$Rs localizations in iLTP samples where we labeled α_2 subunit of receptor in respect to control samples.

during plasticity, as shown in **figure 3.7**. These percentages are consistent with the reported enhancement of GABAergic currents as a consequence of iLTP (Marsden et al., 2007).

3.4.3 Rearrangement of GABA$_A$Rs in a larger number of SSDs during iLTP

Another important quantitative information we obtained from our approach is the number of SSDs at the inhibitory synapse. We observed that in iLTP samples GABA$_A$ receptors are reorganized in a larger number of SSDs per synapse for both isoforms, α_1-GABA$_A$R and α_2-GABA$_A$R (**figure 3.8)**.

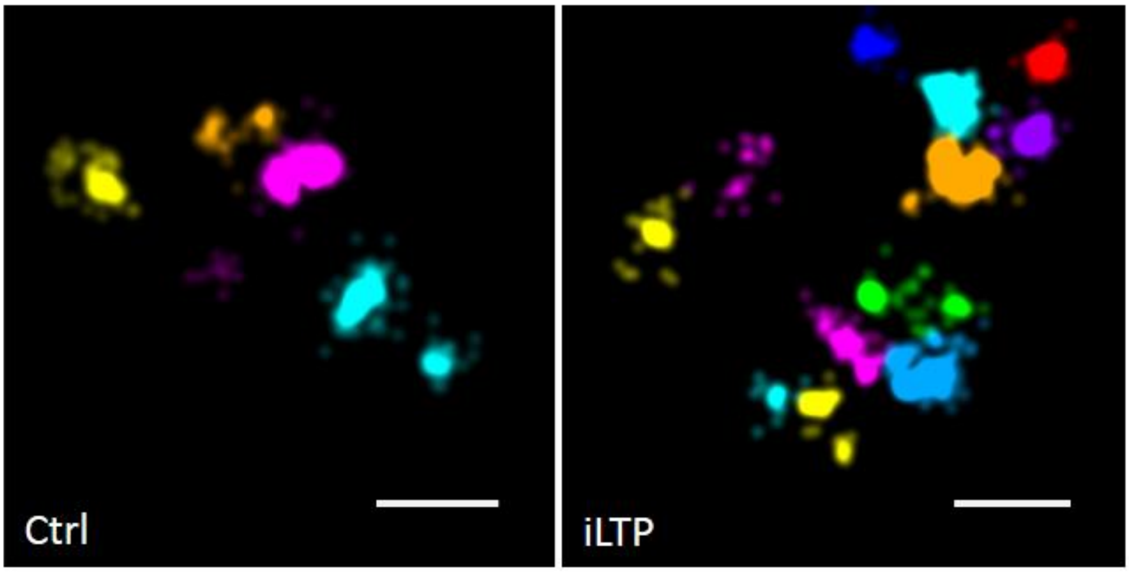

Figure 3.8 Representative images of GABA$_A$R SSDs per synapse in control samples and in iLTP samples. Scale bars, 200 nm.

By plotting the relative frequency of synapses with progressive numbers of SSDs per synapse as a histogram, we noticed an inversion of trend between synapses with a number of SSDs less than or equal to 3, and synapses with a number of SSDs greater than or equal to 4, for both isoforms (**figure 3.9**). In fact, despite synapses with a low number of SSDs are more represented both in control and in plasticity, we report a greater fraction of crowded synapses (i.e., with a number of SSDs per synapse greater than 3) in iLTP samples compared with control conditions (**figure 3.10**).

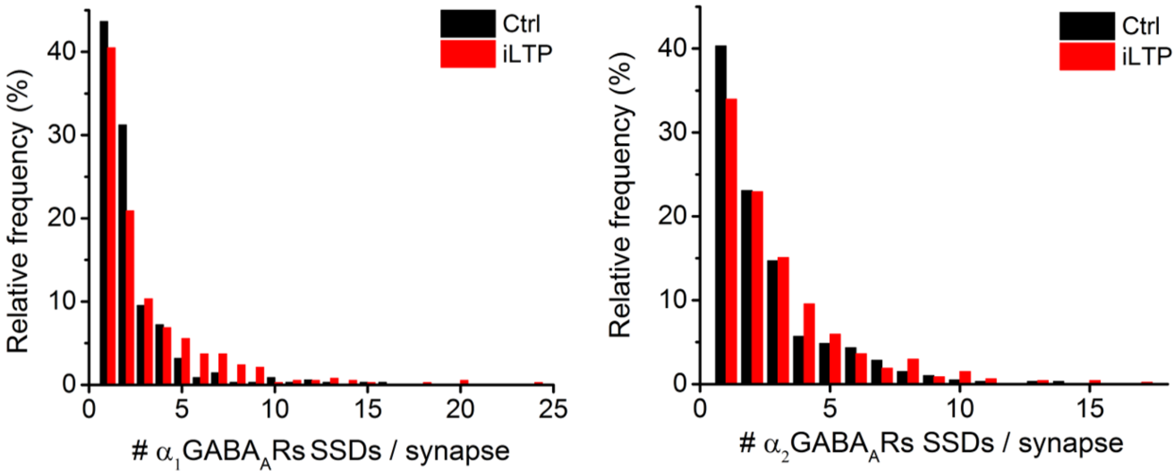

Figure 3.9 Corresponding histograms of the number of GABA$_A$R SSDs / synapse in Ctrl and iLTP samples.

The histogram on the left displays the relative frequency of synapses with 1, 2, 3, 4, etc. α_1-GABA$_A$R SSDs in control samples (black) and iLTP samples (red). The histogram on the right displays the relative frequency of synapses with 1, 2, 3, 4, etc. α_2-GABA$_A$R SSDs in control samples (black) and iLTP samples (red). For both isoforms of the receptor, synapses with a number of SSDs greater than or equal to 4 are more frequent in samples under plasticity conditions.

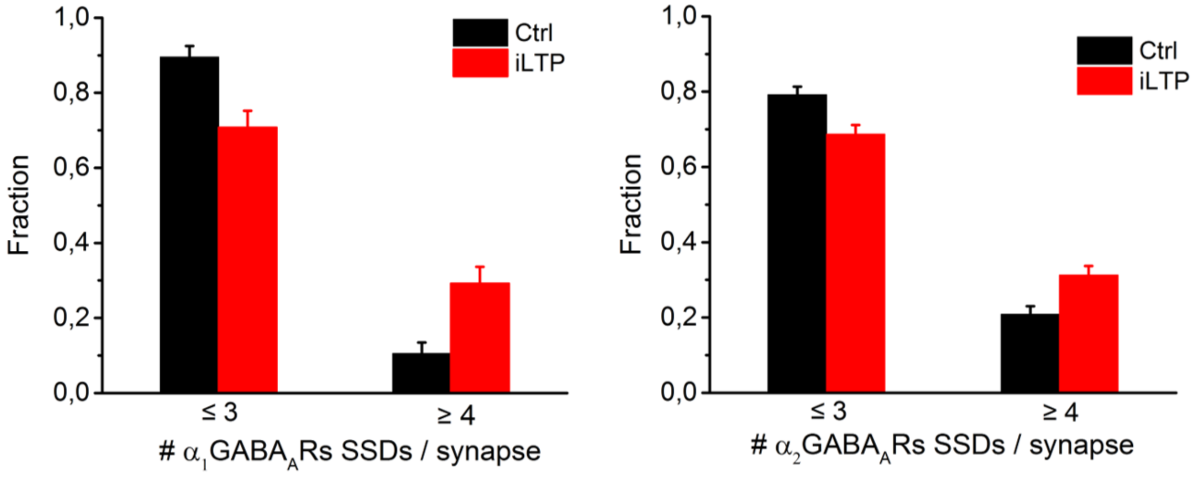

Figure 3.10 Fraction of synapses with a number of SSDs less than or equal to 3 and synapses with a number of SSDs greater than or equal to 4.

The left graph is referred to α_1-GABA$_A$R SSDs and the right one to α_2-GABA$_A$R SSDs. Data are presented as mean ± SE.

3.4.4 Nanoscale organization of GABA$_A$Rs inside subsynaptic domains

Although inhibitory postsynaptic GABA$_A$R SSDs have been described in a recent work (Crosby et al., 2019), to date there is no study quantifying the receptor density at a molecular level. Our approach is not limited to disclosing the number and size of SSDs at the PSD, but also reveals the number of localizations of GABA$_A$R per SSD, the area of SSDs and their density, calculated as the number of localizations divided to the area. Moreover, we report these data for two GABA$_A$R isoforms, underlining differences between the basal condition and the plasticity condition.

We found considerable differences between α_1-GABA$_A$R and α_2-GABA$_A$R SSDs reshaping during iLTP. As shown by cumulative distributions of frequency in **figure 3.11**, the number of localizations of α_1-GABA$_A$R per SSD slightly decreases in stimulated samples in respect to control samples (Ctrl: 134.3 ± 4.8; iLTP: 122.3 ± 2.8; n = 781 and 1161, respectively, $p < 0.05$, Student's *t* test), while the number of localizations of α_2-GABA$_A$R per SSD slightly increase in iLTP samples (Ctrl: 117.5 ± 2.4; iLTP: 126.7 ± 2.8; n = 1569 and 1383, respectively, $p < 0.05$, Student's *t* test).

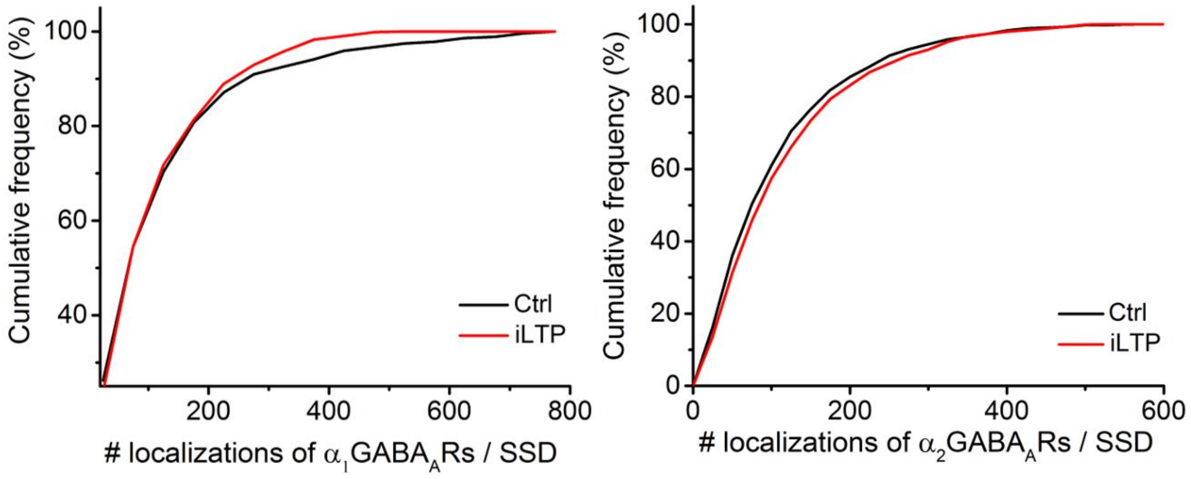

Figure 3.11 Cumulative distributions of the number of localizations of GABA$_A$Rs per SSD.

The cumulative distribution on the left shows that the number of localizations of α_1-GABA$_A$R is lower in iLTP samples than in control samples (9% decrease). The cumulative distribution on the right displays that the number of localizations of α_2-GABA$_A$R is upper in iLTP samples (8% increase).

The sizes of SSDs were calculated as the standard deviation of the x-y coordinates from the relative cluster centroids. Hence, we approximated SSDs to circles in order to determine areas. Again we detected differences between the two isoforms; α_1-GABA$_A$R SSDs are bigger in control samples than in iLTP ones (Ctrl: 649.1 ± 16.4; iLTP: 724.7 ± 15.3; n = 765 and 1142, respectively, $p < 0.01$, Student's *t* test), instead there is no difference between control and iLTP SSDs for α_2-GABA$_A$R (Ctrl: 617.5 ± 10.7; iLTP: 606.4 ± 10.6; n = 1541 and 1354, respectively, nonsignificant, Student's *t* test) (**figure 3.12**).

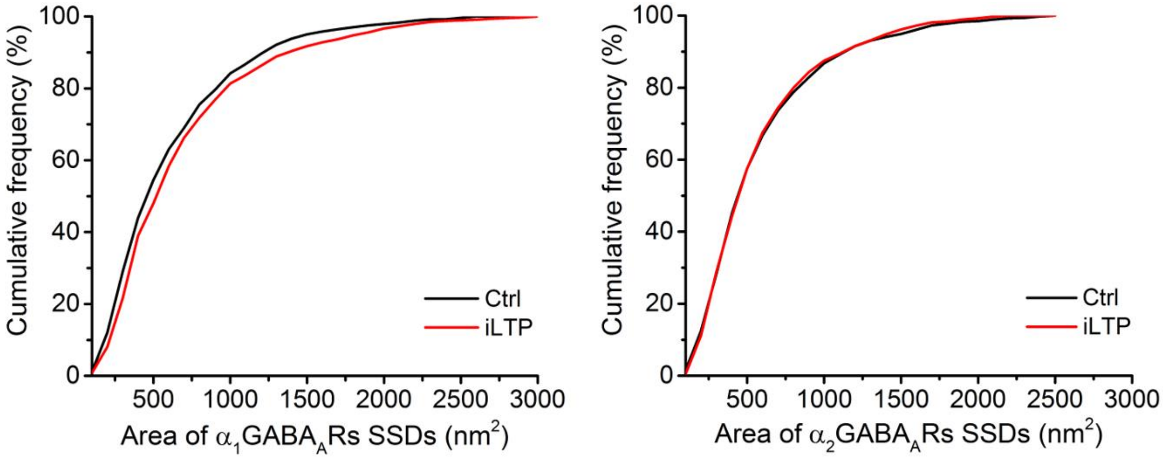

Figure 3.12 Cumulative distributions of the areas of GABA$_A$R SSDs.

Left, cumulative distribution of the areas of α_1-GABA$_A$R SSDs under basal conditions (black) and during iLTP (red), showing an increase of SSDs area in stimulated samples (12% upper). Right, cumulative distribution of the areas of α_2-GABA$_A$R SSDs under basal conditions (black) and during iLTP (red), where the two curves overlap each other, meaning that there is not significant difference between the two conditions.

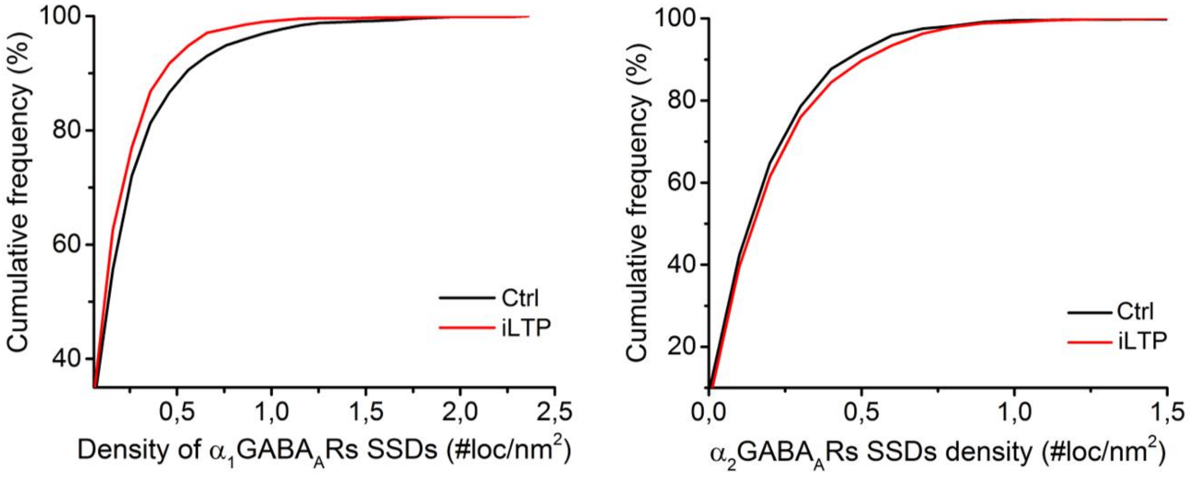

Figure 3.13 Cumulative distributions of the densities of GABA$_A$R SSDs.

Left, cumulative distribution of the densities of α_1-GABA$_A$R SSDs under basal conditions (black) and during iLTP (red), showing a decrease of SSDs density in stimulated samples (17% lower). Right, cumulative distribution of the densities of α_2-GABA$_A$R SSDs under basal conditions (black) and during iLTP (red), displaying an increase of SSDs density in iLTP samples (9% upper).

At last, we calculated the density of receptor SSDs by dividing the number of localizations/SSD by the areas, and we found that for α_1-GABA$_A$R SSDs, the density decreases in stimulated samples (Ctrl: 0.269 ± 0.010; iLTP: 0.223 ± 0.006; n = 765 and 1142, respectively, $p < 0.01$, Student's *t* test), whereas α_2-GABA$_A$ SSDs are denser in iLTP neurons (Ctrl: 0.236 ± 0.005; iLTP: 0.258 ± 0.006; n = 1541 and 1354, respectively, $p < 0.01$, Student's *t* test) (**figure 3.13**).

3.4.5 SSD characteristics as a function of the number of SSDs per synapse

As mentioned previously (page 57 and figure 3.10), it is possible to identify two categories of synapses, based on their number of SSDs, which are differently represented in control samples and stimulated samples. The first category consists of synapses with 3 or fewer SSDs, which we will call from now "category A" to simplify. The second one consists of synapses with 4 or more SSDs, which we will call "category B".

Since for both α_1 and α_2 subunits in plasticity samples there is a decrease of the number of A-synapses and an increase of the number of B-synapses, in respect to control samples (**figure 3.10**), we decided to investigate further how the characteristics of SSDs change, with the induction of iLTP, as a function of their belonging to synapses A or B. However, please note that synapses belonging to category A are more represented both in control and in plasticity as reported by the histogram in **figure 3.10**.

We report that, in the case of α_1 subunit, SSDs belonging to synapses of type A (#SSDs/syn ≤ 3) show a 15% decrease in GABA$_A$R localizations number in iLTP samples, whereas SSDs belonging to synapses of type B (#SSDs/syn ≥ 4) show a 42% increase in localizations number in iLTP (**figure 3.14**, left side). In the previous paragraph, we showed that the global number of localizations of α_1-GABA$_A$R per SSD slightly decreases under plasticity conditions, but this is explained by the fact that synapses of type A are much more represented than synapses of type B, as already stressed.

Regarding α_2 subunit, SSDs in synapses of type A do not vary in the localizations number between control and iLTP samples, whereas SSDs of type B synapses exhibit a 16% increase in localizations number (**figure 3.14**, right side).

In addition, the areas of α_1 SSDs in synapses A remain quite the same in iLTP samples; instead, α_1 SSDs belonging to synapses B in iLTP neurons have an average area almost 50% larger than in controls (**figure 3.15**, left side). In this case, we could affirm that the increase of the α_1 SSDs area, showed in **figure 3.12**, is entirely driven by the synapses with 4 or more SSDs.

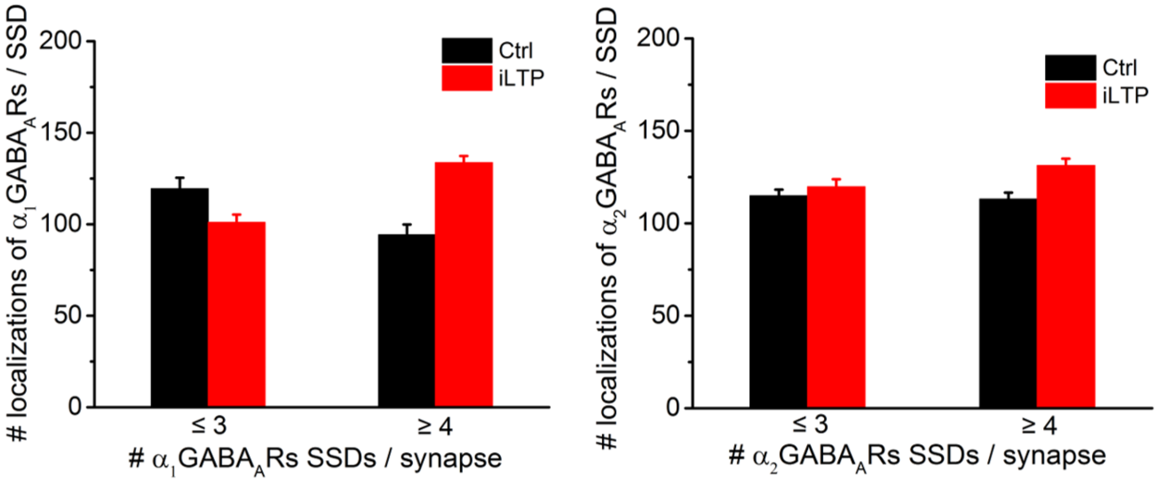

Figure 3.14 Number of localizations of α_1-GABA$_A$R and α_2-GABA$_A$R per SSD as a function of the number of SSDs per synapse.

The left bar plot is referred to α_1-GABA$_A$R SSDs and the right one to α_2-GABA$_A$R SSDs. Data are presented as mean ± SE.

For α_2 SSDs, on the contrary, we had reported no significant differences between SSDs area in control samples and SSDs area in iLTP samples (**figure 3.11**). Also, considering the average area of SSDs belonging to category A or category B, there are no differences between controls and iLTP neurons (**figure 3.14**, right side).

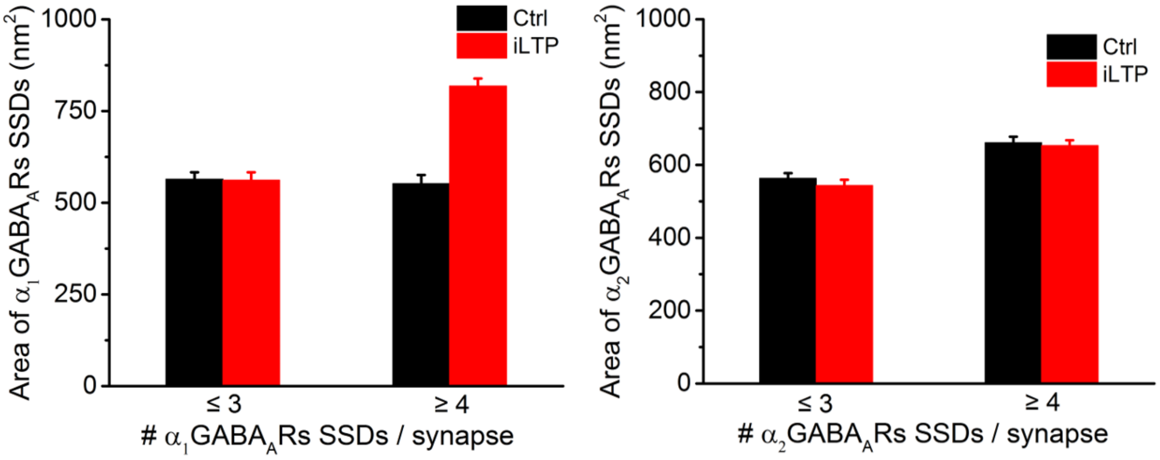

Figure 3.15 Average area of α_1-GABA$_A$R and α_2-GABA$_A$R SSDs as a function of the number of SSDs per synapse.

The left bar plot is referred to α_1-GABA$_A$R SSDs and the right one to α_2-GABA$_A$R SSDs. Data are presented as mean ± SE.

Finally, we plotted the average density of SSDs, in controls and under plasticity, as a function of the number of SSDs per synapses. In the bar plots in **figure 3.16** (left side), we can see that the average density of the α_1 SSDs belonging to category A in samples under plasticity is 14% lower than control samples. Instead, the difference between control and iLTP of α_1 SSDs is not significant for SSDs belonging to category B synapses. For α_2 SSDs, we report a 19% increase of the average density of SSDs belonging to category B synapses, whereas SSDs in synapses of category A do not show significant differences in density (**figure 3.16**, right side).

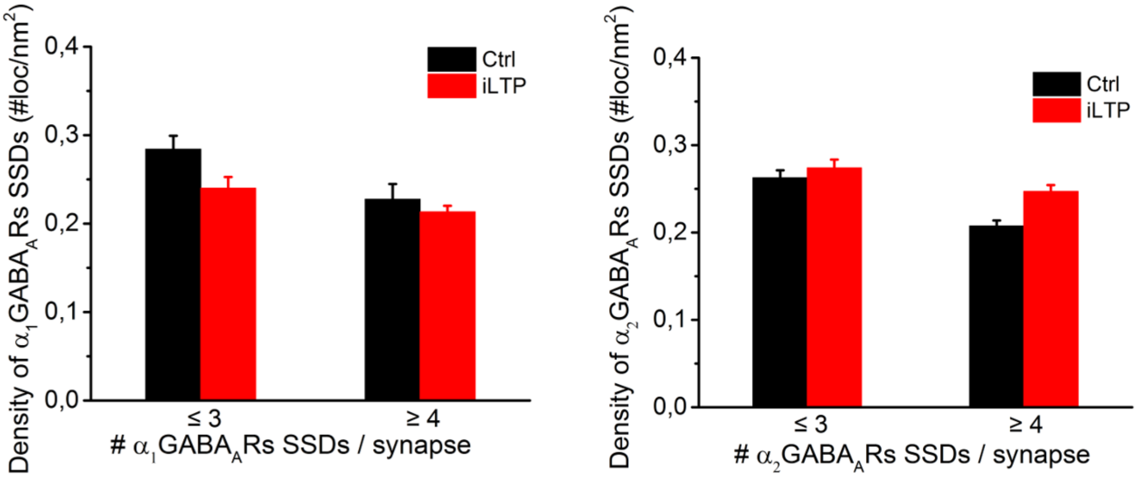

Figure 3.16 Average density of α_1-GABA$_A$R and α_2-GABA$_A$R SSDs as a function of the number of SSDs per synapse.

The left bar plot is referred to α_1-GABA$_A$R SSDs and the right one to α_2-GABA$_A$R SSDs. Data are presented as mean ± SE.

3.5 Discussions

Since the constant dynamic movement of synaptic components is a key feature of neurotransmission and its plasticity (Choquet and Triller, 2013), several studies have focused on the nanoscopic events pertinent to synaptic plasticity over the last years. These studies have shed light on many details of the spatial distribution and density of the main synaptic players, impossible to be visualized before the advent of super-resolution.

However, the detection of SSDs with super-resolution microscopy remains challenging due to intrinsic technical and biological limitations. Many circumstances need to be taken into account in detecting clustered proteins using SMLMs (Yang and Specht, 2019). The most biologically relevant features of SSDs are their size, the number of SSDs per synapse, and the number of proteins per SSD. Unfortunately, the measured size of SSDs seems to be dependent on the imaging technique employed to measure it. SMLMs, STED, and SIM detected a wide range of SSD sizes, with a lower limit of ~ 50 nm that reflects the spatial resolution of super-resolution imaging. Even in the case of the identification of the number of SSDs per synapse, it is likely that different imaging and quantitative analysis methods can again affect the results differently. Finally, the measurement of the number of proteins forming SSDs remains a difficult task due to uncertainty in labeling stoichiometry.

In this thesis, we proposed a method to achieve quantitative information about how the characteristics of $GABA_AR$ SSDs change under basal conditions and during synaptic plasticity, bypassing the issues above mentioned. In order to unveil the molecular mechanisms underlying plasticity of inhibition is crucial to reveal in which way SSDs adapt dynamically to changes in synaptic strength. By comparing cluster analysis of localization data sets provided by STORM imaging of $GABA_AR$ in control neurons and iLTP neurons, we can contribute to the current attempts in the understanding of neurotransmission plasticity with state-of-art results.

Having conducted all the experiments in the precisely same experimental and analysis conditions, we can report the occurring changes in plasticity conditions, in terms of the number of receptors per synapse, number of SSDs per synapse, number of receptors per SSD, and SSDs size and density at the nanoscale level.

Furthermore, we performed the same set of experiments on two different subunits of $GABA_AR$, α_1 and α_2, that lead us to discover significant divergences between them, supporting the hypothesis that subunit composition of $GABA_AR$ is a determinant in the expression of inhibition. Please note that a comparison between the quantitative data obtained with the labeling of the two subunits would not be reliable, since we obviously utilized two distinct primary antibodies, one specific for α_1-$GABA_AR$ and the other specific for α_2-$GABA_AR$, that perform differently. Therefore, we limited our observations on the diverse response of the receptor subtypes to iLTP.

We reported an increase of the number of $GABA_AR$s per synapse for both receptor subtypes during iLTP as expected, since the number of receptors at the synapse is directly related to the strength of synaptic transmission (Fukazawa and Shigemoto, 2012; Tarusawa et al., 2009). We can thus suggest that both subtypes are responsible for the enhancement of GABAergic currents during inhibitory synaptic plasticity described in previous studied (Nusser et al., 1998; Petrini et al., 2014).

Our findings also revealed the fragmentation of the receptor at the synapse. Although most synapses contain fewer than 3 SSDs both in control and iLTP, we found a larger fraction of synapses with 4 or more SSDs in plasticity samples. That could be the answer to the open question about if the presence of multiple SSDs weighs on the regulation of synaptic function. The emergence of new SSDs on the postsynaptic membrane could be the key of the inhibitory plasticity. Moreover, the increased fragmentation of GABA$_A$R in plasticity is in accordance with the reported rearrangement of gephyrin in a multi-nanodomain scaffold at the postsynapse during iLTP (Pennacchietti et al., 2017).

Until now, α_1-GABA$_A$R and α_2-GABA$_A$R showed no difference in their response to the induction of plasticity. It is in the organization of receptors in SSDs that we detected differences between them (**figure 3.17**). In plasticity, the number of receptors per SSD decreases for α_1 and increases for α_2. Hence, the overall increase of GABA$_A$Rs at the inhibitory synapse under plasticity conditions could be the result of different trafficking processes: α_1 goes out of SSDs and forms new ones, while α_2 moves from extrasynaptic areas to the synaptic site and enrich existing SSDs or forms new ones. Besides, SSDs average area undergoes an increase in plasticity for α_1-GABA$_A$R, while α_2-GABA$_A$R shows no changes, thus leading to a decrease of SSDs average density for α_1 and an increase for α_2.

In addition, since we suppose that the increment of the number of synapses with 4 or more SSDs in iLTP neurons is a key process in the expression of synaptic plasticity, we also examined SSDs characteristics as a function of the number of SSDs per synapse. We found that crowded synapses contribute in a different manner to the iLTP response for α_1 and $\alpha_{2.}$

The dissimilarities in the behavior of the two subtypes of GABA$_A$R remain an incomplete puzzle that requires further investigations, in order to answer to opening question regarding the possible coexistence of the two subunits in the same receptor or if α_1 and α_2 receptor subtypes play different role in the inhibition of neurotransmission.

A detailed portrait of the spatial organization and real copy number of receptors inside SSDs is still a challenge nowadays. However, the quantification of the size and density of SSDs here reported is at the cutting edge in the worldwide research effort aspiring to obtain a clearer painting of the molecular mechanisms underlying the regulation of the inhibitory neurotransmission.

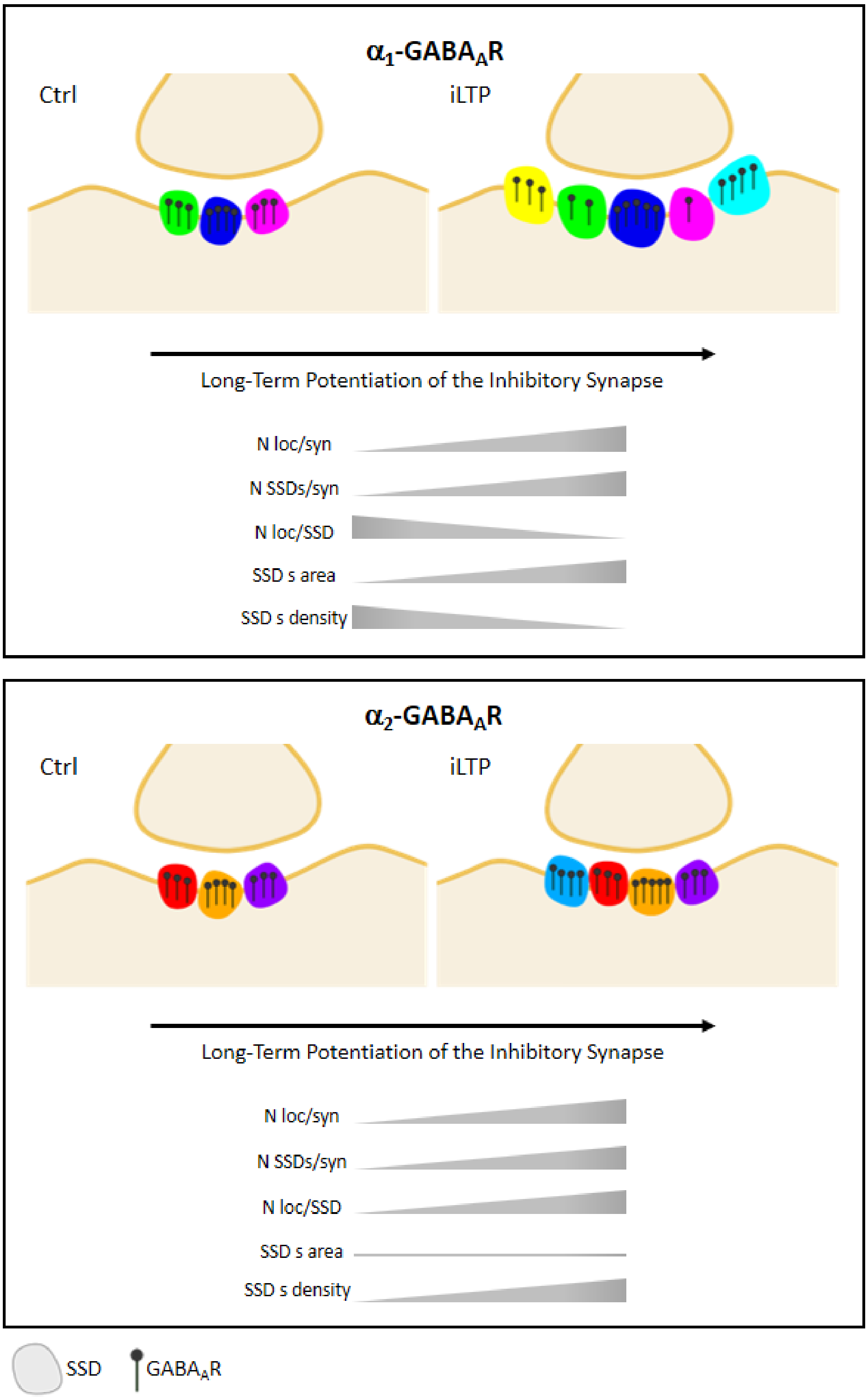
α1-GABAAR
Ctrl
iLTP
Long-Term Potentiation of the Inhibitory Synapse
N loc/syn
N SSDs/syn
N loc/SSD
SSD s area
SSD s density
α2-GABAAR
Ctrl
iLTP
Long-Term Potentiation of the Inhibitory Synapse
N loc/syn
N SSDs/syn
N loc/SSD
SSD s area
SSD s density
SSD
GABAAR

Figure 3.17 Summary of results in the quantitative investigation of the spatial distribution of two subtypes of GABA$_A$R under plasticity conditions.

Top panel, rearrangement of α_1-GABA$_A$R in iLTP neurons; the receptor arranges itself in a larger number of SSDs per synapse, with an average area of SSDs bigger than in control; localizations per SSD decrease as well as the average density of SSDs. The total amount of receptors at the synapse rises in plasticity.
Bottom panel, rearrangement of α_2-GABA$_A$R in iLTP neurons; the receptor arranges itself in a larger number of SSDs per synapse, with an average area of SSDs equal to control; localizations per SSD increases as well as the average density of SSDs. The total amount of receptors at the synapse rises in plasticity.

Chapter 4

Adhesion and migration of neurons on single-layer graphene

> *"Graphene is a single plane of graphite that has to be pulled out of bulk graphite to show its amazing properties."*
>
> Sir Andre Konstantin Geim
> (Nobel Prize for Physics in 2010)

Since its discovery in 2004, graphene has definitely emerged as a promising nanomaterial thanks to its unique combination of properties. Graphene potentials go beyond electronics, batteries, and other physical applications; its mechanical and conductive features has also stricken the field of biomedical engineering. As a new biocompatible nanostructured material, graphene is the ideal candidate for biosensors, tissue engineering, drug delivery, etc.

The employment of graphene and its derivatives in the biological context requires a depth characterization of its interaction with biological samples. Recent studies report neurons affinity for single-layer graphene and the possibility to design geometrically ordered neural networks by seeding neurons on micropatterned graphene substrates.

In order to reveal the molecular mechanism underlying the propensity of neurons to migrate to and grow on graphene instead of glass, we exploited STORM imaging and cluster analysis to quantify the adhesion protein vinculin in neurons seeded on both substrates.

4.1 Nanomaterials and biological samples interaction

In the last years, the rise of a new family of carbon-based nanomaterials have drawn an increasing level of attention in the scientific community. Thanks to their unusual properties, they have potentially broad applications in various fields.

Since 2004, when it was discovered and characterized (Novoselov et al., 2004), *graphene* has emerged as a promising nano-platform with a wide potential for biomedical engineering, translational medicine and biotechnology (Ferrari et al., 2015; Yin et al., 2017). In fact, because of their chemical, physical, and mechanical properties, graphene and its derivatives are undeniable ideal candidates for biosensors (Kuila et al., 2011; Wang and Dai, 2015), tissue engineering (Dvir et al., 2011; Lee et al., 2011; Menaa et al., 2015; Zhang and Webster, 2009), tissue scaffold (Kalbacova et al., 2010; Nayak et al., 2011), gene therapy (Draz et al., 2014; Feng et al., 2011), drug delivery (Farokhzad and Langer, 2009; Sun et al., 2008) and bioimaging probes (Bartelmess et al., 2015; Feng and Liu, 2011; Yoo et al., 2015; Zhang et al., 2010).

However, the employment of graphene-related nanomaterials in a biological context necessitates a detailed characterization to document the effects of the interaction between graphene and different organizational levels of living systems, ranging from biomolecules to cells.

4.1.1 Graphene: the "wonder material"

Graphene is a monolayer material composed of sp^2 carbon atoms hexagonally arranged in an atomically thick two-dimensional sheet. The authors, Geim and Novoselov, were deservedly awarded the Nobel Prize for physics in 2010.

Graphene has immediately attracted a keen interest due to its unique properties, and the related research has accelerated exponentially since its discovery. According to Scopus (bibliographic database), thousands of papers have been written about graphene since 2005, and in 2013 the academic publications reporting the use of graphene was so abundant that it equalizes to over 40 publications per day (Randviir et al., 2014).

Graphene can be isolated from its three-dimensional parent material *graphite* (**figure 4.1**), by repeated mechanical exfoliation of graphite flakes using adhesive tape, the so called 'Scotch Tape' method (Novoselov et al., 2004) or grown on substrates by chemical vapor deposition (CVD) or decomposition of carbide phases (Sprinkle et al., 2010). It is also the building block of *carbon nanotubes* (CNT) (**figure 4.1**).

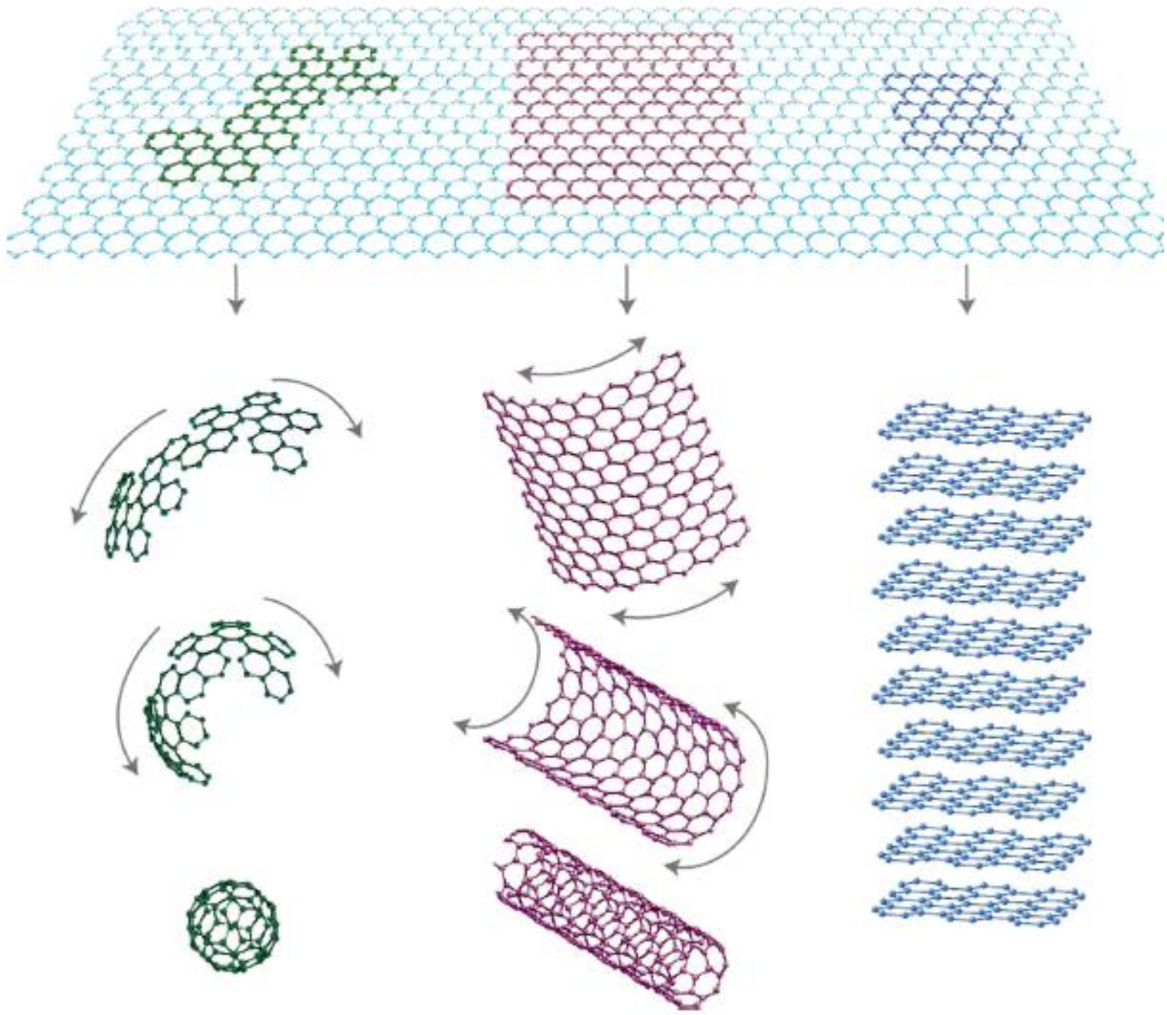

Figure 4.1 Graphene (top) and related structures: fullerene (bottom left); carbon nanotubes (bottom centre); and graphite (bottom right) (Randviir et al., 2014).

Graphene possesses very high mechanical strength, surface area, and thermal and electrical conductivity. Moreover, it can be easily functionalized by chemical modification. Graphene-related nanomaterials have been developed in many different forms in terms of shape, size, and surface modifications that provide them versatile physical, chemical, and biomedical characteristics.

In biomedical applications, the major advantage of graphene-related nanomaterials is their high specific surface area, which allows high-density bio-functionalization or drug loading (Sanchez et al., 2012).

4.1.2 Adhesion and proliferation of neurons on graphene

As mentioned before, graphene shows high transmittance and conductivity. Because neurons functions are based on electrical activity, this property of graphene may be ideal for the development of neural models in biomedical applications (Ryu and Kim, 2013).

A study published in 2011 examined the effects of neurons on graphene, proving excellent biocompatibility of graphene with neural cells. Moreover, this study report that the growth and vitality of neurons on graphene were significantly enhanced compared to the conventional culture substrates (Li et al., 2011).

In addition to conductivity, graphene also has other unique features, such as elasticity and protein or small molecules absorption that may alter the direction of cell proliferation. This capability can be exploited for *cell patterning* that plays a crucial role in tissue engineering and biosensing to control cell position and guide them to specific locations. In fact, it is known that a patterned surface may affect many cellular processes such as cell-cell communication and migration (Ventre et al., 2014) and cell differentiation (Recknor et al., 2006).

Among the many different graphene species, *single-layer graphene* (SLG), obtained by CVD, offer some advantages in the field of biomedical applications since it can be easily conveyed onto any other substrates (Suk et al., 2011), and it can be patterned (Park et al., 2012; Strong et al., 2012).

A recent study showed that a patterned surface of SLG promotes ordered neuron growth because of the inclination of hippocampal neurons to adhere to SLG regions (Lorenzoni et al., 2013). Lorenzoni and co-workers grew the SLG on Cu foils via CVD process and then they transferred SLG on glass substrates that are usually employed for cell cultures. SLG was machined in stripe-pattern by laser ablation, then sterilized in ethanol, and coated with poly-D-lysine (PDL) to promote cell adhesion and growth. Neurons were plated on the graphene/glass substrate and their growth was followed by optical microscopy since the transparency of graphene allows observation of the neuron’s morphological changes. At DIV7, neurons arranged preferentially on the graphene surface, leaving the glass surface almost free of cells, demonstrating an ordered interconnected neuron pattern that mimicked the surface pattern design.

In order to investigate the cell response to the surface cues of micropatterned SLG/glass substrate, the same group tested Chinese hamster ovary (CHO) cells on PDL-coated micropatterned SLG substrates and quantified the adhesion by using single-cell force spectroscopy (Keshavan et al., 2017). They reported an enhanced cell adhesion on SLG and the initial CHO cell accumulation on the graphene regions, confirming the neuronal behavior. However, at DIV2, CHO cells migrated onto the adjacent SLG-ablated areas, apparently more advantageous for cell proliferation. These findings might indicate that the interplay of cells with surface cues is a cell-type dependent mechanism.

This cell-type dependent response may be induced by several factors, ranging from the different characteristics of the cell membranes to the differences in the cell functionality.

4.2 Quantification of adhesion proteins in epithelial cells and neurons on SLG

From the studies previously mentioned, it is evident that cell adhesion machinery is influenced by graphene micropatterned substrates. How graphene causes the enhancement of neuron and CHO cell adhesion has not still been understood.

Cell adhesion and migration rely on the growth of *focal adhesions* (FA), which are macromolecular assemblies connecting the intracellular actin network with the extracellular matrix (ECM). They transmit mechanical forces and regulatory signals by linking the membrane to the cytoskeleton (Wehrle-Haller, 2012). In details, they consist of large complexes of transmembrane integrins whose intracellular domain binds to the cytoskeleton through adapter proteins, such as talin, α-actinin, paxillin, vinculin, and tensin. During cell migration, both the composition and the morphology of the focal adhesion change dynamically.

We hypothesized that the molecular mechanism underlying cell migration on graphene implies modifications in the protein amount involved in the formation of focal adhesions. In order to verify our hypothesis or to make at least new steps in understanding the processes that make possible cell patterning on nanostructured materials at a nanoscale level, we applied quantitative STORM to quantify vinculin in CHO cells first, and in neurons after.

In the past, single-molecule localization microscopies (SMLMs) have been widely employed in the study of focal adhesions shedding light on the nanoscale protein organization. For example, two-color PALM has been used to determine colocalization of vinculin and paxillin, showing that they actually form nano-aggregates (Shroff et al., 2007), whereas talin plays a central role in organizing the focal adhesion strata (Kanchanawong et al., 2010).

As in the previous chapter, we overcome the issues regarding the quantification of the real protein copy number by comparing the number of localizations of vinculin in cells lying on SLG areas and in cells lying on glass areas.

4.3 Materials and methods

4.3.1 Single-layer graphene/glass substrate fabrication

Commercially available CVD grown SLG on copper (Cu) (2D Tech, UK) was transferred on glass coverslips by wet etching technique on Cu as following the protocol reported in (Keshavan et al., 2017). The transferred SLG was ablated by laser micromachining following the protocol previously optimized and described by (Lorenzoni et al., 2013). The result was a coverslip half SLG and half glass. The substrates were coated with 0.1 mg/mL poly-D-lysine (PDL, Sigma-Aldrich) for 3h in incubator and rinsed with sterile deionized water.

4.3.2 Cell cultures

Chinese hamster ovary cell lines (ATCCs, CCL-61T, UK) were cultured under standard conditions in Dulbecco’s modified eagle medium (DMEM) for 2 DIV.

Primary hippocampal neurons were prepared from E18 rat. Neurons were plated in serum-free Neurobasal-A medium (Invitrogen, Italy) supplemented with Glutamax (Invitrogen, Italy) 1%, B-27 (Invitrogen, Italy) 2%, at 37°C in 5% CO_2 for 1 DIV.

4.3.3 Immunostaining protocol

Cells (CHO or neurons) were fixed with 3% (w/v) paraformaldehyde (PFA) in phosphate-buffered saline (PBS) for 7 min at room temperature (RT). After washing 3 times in PBS, cells were incubated with a blocking buffer solution containing 3% (w/v) bovine serum albumin (BSA, Sigma-Aldrich) and 0.2% Triton X-100 (Sigma-Aldrich) for 40 min at RT to prevent non-specific binding and permeabilize cell membrane.

Immunolabeling of vinculin was performed incubating cells with an anti-vinculin rabbit primary antibody (PA5- 19842, Thermo Fisher) at RT for 1h, followed by 45 min incubation with a custom built anti-rabbit secondary antibody conjugated with the dye pair Alexa Fluor 405/Alexa Fluor 647 (conjugation protocol in the following paragraph) at RT.

At the end of the immunostaining, samples were fixed again in PFA 2% for 5 min and stored in PBS at 4°C

4.3.4 Activator-reporter dye pairs preparation protocol

For the preparation protocol of the dye pair we refer to paragraph 3.3.4 at page 55.

4.3.5 STORM imaging and data reconstruction

STORM microscope

For the technical specifications of STORM microscope, refer to paragraph 3.3.5, page 56.

Imaging buffer

All samples were imaged in the GLOX imaging buffer (page 31, 56), (Bates et al., 2007).

Imaging protocol

Imaging was performed by acquiring 20,000 frames of 647 channel with an exposure time of 30 ms. The 647 nm laser was used for exciting the reporter dye (Alexa 647) and switching it to the dark state. The 405 nm laser light was used for reactivating the reporter into a fluorescent state via the activator dye (Alexa 405). An imaging cycle was used in which one frame belonging to the activating light pulse was alternated with three frames belonging to the imaging light pulse.

Analysis of raw STORM data

The images reconstruction was performed using the custom software (Insight3, kindly provided by Dr. Bo Huang of University of California). Refer to paragraph 3.3.5, page 57.

4.3.6 Cluster analysis

Cluster analysis of STORM localization data was performed with the MATLAB custom-written code (Ricci et al., 2015), described in the paragraph 3.3.6, page 57. Before analyzing localization data, we optimized clustering factors and parameters to obtain the best performance of the algorithm on vinculin.

4.3.7 Statistical analysis

All statistical tests were performed in OriginPro2016. Data were tested with unpaired two-tailed Student’s *t* test. P-values were considered significant if < 0.05. Bar graphs are displayed as mean ± standard error of mean (SEM), unless otherwise noted.

4.4 Results

To determine if graphene affects the focal adhesions of cells seeded on it, maybe influencing the geometry and thickness of the poly-D-lysine coating that influences the adhesion machinery in turn, we aimed to quantify the adhesion protein vinculin in cells adhered to glass and in cells adhered to graphene.

Initially, we conducted our experiments with CHO cells, previously employed to measure cell adhesion forces by single-cell force spectroscopy (Keshavan et al., 2017). Then we moved onto neurons, as the most attractive application of growing cells on graphene could be to create geometrically ordered neural networks for biomedical applications.

4.4.1 Quantification of vinculin in CHO cells

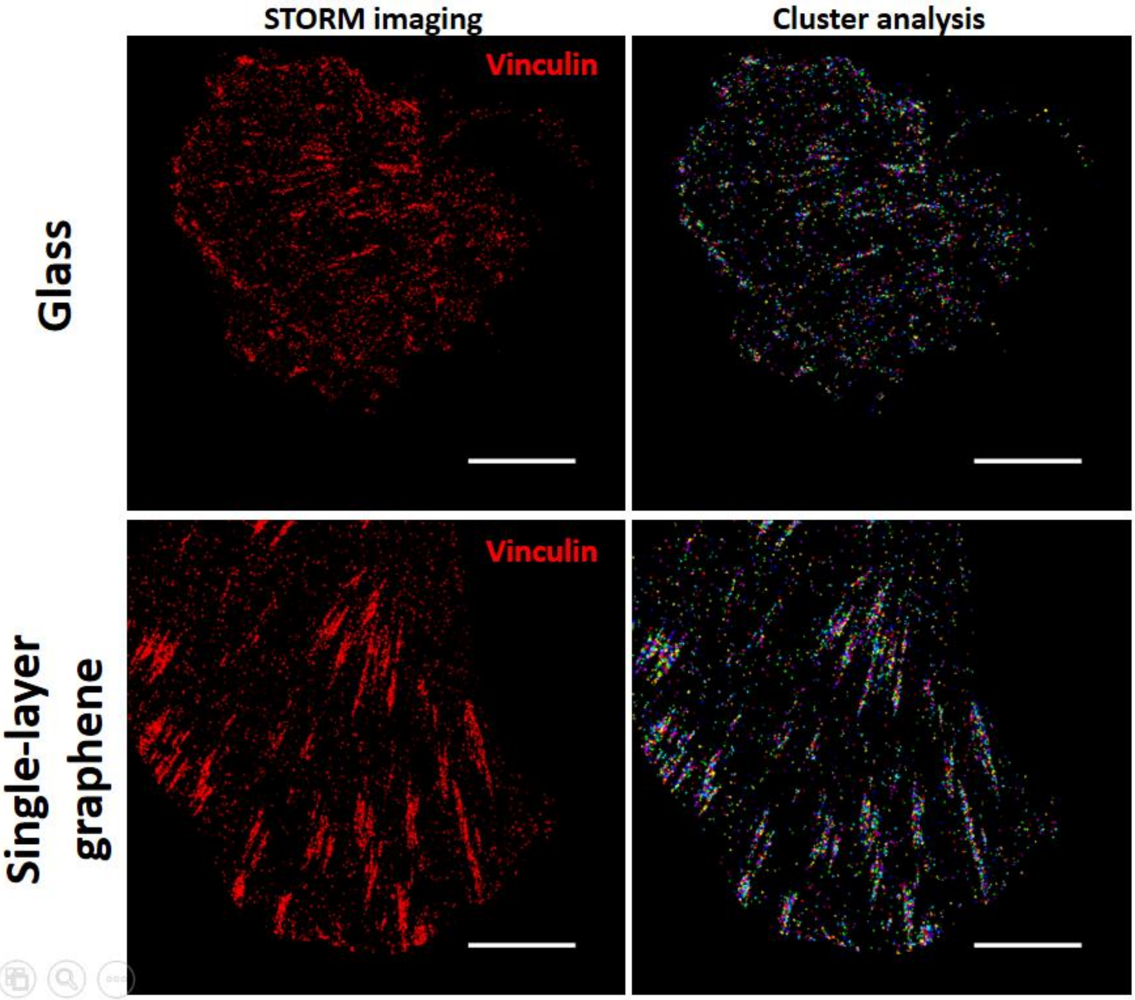

Figure 4.2 STORM imaging and cluster analysis of CHO cells adhered on glass and SLG. Scale bars, 5 µm.

We used 2D STORM to acquire super-resolution images of vinculin in DIV2 Chinese hamster ovary cells. As reported by Keshavan and co-workers, at DIV2 CHO cells preferentially arrange on graphene rather than on glass, and then migrate to the latter in the following days of culture (Keshavan et al., 2017).

STORM images show that there are morphological differences between the cells on SLG and the few cells adhered on glass. Cells on glass are smaller and more rounded than cells on graphene that are flatter and bigger. Moreover, vinculin forms larger macromolecular assemblies shaped as stripes crossing the entire imaged region, which are absent in cells seeded on SLG (**figure 4.2**).

By processing STORM images with the distance-based clustering algorithm, we quantified vinculin localizations per nanodomain. We found that on graphene, the number of vinculin localizations per nanodomain is higher than on glass (from 54.17 ± 0.48 in cells on glass to 92.82 ± 0.68 in cells on SLG, n = 5646 and 21701, respectively, $p < 0.01$, Student's *t* test). Therefore, we observed a 42% increase of vinculin localizations per nanodomain, as shown in **figure 4.3**.

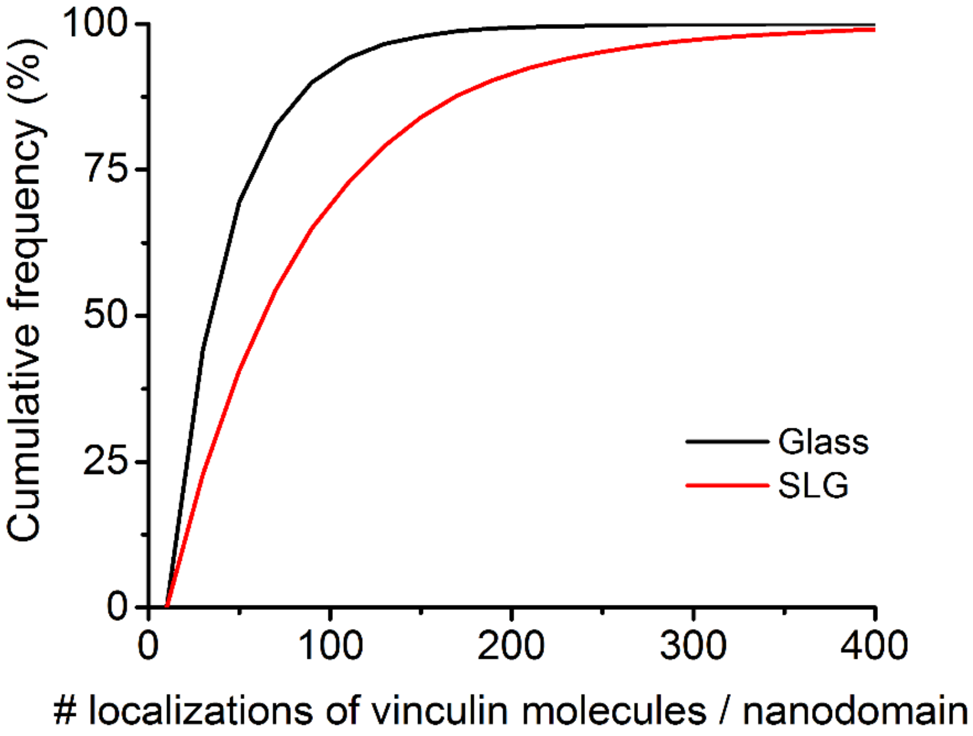

Figure 4.3 Cumulative distributions of the number of localizations of vinculin per nanodomain.

The cumulative distribution shows the 42% increase of vinculin localizations in cells adhered on SLG in respect to cells adhered on glass.

4.4.2 Quantification of vinculin in neurons

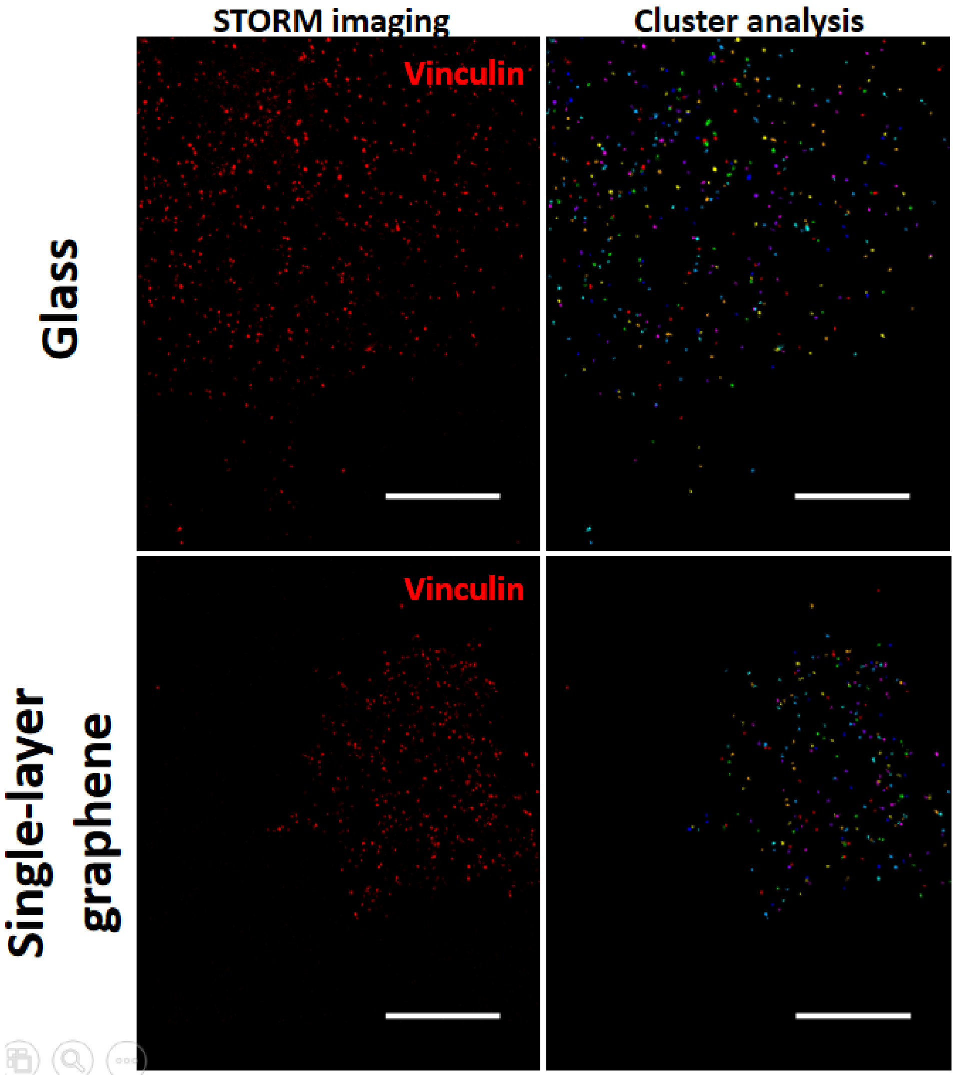

Figure 4.4 STORM imaging and cluster analysis of neurons adhered on glass and SLG. Scale bars, 5 µm

Then, we performed the same experiments on embryonal rat neurons. Unfortunately, we could not carry on all the necessary measurements to get a complete picture of the effect of graphene on the rearrangement of vinculin in neurons. We can only report preliminary data obtained from STORM imaging of DIV1 neurons.

We observed that neurons are indifferently located both on glass and SLG, and by analyzing localization data with clustering, we found no difference in the number of localizations of vinculin per nanodomain (Glass: 50.77 ± 1.11 n = 941; SLG: 41.81 ± 0.70 n = 1147, nonsignificant, Student's *t* test).

One day in vitro is too early to appreciate any difference between neuron adhesion on glass and graphene, as was to be expected from the results reported by Lorenzoni and co-workers showing the neurons migration on SLG stripes after 7 days in vitro (Lorenzoni et al., 2013).

4.5 Discussion

Graphene has brought significant contributions to neural tissue engineering due to its outstanding properties, such as conductivity, mechanical strength, high surface area, and biocompatibility. Several recent studies show that graphene combined with other materials to form nanocomposites can provide exceptional scaffolds for stimulating neural cell adhesion, proliferation, differentiation, or neural regeneration (Bei et al., 2019).

Recently a secure protocol has been optimized to induce localized and ordered growth of neurons on micropatterned graphene substrates, opening many possibilities for further research. Despite its effectiveness, the adhesion mechanism at the SLG-neuron interface is still not clear.

Here, we presented some preliminary results obtained employing single-molecule localization microscopy combined with cluster analysis, to investigate quantitatively the distribution of the adhesion protein vinculin in CHO cells and neurons seeded on glass or graphene.

Our results show that CVD grown graphene have an excellent biocompatibility, and it is suitable for the growth of both CHO and neurons. Moreover, in CHO cells on graphene, vinculin localizations per nanodomains are 42% higher than in cells adhered to glass, demonstrating that the higher affinity of CHO cells for SLG is related to morphological and quantitative changes in the organization of the adhesion machinery of the cell.

Regarding neurons, we showed only preliminary data. Still, we aim to perform more experiments in order to test the plausibility of a result similar to vinculin in CHO, as we would expect from measurements on neurons cultured for more than 7 days.

However, here we have optimized an effcient approach that can be exploited in the future to deepen the comprehension of cell adhesions on graphene, but also on any other nanostructured material.

Chapter 5

Conclusions and future perspectives

By circumventing the diffraction barrier, super-resolution optical microscopy has led to breakthrough discoveries in several fields of life science, allowing the nanoscale observation of diffraction-limited cell structures, up to the single-molecule scale. Today, nanoscopy is a well-established imaging tool and has become a workhorse of many biological laboratories all over the world.

With the spatial resolution improvement, a greater interest in performing quantitative measurements at the molecular level has come along, in order to respond to a huge number of still unresolved questions.

In this context, we proposed a method to achieve quantitative information from single-molecule localization microscopy, which allowed us reaching innovative insights into the molecular mechanisms underlying transmission processes at the synapses, and into the adhesion machinery changes due to the interaction between cells and nanomaterials.

Many recent studies related to super-resolved imaging of the arrangement of synaptic proteins revealed that neurotransmitter receptors and scaffold proteins are organized in nanometric and highly dynamic SSDs (subsynaptic domains). SSD formation and remodeling have a fundamental role in modulation and plasticity of the synaptic neurotransmission (Crosby et al., 2019; Pennacchietti et al., 2017; Yang and Specht, 2019). Thanks to our approach applied to the study of the inhibitory receptor $\mathrm{GABA_A}$, we made a step forward in the understanding of the SSD architecture. Thus, we opened a window on the achievement of a more profound knowledge of the synaptic processes and their failure in neurological diseases.

In detail, we achieved the molecular characterization of $\mathrm{GABA_AR}$ SSDs in basal and in plasticity conditions. This result is state-of-art in the current scientific landscape.

The recent rise of a new family of nanostructured materials derived from graphene, strongly demand for a detailed characterization of the interaction between biological samples and these novel biocompatible materials. Especially in the light of their applicability in several fields of biomedicine, such as tissue engineering and regenerative medicine, it is necessary to develop a strategy that might unveil how single-layer graphene affects the molecular mechanisms behind cell adhesion.

By quantifying protein components of focal adhesions, we highlighted modifications occurring in the adhesion machinery of epithelial cells and neurons in order to find an explanation for the cell-type dependent migration reported in recent literature (Keshavan et al., 2017; Lorenzoni et al., 2013).

The preliminary data we obtained show that cell adhesion studies can be tackled at the molecular level and that the presented approach is potentially suited for any other nanostructured or nanocomposite materials.

Generally, the understanding of proteins stoichiometry, dynamics, and interaction is crucial for the identification of the etiology of pathologies and disorders in the human body. Thus, only a quantitative and high-resolved view of protein assemblies and their related processes may lead to the development of potential treatments and therapies in the future.

This thesis contributes to the research effort aimed at accomplishing the goal mentioned above providing a cutting edge advance in quantitative single-molecule localization microscopy.

List of References

Abbe, E. 1873. Beiträge zur Theorie des Mikroskops und der mikroskopischen Wahrnehmung. *Archiv für mikroskopische Anatomie*. 9:413-418.

Abraham, A.V., S. Ram, J. Chao, E. Ward, and R.J. Ober. 2009. Quantitative study of single molecule location estimation techniques. *Optics express*. 17:23352-23373.

Airy, G.B. 1835. On the Diffraction of an Object-glass with Circular Aperture: From the Transactions of the Cambridge Philosophical Society, Vol. V. Printed at the Pitt Press by John Smith.

Alberts, B., J. Wilson, and T. Hunt. 2008. Molecular Biology of the Cell (Garland Science, New York). *USA. 1601p*.

Andronov, L., I. Orlov, Y. Lutz, J.-L. Vonesch, and B.P. Klaholz. 2016. ClusterViSu, a method for clustering of protein complexes by Voronoi tessellation in super-resolution microscopy. *Scientific reports*. 6:24084.

Axelrod, D. 1981. Cell-substrate contacts illuminated by total internal reflection fluorescence. *The Journal of cell biology*. 89:141-145.

Axelrod, D. 2003. [1] Total internal reflection fluorescence microscopy in cell biology. *In* Methods in enzymology. Vol. 361. Elsevier. 1-33.

Balzarotti, F., Y. Eilers, K.C. Gwosch, A.H. Gynnå, V. Westphal, F.D. Stefani, J. Elf, and S.W. Hell. 2017. Nanometer resolution imaging and tracking of fluorescent molecules with minimal photon fluxes. *Science*. 355:606-612.

Barnard, E., P. Skolnick, R. Olsen, H. Mohler, W. Sieghart, G. Biggio, C. Braestrup, A. Bateson, and S. Langer. 1998. International Union of Pharmacology. XV. Subtypes of γ-aminobutyric acidA receptors: classification on the basis of subunit structure and receptor function. *Pharmacological reviews*. 50:291-314.

Bartelmess, J., S. Quinn, and S. Giordani. 2015. Carbon nanomaterials: multi-functional agents for biomedical fluorescence and Raman imaging. *Chemical Society Reviews*. 44:4672-4698.

Bates, M., T.R. Blosser, and X. Zhuang. 2005. Short-range spectroscopic ruler based on a single-molecule optical switch. *Physical review letters*. 94:108101.

Bates, M., G.T. Dempsey, K.H. Chen, and X. Zhuang. 2012. Multicolor super-resolution fluorescence imaging via multi-parameter fluorophore detection. *ChemPhysChem*. 13:99-107.

Bates, M., B. Huang, G.T. Dempsey, and X. Zhuang. 2007. Multicolor super-resolution imaging with photo-switchable fluorescent probes. *Science*. 317:1749-1753.

Bei, H.P., Y. Yang, Q. Zhang, Y. Tian, X. Luo, M. Yang, and X. Zhao. 2019. Graphene-based nanocomposites for neural tissue engineering. *Molecules*. 24:658.

Benke, A., and S. Manley. 2012. Live-cell dSTORM of cellular DNA based on direct DNA labeling. *Chembiochem*. 13:298-301.

Betzig, E. 1995. Proposed method for molecular optical imaging. *Optics letters*. 20:237-239.

Betzig, E., G.H. Patterson, R. Sougrat, O.W. Lindwasser, S. Olenych, J.S. Bonifacino, M.W. Davidson, J. Lippincott-Schwartz, and H.F. Hess. 2006. Imaging intracellular fluorescent proteins at nanometer resolution. *Science*. 313:1642-1645.

Böger, C., A.-S. Hafner, T. Schlichthärle, M.T. Strauss, S. Malkusch, U. Endesfelder, R. Jungmann, E.M. Schuman, and M. Heilemann. 2019. Super-resolution imaging and estimation of protein copy numbers at single synapses with DNA-point accumulation for imaging in nanoscale topography. *Neurophotonics*. 6:035008.

Born, M., and E. Wolf. 2013. Principles of optics: electromagnetic theory of propagation, interference and diffraction of light. Elsevier.

Brede, N., and M. Lakadamyali. 2012. GraspJ: an open source, real-time analysis package for super-resolution imaging. *Optical Nanoscopy*. 1:11.

Chalfie, M., Y. Tu, G. Euskirchen, W.W. Ward, and D.C. Prasher. 1994. Green fluorescent protein as a marker for gene expression. *Science*. 263:802-805.

Chen, F., P.W. Tillberg, and E.S. Boyden. 2015. Expansion microscopy. *Science*. 347:543-548.

Choquet, D., and A. Triller. 2013. The dynamic synapse. *Neuron*. 80:691-703.

Chozinski, T.J., A.R. Halpern, H. Okawa, H.-J. Kim, G.J. Tremel, R.O. Wong, and J.C. Vaughan. 2016. Expansion microscopy with conventional antibodies and fluorescent proteins. *Nature methods*. 13:485.

Clark, P.J., and F.C. Evans. 1954. Distance to nearest neighbor as a measure of spatial relationships in populations. *Ecology*. 35:445-453.

Coffman, V.C., and J.-Q. Wu. 2012. Counting protein molecules using quantitative fluorescence microscopy. *Trends in biochemical sciences*. 37:499-506.

Cordes, T., M. Strackharn, S.W. Stahl, W. Summerer, C. Steinhauer, C. Forthmann, E.M. Puchner, J. Vogelsang, H.E. Gaub, and P. Tinnefeld. 2009. Resolving single-molecule assembled patterns with superresolution blink-microscopy. *Nano letters*. 10:645-651.

Crosby, K.C., S.E. Gookin, J.D. Garcia, K.M. Hahm, M.L. Dell'Acqua, and K.R. Smith. 2019. Nanoscale Subsynaptic Domains Underlie the Organization of the Inhibitory Synapse. *Cell reports*. 26:3284-3297. e3283.

Dani, A., B. Huang, J. Bergan, C. Dulac, and X. Zhuang. 2010. Superresolution imaging of chemical synapses in the brain. *Neuron*. 68:843-856.

de Luca, E., T. Ravasenga, E.M. Petrini, A. Polenghi, T. Nieus, S. Guazzi, and A. Barberis. 2017. Inter-synaptic lateral diffusion of GABAA receptors shapes inhibitory synaptic currents. *Neuron*. 95:63-69. e65.

De Robertis, E.D., and H.S. Bennett. 1955. Some features of the submicroscopic morphology of synapses in frog and earthworm. *The Journal of Cell Biology*. 1:47-58.

Dempsey, G.T., M. Bates, W.E. Kowtoniuk, D.R. Liu, R.Y. Tsien, and X. Zhuang. 2010. Photoswitching Mechanism of Cyanine Dyes. *Biophysical Journal*. 98:394a.

Dempsey, G.T., J.C. Vaughan, K.H. Chen, M. Bates, and X. Zhuang. 2011. Evaluation of fluorophores for optimal performance in localization-based super-resolution imaging. *Nature methods*. 8:1027.

Denk, W., J.H. Strickler, and W.W. Webb. 1990. Two-photon laser scanning fluorescence microscopy. *Science*. 248:73-76.

Deschout, H., F.C. Zanacchi, M. Mlodzianoski, A. Diaspro, J. Bewersdorf, S.T. Hess, and K. Braeckmans. 2014. Precisely and accurately localizing single emitters in fluorescence microscopy. *Nature methods*. 11:253.

Draz, M.S., B.A. Fang, P. Zhang, Z. Hu, S. Gu, K.C. Weng, J.W. Gray, and F.F. Chen. 2014. Nanoparticle-mediated systemic delivery of siRNA for treatment of cancers and viral infections. *Theranostics*. 4:872.

Durisic, N., L. Laparra-Cuervo, Á. Sandoval-Álvarez, J.S. Borbely, and M. Lakadamyali. 2014. Single-molecule evaluation of fluorescent protein photoactivation efficiency using an in vivo nanotemplate. *Nature methods*. 11:156.

Dvir, T., B.P. Timko, D.S. Kohane, and R. Langer. 2011. Nanotechnological strategies for engineering complex tissues. *Nature nanotechnology*. 6:13.

Ester, M., H.-P. Kriegel, J. Sander, and X. Xu. 1996. A density-based algorithm for discovering clusters in large spatial databases with noise. *In* Kdd. Vol. 96. 226-231.

Farokhzad, O.C., and R. Langer. 2009. Impact of nanotechnology on drug delivery. *ACS nano*. 3:16-20.

Feng, L., and Z. Liu. 2011. Graphene in biomedicine: opportunities and challenges. *Nanomedicine*. 6:317-324.

Feng, L., S. Zhang, and Z. Liu. 2011. Graphene based gene transfection. *Nanoscale*. 3:1252-1257.

Ferrari, A.C., F. Bonaccorso, V. Fal'Ko, K.S. Novoselov, S. Roche, P. Bøggild, S. Borini, F.H. Koppens, V. Palermo, and N. Pugno. 2015. Science and technology roadmap for graphene, related two-dimensional crystals, and hybrid systems. *Nanoscale*. 7:4598-4810.

Fitzgerald, J.E., J. Lu, and M.J. Schnitzer. 2012. Estimation theoretic measure of resolution for stochastic localization microscopy. *Physical review letters*. 109:048102.

Fukazawa, Y., and R. Shigemoto. 2012. Intra-synapse-type and inter-synapse-type relationships between synaptic size and AMPAR expression. *Current opinion in neurobiology*. 22:446-452.

Gautier, A., A. Juillerat, C. Heinis, I.R. Corrêa Jr, M. Kindermann, F. Beaufils, and K. Johnsson. 2008. An engineered protein tag for multiprotein labeling in living cells. *Chemistry & biology*. 15:128-136.

Gelles, J., B.J. Schnapp, and M.P. Sheetz. 1988. Tracking kinesin-driven movements with nanometre-scale precision. *Nature*. 331:450.

Gustafsson, M.G. 2000. Surpassing the lateral resolution limit by a factor of two using structured illumination microscopy. *Journal of microscopy*. 198:82-87.

Gustafsson, M.G. 2005. Nonlinear structured-illumination microscopy: wide-field fluorescence imaging with theoretically unlimited resolution. *Proceedings of the National Academy of Sciences*. 102:13081-13086.

Heilemann, M., S. van de Linde, A. Mukherjee, and M. Sauer. 2009. Super-resolution imaging with small organic fluorophores. *Angewandte Chemie International Edition*. 48:6903-6908.

Heilemann, M., S. Van De Linde, M. Schüttpelz, R. Kasper, B. Seefeldt, A. Mukherjee, P. Tinnefeld, and M. Sauer. 2008. Subdiffraction-resolution fluorescence imaging with conventional fluorescent probes. *Angewandte Chemie International Edition*. 47:6172-6176.

Heine, M., L. Groc, R. Frischknecht, J.-C. Béïque, B. Lounis, G. Rumbaugh, R.L. Huganir, L. Cognet, and D. Choquet. 2008. Surface mobility of postsynaptic AMPARs tunes synaptic transmission. *Science*. 320:201-205.

Heisenberg, W. 1930. The Physical Principles of the Quantum Theory.

Hell, S.W., and M. Kroug. 1995. Ground-state-depletion fluorscence microscopy: A concept for breaking the diffraction resolution limit. *Applied Physics B*. 60:495-497.

Hell, S.W., and J. Wichmann. 1994. Breaking the diffraction resolution limit by stimulated emission: stimulated-emission-depletion fluorescence microscopy. *Optics letters*. 19:780-782.

Hess, S.T., T.P. Girirajan, and M.D. Mason. 2006. Ultra-high resolution imaging by fluorescence photoactivation localization microscopy. *Biophysical journal*. 91:4258-4272.

Hofmann, M., C. Eggeling, S. Jakobs, and S.W. Hell. 2005. Breaking the diffraction barrier in fluorescence microscopy at low light intensities by using reversibly photoswitchable proteins. *Proceedings of the National Academy of Sciences*. 102:17565-17569.

Huang, B., W. Wang, M. Bates, and X. Zhuang. 2008. Three-dimensional super-resolution imaging by stochastic optical reconstruction microscopy. *Science*. 319:810-813.

Huang, F., T.M. Hartwich, F.E. Rivera-Molina, Y. Lin, W.C. Duim, J.J. Long, P.D. Uchil, J.R. Myers, M.A. Baird, and W. Mothes. 2013. Video-rate nanoscopy using sCMOS camera–specific single-molecule localization algorithms. *Nature methods*. 10:653.

Jablonski, A. 1933. Efficiency of Anti-Stokes Fluorescence in Dyes. *Nature*. 131:839-840.

Jacob, T.C., Y.D. Bogdanov, C. Magnus, R.S. Saliba, J.T. Kittler, P.G. Haydon, and S.J. Moss. 2005. Gephyrin regulates the cell surface dynamics of synaptic GABAA receptors. *Journal of Neuroscience*. 25:10469-10478.

Jia, S., J.C. Vaughan, and X. Zhuang. 2014. Isotropic three-dimensional super-resolution imaging with a self-bending point spread function. *Nature photonics*. 8:302.

Jin, Y., and C.C. Garner. 2008. Molecular mechanisms of presynaptic differentiation. *Annual review of cell and developmental biology*. 24:237-262.

Jones, S.A., S.-H. Shim, J. He, and X. Zhuang. 2011. Fast, three-dimensional super-resolution imaging of live cells. *Nature methods*. 8:499.

Jungmann, R., M.S. Avendaño, M. Dai, J.B. Woehrstein, S.S. Agasti, Z. Feiger, A. Rodal, and P. Yin. 2016. Quantitative super-resolution imaging with qPAINT. *Nature methods*. 13:439.

Kalbacova, M., A. Broz, J. Kong, and M. Kalbac. 2010. Graphene substrates promote adherence of human osteoblasts and mesenchymal stromal cells. *Carbon*. 48:4323-4329.

Kanchanawong, P., G. Shtengel, A.M. Pasapera, E.B. Ramko, M.W. Davidson, H.F. Hess, and C.M. Waterman. 2010. Nanoscale architecture of integrin-based cell adhesions. *Nature*. 468:580-584.

Kandel, E.R., J.H. Schwartz, T.M. Jessell, D.o. Biochemistry, M.B.T. Jessell, S. Siegelbaum, and A. Hudspeth. 2000. Principles of neural science. McGraw-hill New York.

Kasugai, Y., J.D. Swinny, J.D.B. Roberts, Y. Dalezios, Y. Fukazawa, W. Sieghart, R. Shigemoto, and P. Somogyi. 2010. Quantitative localisation of synaptic and extrasynaptic GABAA receptor subunits on hippocampal pyramidal cells by freeze-fracture replica immunolabelling. *European Journal of Neuroscience*. 32:1868-1888.

Ke, Y., L.L. Ong, W.M. Shih, and P. Yin. 2012. Three-dimensional structures self-assembled from DNA bricks. *science*. 338:1177-1183.

Keshavan, S., R. Oropesa-Nuñez, A. Diaspro, C. Canale, and S. Dante. 2017. Adhesion and migration of CHO cells on micropatterned single layer graphene. *2D Materials*. 4:025022.

Klar, T.A., and S.W. Hell. 1999. Subdiffraction resolution in far-field fluorescence microscopy. *Optics letters*. 24:954-956.

Klessinger, M. 1978. Konstitution und Lichtabsorption organischer Farbstoffe. *Chemie in unserer Zeit*. 12:1-11.

Kneussel, M., J.H. Brandstätter, B. Laube, S. Stahl, U. Müller, and H. Betz. 1999. Loss of postsynaptic GABAA receptor clustering in gephyrin-deficient mice. *Journal of Neuroscience*. 19:9289-9297.

Kufer, S., E. Puchner, H. Gumpp, T. Liedl, and H. Gaub. 2008. Single-molecule cut-and-paste surface assembly. *Science*. 319:594-596.

Kuila, T., S. Bose, P. Khanra, A.K. Mishra, N.H. Kim, and J.H. Lee. 2011. Recent advances in graphene-based biosensors. *Biosensors and bioelectronics*. 26:4637-4648.

Lakadamyali, M. 2014. Super-resolution microscopy: Going live and going fast. *Chemphyschem*. 15:630-636.

Lakowicz, J.R. 2006. Principles of Fluorescence Spectroscopy. Springer Publications.

Laughlin, S.T., J.M. Baskin, S.L. Amacher, and C.R. Bertozzi. 2008. In vivo imaging of membrane-associated glycans in developing zebrafish. *Science*. 320:664-667.

Lee, W.C., C.H.Y. Lim, H. Shi, L.A. Tang, Y. Wang, C.T. Lim, and K.P. Loh. 2011. Origin of enhanced stem cell growth and differentiation on graphene and graphene oxide. *ACS nano*. 5:7334-7341.

Leung, B.O., and K.C. Chou. 2011. Review of super-resolution fluorescence microscopy for biology. *Applied spectroscopy*. 65:967-980.

Levet, F., E. Hosy, A. Kechkar, C. Butler, A. Beghin, D. Choquet, and J.-B. Sibarita. 2015. SR-Tesseler: a method to segment and quantify localization-based super-resolution microscopy data. *Nature methods*. 12:1065.

Li, N., X. Zhang, Q. Song, R. Su, Q. Zhang, T. Kong, L. Liu, G. Jin, M. Tang, and G. Cheng. 2011. The promotion of neurite sprouting and outgrowth of mouse hippocampal cells in culture by graphene substrates. *Biomaterials*. 32:9374-9382.

Lichtman, J.W., and J.A. Conchello. 2005. Fluorescence microscopy. *Nat Methods*. 2:910-919.

Lorenzoni, M., F. Brandi, S. Dante, A. Giugni, and B. Torre. 2013. Simple and effective graphene laser processing for neuron patterning application. *Scientific reports*. 3:1954.

Luscher, B., Q. Shen, and N. Sahir. 2011. The GABAergic deficit hypothesis of major depressive disorder. *Molecular psychiatry*. 16:383.

MacGillavry, H.D., Y. Song, S. Raghavachari, and T.A. Blanpied. 2013. Nanoscale scaffolding domains within the postsynaptic density concentrate synaptic AMPA receptors. *Neuron*. 78:615-622.

Magrassi, R., S. Scalisi, and F.C. Zanacchi. 2019. Single-molecule localization to study cytoskeletal structures, membrane complexes, and mechanosensors. *Biophysical reviews*:1-12.

Marsden, K.C., J.B. Beattie, J. Friedenthal, and R.C. Carroll. 2007. NMDA receptor activation potentiates inhibitory transmission through GABA receptor-associated protein-dependent exocytosis of GABAA receptors. *Journal of Neuroscience*. 27:14326-14337.

Menaa, F., A. Abdelghani, and B. Menaa. 2015. Graphene nanomaterials as biocompatible and conductive scaffolds for stem cells: impact for tissue engineering and regenerative medicine. *Journal of tissue engineering and regenerative medicine*. 9:1321-1338.

Minsky, M., and M. Minsky. 1961. Microscopy apparatus. US Patent US3,013,467.

Moerner, W.E., and L. Kador. 1989. Optical detection and spectroscopy of single molecules in a solid. *Physical review letters*. 62:2535.

Nahidiazar, L., A.V. Agronskaia, J. Broertjes, B. van den Broek, and K. Jalink. 2016. Optimizing imaging conditions for demanding multi-color super resolution localization microscopy. *PLoS One*. 11:e0158884.

Nair, D., E. Hosy, J.D. Petersen, A. Constals, G. Giannone, D. Choquet, and J.-B. Sibarita. 2013. Super-resolution imaging reveals that AMPA receptors inside synapses are dynamically organized in nanodomains regulated by PSD95. *Journal of Neuroscience*. 33:13204-13224.

Nayak, T.R., H. Andersen, V.S. Makam, C. Khaw, S. Bae, X. Xu, P.-L.R. Ee, J.-H. Ahn, B.H. Hong, and G. Pastorin. 2011. Graphene for controlled and accelerated osteogenic differentiation of human mesenchymal stem cells. *ACS nano*. 5:4670-4678.

Nicovich, P.R., D.M. Owen, and K. Gaus. 2017. Turning single-molecule localization microscopy into a quantitative bioanalytical tool. *Nature protocols*. 12:453.

Nikon, S.R.M.N. STORM. STORM Protocol-Sample Preparation,[Online; retrieved on 10th of November 2015], 2015.

Novoselov, K.S., A.K. Geim, S.V. Morozov, D. Jiang, Y. Zhang, S.V. Dubonos, I.V. Grigorieva, and A.A. Firsov. 2004. Electric field effect in atomically thin carbon films. *science*. 306:666-669.

Nusser, Z., N. Hajos, P. Somogyi, and I. Mody. 1998. Increased number of synaptic GABA A receptors underlies potentiation at hippocampal inhibitory synapses. *Nature*. 395:172.

Palay, S.L., and G.E. Palade. 1955. The fine structure of neurons. *The Journal of biophysical and biochemical cytology*. 1:69.

Park, J., J.-H. Yoo, and C.P. Grigoropoulos. 2012. Multi-scale graphene patterns on arbitrary substrates via laser-assisted transfer-printing process. *Applied Physics Letters*. 101:043110.

Patterson, G.H., and J. Lippincott-Schwartz. 2002. A photoactivatable GFP for selective photolabeling of proteins and cells. *Science*. 297:1873-1877.

Pavani, S.R.P., M.A. Thompson, J.S. Biteen, S.J. Lord, N. Liu, R.J. Twieg, R. Piestun, and W. Moerner. 2009. Three-dimensional, single-molecule fluorescence imaging beyond the diffraction limit by using a double-helix point spread function. *Proceedings of the National Academy of Sciences*. 106:2995-2999.

Pennacchietti, F., S. Vascon, T. Nieus, C. Rosillo, S. Das, S.K. Tyagarajan, A. Diaspro, A. Del Bue, E.M. Petrini, and A. Barberis. 2017. Nanoscale molecular reorganization of the inhibitory postsynaptic density is a determinant of GABAergic synaptic potentiation. *Journal of Neuroscience*. 37:1747-1756.

Petrini, E.M., and A. Barberis. 2014. Diffusion dynamics of synaptic molecules during inhibitory postsynaptic plasticity. *Frontiers in Cellular Neuroscience*. 8.

Petrini, E.M., J. Lu, L. Cognet, B. Lounis, M.D. Ehlers, and D. Choquet. 2009. Endocytic trafficking and recycling maintain a pool of mobile surface AMPA receptors required for synaptic potentiation. *Neuron*. 63:92-105.

Petrini, E.M., T. Ravasenga, T.J. Hausrat, G. Iurilli, U. Olcese, V. Racine, J.-B. Sibarita, T.C. Jacob, S.J. Moss, and F. Benfenati. 2014. Synaptic recruitment of gephyrin regulates surface GABA A receptor dynamics for the expression of inhibitory LTP. *Nature communications*. 5:3921.

Randviir, E.P., D.A. Brownson, and C.E. Banks. 2014. A decade of graphene research: production, applications and outlook. *Materials Today*. 17:426-432.

Recknor, J.B., D.S. Sakaguchi, and S.K. Mallapragada. 2006. Directed growth and selective differentiation of neural progenitor cells on micropatterned polymer substrates. *Biomaterials*. 27:4098-4108.

Rego, E.H., L. Shao, J.J. Macklin, L. Winoto, G.A. Johansson, N. Kamps-Hughes, M.W. Davidson, and M.G. Gustafsson. 2012. Nonlinear structured-illumination microscopy with a photoswitchable protein reveals cellular structures at 50-nm resolution. *Proceedings of the National Academy of Sciences*. 109:E135-E143.

Renner, M., C.G. Specht, and A. Triller. 2008. Molecular dynamics of postsynaptic receptors and scaffold proteins. *Current opinion in neurobiology*. 18:532-540.

Ricci, M.A., C. Manzo, M.F. García-Parajo, M. Lakadamyali, and M.P. Cosma. 2015. Chromatin fibers are formed by heterogeneous groups of nucleosomes in vivo. *Cell*. 160:1145-1158.

Ries, J., C. Kaplan, E. Platonova, H. Eghlidi, and H. Ewers. 2012. A simple, versatile method for GFP-based super-resolution microscopy via nanobodies. *Nature methods*. 9:582.

Ripley, B. 1977. The point processes of stochastic geometry. *Advances in Applied Probability*. 9:434-435.

Rust, M.J., M. Bates, and X. Zhuang. 2006. Sub-diffraction-limit imaging by stochastic optical reconstruction microscopy (STORM). *Nature methods*. 3:793.

Ryu, S., and B.-S. Kim. 2013. Culture of neural cells and stem cells on graphene. *Tissue Engineering and Regenerative Medicine*. 10:39-46.

Sahl, S.J., S.W. Hell, and S. Jakobs. 2017. Fluorescence nanoscopy in cell biology. *Nature reviews Molecular cell biology*. 18:685.

Sanchez, V.C., A. Jachak, R.H. Hurt, and A.B. Kane. 2012. Biological interactions of graphene-family nanomaterials: an interdisciplinary review. *Chemical research in toxicology*. 25:15-34.

Sauer, M. 2013. Localization microscopy coming of age: from concepts to biological impact. *J Cell Sci*. 126:3505-3513.

Sengupta, P., T. Jovanovic-Talisman, D. Skoko, M. Renz, S.L. Veatch, and J. Lippincott-Schwartz. 2011. Probing protein heterogeneity in the plasma membrane using PALM and pair correlation analysis. *Nature methods*. 8:969.

Sharonov, A., and R.M. Hochstrasser. 2006. Wide-field subdiffraction imaging by accumulated binding of diffusing probes. *Proceedings of the National Academy of Sciences*. 103:18911-18916.

Shim, S.-H., C. Xia, G. Zhong, H.P. Babcock, J.C. Vaughan, B. Huang, X. Wang, C. Xu, G.-Q. Bi, and X. Zhuang. 2012. Super-resolution fluorescence imaging of organelles in live cells with photoswitchable membrane probes. *Proceedings of the National Academy of Sciences*. 109:13978-13983.

Shroff, H., C.G. Galbraith, J.A. Galbraith, and E. Betzig. 2008. Live-cell photoactivated localization microscopy of nanoscale adhesion dynamics. *Nature methods*. 5:417.

Shroff, H., C.G. Galbraith, J.A. Galbraith, H. White, J. Gillette, S. Olenych, M.W. Davidson, and E. Betzig. 2007. Dual-color superresolution imaging of genetically expressed probes within individual adhesion complexes. *Proceedings of the National Academy of Sciences*. 104:20308-20313.

Shtengel, G., J.A. Galbraith, C.G. Galbraith, J. Lippincott-Schwartz, J.M. Gillette, S. Manley, R. Sougrat, C.M. Waterman, P. Kanchanawong, and M.W. Davidson. 2009. Interferometric fluorescent super-resolution microscopy resolves 3D cellular ultrastructure. *Proceedings of the National Academy of Sciences*. 106:3125-3130.

Sigal, Y.M., R. Zhou, and X. Zhuang. 2018. Visualizing and discovering cellular structures with super-resolution microscopy. *Science*. 361:880-887.

Small, A., and S. Stahlheber. 2014. Fluorophore localization algorithms for super-resolution microscopy. *Nature methods*. 11:267.

Specht, C.G., I. Izeddin, P.C. Rodriguez, M. El Beheiry, P. Rostaing, X. Darzacq, M. Dahan, and A. Triller. 2013. Quantitative nanoscopy of inhibitory synapses: counting gephyrin molecules and receptor binding sites. *Neuron*. 79:308-321.

Sprinkle, M., M. Ruan, Y. Hu, J. Hankinson, M. Rubio-Roy, B. Zhang, X. Wu, C. Berger, and W.A. De Heer. 2010. Scalable templated growth of graphene nanoribbons on SiC. *Nature nanotechnology*. 5:727-731.

Squire, L., D. Berg, F.E. Bloom, S. Du Lac, A. Ghosh, and N.C. Spitzer. 2012. Fundamental neuroscience. Academic Press.

Steinhauer, C., R. Jungmann, T.L. Sobey, F.C. Simmel, and P. Tinnefeld. 2009. DNA origami as a nanoscopic ruler for super-resolution microscopy. *Angewandte Chemie International Edition*. 48:8870-8873.

Strong, V., S. Dubin, M.F. El-Kady, A. Lech, Y. Wang, B.H. Weiller, and R.B. Kaner. 2012. Patterning and electronic tuning of laser scribed graphene for flexible all-carbon devices. *ACS nano*. 6:1395-1403.

Suk, J.W., A. Kitt, C.W. Magnuson, Y. Hao, S. Ahmed, J. An, A.K. Swan, B.B. Goldberg, and R.S. Ruoff. 2011. Transfer of CVD-grown monolayer graphene onto arbitrary substrates. *ACS nano*. 5:6916-6924.

Sun, X., Z. Liu, K. Welsher, J.T. Robinson, A. Goodwin, S. Zaric, and H. Dai. 2008. Nano-graphene oxide for cellular imaging and drug delivery. *Nano research*. 1:203-212.

Swoboda, M., J.r. Henig, H.-M. Cheng, D. Brugger, D. Haltrich, N. Plumeré, and M. Schlierf. 2012. Enzymatic oxygen scavenging for photostability without pH drop in single-molecule experiments. *ACS nano*. 6:6364-6369.

Tang, A.-H., H. Chen, T.P. Li, S.R. Metzbower, H.D. MacGillavry, and T.A. Blanpied. 2016. A trans-synaptic nanocolumn aligns neurotransmitter release to receptors. *Nature*. 536:210.

Tarusawa, E., K. Matsui, T. Budisantoso, E. Molnár, M. Watanabe, M. Matsui, Y. Fukazawa, and R. Shigemoto. 2009. Input-specific intrasynaptic arrangements of ionotropic glutamate receptors and their impact on postsynaptic responses. *Journal of Neuroscience*. 29:12896-12908.

Thevathasan, J.V., M. Kahnwald, K. Cieśliński, P. Hoess, S.K. Peneti, M. Reitberger, D. Heid, K.C. Kasuba, S.J. Hoerner, and Y. Li. 2019. Nuclear pores as versatile reference standards for quantitative superresolution microscopy. *BioRxiv*:582668.

Thompson, R.E., D.R. Larson, and W.W. Webb. 2002. Precise nanometer localization analysis for individual fluorescent probes. *Biophysical journal*. 82:2775-2783.

Turkowyd, B., D. Virant, and U. Endesfelder. 2016. From single molecules to life: microscopy at the nanoscale. *Analytical and bioanalytical chemistry*. 408:6885-6911.

Ulbrich, M.H., and E.Y. Isacoff. 2007. Subunit counting in membrane-bound proteins. *Nature methods*. 4:319.

Ventre, M., C.F. Natale, C. Rianna, and P.A. Netti. 2014. Topographic cell instructive patterns to control cell adhesion, polarization and migration. *Journal of the royal society Interface*. 11:20140687.

Wang, Z., and Z. Dai. 2015. Carbon nanomaterial-based electrochemical biosensors: an overview. *Nanoscale*. 7:6420-6431.

Weber, K., P.C. Rathke, and M. Osborn. 1978. Cytoplasmic microtubular images in glutaraldehyde-fixed tissue culture cells by electron microscopy and by immunofluorescence microscopy. *Proceedings of the National Academy of Sciences*. 75:1820-1824.

Wehrle-Haller, B. 2012. Structure and function of focal adhesions. *Current opinion in cell biology*. 24:116-124.

Wombacher, R., M. Heidbreder, S. Van De Linde, M.P. Sheetz, M. Heilemann, V.W. Cornish, and M. Sauer. 2010. Live-cell super-resolution imaging with trimethoprim conjugates. *Nature methods*. 7:717.

Xu, K., G. Zhong, and X. Zhuang. 2013. Actin, spectrin, and associated proteins form a periodic cytoskeletal structure in axons. *Science*. 339:452-456.

Yang, X., and C.G. Specht. 2019. Subsynaptic domains in super-resolution microscopy: the treachery of images. *Frontiers in Molecular Neuroscience*. 12:161.

Yin, F., B. Gu, Y. Lin, N. Panwar, S.C. Tjin, J. Qu, S.P. Lau, and K.-T. Yong. 2017. Functionalized 2D nanomaterials for gene delivery applications. *Coordination Chemistry Reviews*. 347:77-97.

Yizhar, O., L.E. Fenno, M. Prigge, F. Schneider, T.J. Davidson, D.J. O'shea, V.S. Sohal, I. Goshen, J. Finkelstein, and J.T. Paz. 2011. Neocortical excitation/inhibition balance in information processing and social dysfunction. *Nature*. 477:171.

Yoo, J.M., J.H. Kang, and B.H. Hong. 2015. Graphene-based nanomaterials for versatile imaging studies. *Chemical Society Reviews*. 44:4835-4852.

Zanacchi, F.C., C. Manzo, A.S. Alvarez, N.D. Derr, M.F. Garcia-Parajo, and M. Lakadamyali. 2017. A DNA origami platform for quantifying protein copy number in super-resolution. *Nature methods*. 14:789.

Zhang, L., and T.J. Webster. 2009. Nanotechnology and nanomaterials: promises for improved tissue regeneration. *Nano today*. 4:66-80.

Zhang, L., J. Xia, Q. Zhao, L. Liu, and Z. Zhang. 2010. Functional graphene oxide as a nanocarrier for controlled loading and targeted delivery of mixed anticancer drugs. *small*. 6:537-544.

Zuber, B., I. Nikonenko, P. Klauser, D. Muller, and J. Dubochet. 2005. The mammalian central nervous synaptic cleft contains a high density of periodically organized complexes. *Proceedings of the National Academy of Sciences*. 102:19192-19197.

List of Publications

Scalisi S. and Petrini M.E., Diaspro A., Zanacchi F.C. and Barberis A. (2020). *(in preparation*)

Magrassi R., **Scalisi S.**, Zanacchi F.C. (2019). Single-molecule localization to study cytoskeletal structures, membrane complexes, and mechanosensors. *Biophysical reviews*, 1-12.

Scalisi S., Barberis A., Petrini E.M., Zanacchi F.C., Diaspro A. (2019). Unveiling the inhibitory synapse organization using super-resolution microscopy. *Biophysical Journal*, *116*(3), 133a.

Scalisi S., Barberis A., Petrini E.M., Diaspro A., Zanacchi F.C. (2018). Quantitative super-resolution microscopy of proteins at the synaptic level. *Biophysical Journal*, *114*(3), 539a.

Acknowledgements

At the end of a three-year journey, rich in satisfactions and frustrations, in smiles and tears, in confidence and discouragement, it is impossible not to look behind, to sum up, and thank those who have been close to us.

The Ph.D. is an overwhelming experience. For me, as for many others, it was even more because it meant leaving my beloved Sicily, my family, and my friends for the first time for so long. Anyway, it has also meant welcoming a city in my heart, which now I consider a new home and where I found new irreplaceable friends. It was a unique opportunity for training and growth, which taught me a lot and made me more aware of scientific research.

For this reason, I would like to thank above all the excellent scientists I worked with. Dr. Francesca Cella Zanacchi, who has been my mentor in these years, for sharing her vast knowledge with me. Dr. Enrica Maria Petrini and Dr. Andrea Barberis of the IIT Neuroscience and Brain Technology department, for their valuable collaboration in the inhibitory synapse project. Dr. Silvia Dante and Dr. Amira El Merhie, for their kind cooperation in the graphene project. Dutiful thanks also to my supervisor, Prof. Alberto Diaspro, and to colleagues and technicians of the Nanoscopy and the Molecular Microscopy and Spectroscopy IIT groups, for the lab assistance and their scientific and non-scientific help.

I want to thank my family. My father, Nino, and my sister, Sabrina, who supported me in all the possible forms, during the way to the nth educational degree (I swear, this is the last!). Thank you, together with Davide, Giovanna, and baby Beatrice, for never having stopped missing me.

To Stefano, my partner, thank you for being the wonderful person you are, for sharing dreams and hopes with me, for moving your life to Genoa, for sustaining me, and for tolerating the delirious "Ph.D. students outburst" in which you have been often involved.

Finally, I thank Alberta, Artemi, Marco, Denise, Melody, Riccardo, etc., for not being just colleagues to me, for the scientific comparisons, for the support, the drinks and the trips

together, the psychoanalysis sessions, the teas, and the sheep. To all of you, who most than any other shared the collective pleasures and harms of this journey with me, and especially to those who still have a year or two to face, I dedicate this poem by William E. Henley:

Invictus

"Out of the night that covers me,
Black as the pit from pole to pole,
I thank whatever gods may be
For my unconquerable soul.
In the fell clutch of circumstance
I have not winced nor cried aloud.
Under the bludgeonings of chance
My head is bloody, but unbowed.
Beyond this place of wrath and tears
Looms but the Horror of the shade,
And yet the menace of the years
Finds and shall find me unafraid.
It matters not how strait the gate,
How charged with punishments the scroll,
I am the master of my fate:
I am the captain of my soul."

Ringraziamenti

Alla fine di un percorso durato tre anni, denso di soddisfazioni e di delusioni, di sorrisi e di lacrime, di fiducia e di sconforto, è impossibile non guardarsi indietro per tirare le somme e ringraziare chi ci è stato accanto.

Il dottorato di ricerca è un'esperienza travolgente. Per me, come per molti altri, lo è stata ancor di più perché ha significato allontanarmi per la prima volta per così tanto tempo dalla mia amata Sicilia, dalla famiglia e dagli amici, tuttavia per accogliere nel mio cuore una città che adesso sento come una nuova casa e dove ho trovato nuovi insostituibili amici. È stata un'occasione unica di formazione e di crescita, che mi ha insegnato e fatto capire tanto sulla ricerca scientifica.

Per questo motivo, vorrei innanzitutto ringraziare gli eccezionali scienziati con cui ho lavorato. La dott.ssa Francesca Cella Zanacchi, che è stata la mia mentore in questi anni, per aver condiviso con me la sua vasta conoscenza. La dott.ssa Enrica Maria Petrini e il dott. Andrea Barberis del dipartimento Neuroscience and Brain Technology dell'IIT, per la preziosa collaborazione nel progetto sulla sinapsi inibitoria. La dott.ssa Silvia Dante e la dott.ssa Amira El Merhie, per la gentile collaborazione nel progetto sul grafene. Un doveroso ringraziamento va inoltre al mio supervisor, il prof. Alberto Diaspro, e ai colleghi e ai tecnici dei gruppi Nanoscopy e Molecular Microscopy and Spectroscopy dell'IIT, per tutto l'aiuto e il supporto scientifico e non scientifico.

Vorrei ringraziare la mia famiglia. Mio padre, Nino, e mia sorella, Sabrina, che pur lontani mi hanno sostenuta in tutti i modi possibili, in questo cammino verso l'ennesimo sudato titolo di studio (giuro che è l'ultimo!). Grazie a voi, insieme a Davide, Giovanna e la piccola Beatrice, per non aver mai smesso di sentire la mia mancanza.

A Stefano, il mio compagno, grazie per essere la persona splendida che sei, per condividere con me sogni e speranze, per esserti trasferito a Genova, per avermi fiancheggiata, e per aver sopportato i deliranti "sfoghi da dottorandi" in cui ti sei spesso trovato coinvolto.

Infine, ringrazio Alberta, Artemi, Marco, Denise, Melody, Riccardo, etc., per non essere stati solo dei colleghi, per il confronto scientifico, per il sostegno, le bevute, i viaggi insieme, le sedute di psicoanalisi, i tè e le pecore. A tutti voi, che più di tutti avete condiviso le comuni gioie e i comuni mali di questo percorso con me, e soprattutto a chi ha ancora uno o due anni da affrontare, dedico questa poesia di William E. Henley:

Invictus

“Dal profondo della notte che mi avvolge,
Nera come un pozzo da un estremo all'altro,
Ringrazio qualunque dio ci sia
Per la mia anima invincibile.
Nella stretta morsa delle avversità
Non mi sono tirato indietro né ho gridato.
Sotto i colpi avversi della sorte
Il mio capo sanguina, ma non si china.
Oltre questo luogo di rabbia e lacrime
Incombe solo l'orrore della fine.
Eppure la minaccia degli anni
Mi trova, e mi troverà, senza paura.
Non importa quanto stretta sia la porta,
Quanto impietosa sia la vita,
Io sono il padrone del mio destino:
Io sono il capitano della mia anima.”